

~~UNCLASSIFIED~~ REPORT DOCUMENTATION PAGE

Form Approved
OMB No. 0704-0188

1. AGENCY USE ONLY (Leave blank)		2. REPORT DATE 31 JAN 1992	3. REPORT TYPE AND DATES COVERED FINAL 1 JUN 91 - 30 NOV 91
4. TITLE AND SUBTITLE PRESSURE-BASED HIGH-ORDER TVD METHODOLOGY FOR DYNAMIC STALL CONTROL			5. AUTHOR(S) H Q YANG AND A J PRZEKAS
6. AUTHOR(S) H Q YANG AND A J PRZEKAS			7. PERFORMING ORGANIZATION NAME(S) AND ADDRESS(ES) CFD RESEARCH CORP 3325-D TRIANA BLVD HUNTSVILLE, ALABAMA 35805
9. SPONSORING MONITORING AGENCY NAME(S) AND ADDRESS(ES) AFOSR/NA BOLLING AFB DC 20332-6448			10. SPONSORING MONITORING AGENCY REPORT NUMBER F49620-91-C-0042 3005/A1
11. SUPPLEMENTARY NOTES			
12a. DISTRIBUTION AVAILABILITY STATEMENT UNLIMITED			12b. DISTRIBUTION CODE
13. ABSTRACT (Maximum 200 words) The quantitative prediction of the dynamics of separating unsteady flows, such as dynamic stall, is of crucial importance. This six-month SBIR Phase I study has developed several new pressure-based methodologies for solving 3D Navier-Stokes equations in both stationary and moving (body-comforting) coordinated. The modified code was used to simulate both static and dynamic stalls on two-and three-dimensional wing-body configurations. Three-dimensional effects and flow physics are discussed.			
14. SUBJECT TERMS D-D Dynamic Stall, TVD Methodology			15. NUMBER OF PAGES 152
17. SECURITY CLASSIFICATION OF REPORT U	18. SECURITY CLASSIFICATION OF ABSTRACT U	19. SECURITY CLASSIFICATION OF ABSTRACT U	20. LIMITATION OF ABSTRACT

UNCLASSIFIED

ADA247 056

**PRESSURE-BASED HIGH-ORDER TVD METHODOLOGY
FOR DYNAMIC STALL CONTROL
SBIR Phase I Final Report**

by
H.Q. Yang and A.J. Przekwas
CFD Research Corporation
3325-D Triana Blvd.
Huntsville, Alabama 35805

January 1992

CFDRC Report 4170/1

for
Air Force Office of Scientific Research
Bolling Air Force Base, DC 20332-6448

Contract: F49620-91-C-0042
Project Manager: Major Daniel Fant



Accession For	
NTIS GRA&I	<input checked="" type="checkbox"/>
DTIC TAB	<input type="checkbox"/>
Unannounced	<input type="checkbox"/>
Justification	
By	
Distribution/	
Availability Codes	
Dist	Avail and/or Special
A-1	

PROJECT SUMMARY

The quantitative prediction of the dynamics of separating unsteady flows, such as dynamic stall, is of crucial importance. This six-month SBIR Phase I study has developed several new pressure-based methodologies for solving 3D Navier-Stokes equations in both stationary and moving (body-comforting) coordinates. The present pressure-based algorithm is equally efficient for low speed incompressible flows and high speed compressible flows. The discretization of convective terms by the presently developed high-order TVD schemes requires no artificial dissipation and can properly resolve the concentrated vortices in the wing-body with minimum numerical diffusion. It is demonstrated that the proposed Newton's iteration technique not only increases the convergence rate but also strongly couples the iteration between pressure and velocities. The proposed hyperbolization of the pressure correction equation is shown to increase the solver's efficiency. The above proposed methodologies were implemented in an existing CFD code, REFLEQS. The modified code was used to simulate both static and dynamic stalls on two- and three-dimensional wing-body configurations. Three-dimensional effect and flow physics are discussed. Further development and validation are proposed for Phase II.

92-05586



i

98 3 03 059

ACKNOWLEDGEMENTS

The authors would like to express their appreciation to the following individuals who contributed to this project.

- Major Daniel Fant of AFOSR for his constructive comments during the project;
- Dr. Ashok K. Singhal of CFDRC for his many helpful discussions and overall guidance;
- Drs. Mahesh M. Athavale, Yong G. Lai and Yu Jiang of CFDRC for their assistance in the debugging of the modified REFLEQS code, and for their many constructive discussions;
- Mr. Milind V. Talpallikar and Mr. Mark L. Ratcliff of CFDRC for their help in the grid generation and Dr. Z.J. Wang for his help in color graphics; and
- Ms. Shari M. Shea and Ms. Jennifer L. Swann of CFDRC for their skillful preparation of the typescript of this report.

TABLE OF CONTENTS

	<u>Page</u>
PROJECT SUMMARY	i
ACKNOWLEDGEMENTS	ii
NOMENCLATURE	xii
1. INTRODUCTION	1
1.1 Dynamic Stall Phenomenon and Its Significance	1
1.2 Literature Review	3
1.2.1 Computational Approach	4
1.2.2 Experimental Approach	6
1.3 Phase I Study and Its Merits	9
1.3.1 Why Pressure-Based Algorithm ?	9
1.3.2 Merits of the Present Methodology	11
1.5 Outline of the Report	15
2. PRESSURE-BASED METHODOLOGY	16
2.1 Governing Equations and Transformation	16
2.2 Discretization of Governing Equations	19
2.3 Pressure-Velocity Coupling	25
2.4 Solution Algorithm	29
2.5 Turbulence Modeling	30
2.6 Grid Generation	31
2.7 Boundary Conditions	33
2.7.1 Solid Boundary	33
2.7.2 Symmetric Boundary	33

TABLE OF CONTENTS (Cont.)

	<u>Page</u>
2.7.3 Far Field Boundary	34
2.7.4 Periodic Boundary	34
3. PROPOSED NEW METHODOLOGIES AND IMPROVEMENTS	35
3.1 High-Order TVD Schemes	36
3.2 Newton's Iteration Technique	39
3.3 Hyperbolic Pressure Correction	40
4. TWO-DIMENSIONAL STATIC AND DYNAMIC STALLS	44
4.1 Steady, Inviscid Transonic and Supersonic Flows Past a NACA 0012 Airfoil	44
4.2 Steady, Viscous Transonic Flow Over a NACA 0012 and an ARE 2822 Airfoil	48
4.2.1 NACA 0012 Airfoil	51
4.2.2 RAE 2822 Airfoil	55
4.3 NACA 0015 Airfoil Undergoing Constant Rate Pitching Motions	60
4.4 NACA0012 Undergoing Oscillatory Pitching Motion at Transonic Conditions	66
4.5 Parametric Effect on Dynamic Stall on the Airfoils	68
5. THREE-DIMENSIONAL STATIC AND DYNAMIC STALLS ON THE WINGS	80
5.1 Steady Flow over Rectangular Wings	80
5.2 Static and Dynamic Stalls on a Rectangular Wing	88
5.3 Static and Dynamic Stalls on a Forward Swept Wing	103

TABLE OF CONTENTS (Cont.)

		<u>Page</u>
5.4	Dynamic Stall on a Swept Back Wing	117
5.5	Static and Dynamic Stalls on a Delta Wing	125
6.	CONCLUSIONS AND RECOMMENDATIONS	133
6.1	Conclusions	133
6.2	Recommendations for Future Work	134
7.	REFERENCES	142

List of Figures

		<u>Page</u>
1-1.	Sketches of Flow Fields During Dynamic Stall	2
1-2.	Reflection and Propagation of Shock Wave in One-Dimensional Tube Calculated by Density- and Pressure-Based Methods	12
2-1	Curvilinear Coordinates and Finite-Volume Representation	21
2-2.	An O-H Grid Around a Rectangular Wing with NACA0012 Cross-Section	32
3-1.	Mach Number Calculated Along a Converging-Diverging Nozzle Length by Upwind, Central, and TVD Schemes with Pressure-Based Method	37
3-2.	1-D Shock Tube Problem by TVD Scheme with Pressure-Based Method	38
4-1.	Local View of a 100 x 50 O-Grid Around a NACA0012 Airfoil for Inviscid Computations	45

List of Figures (Cont.)

<u>Figure</u>	<u>Page</u>
4-2. Comparison of the Present Pressure-Based TVD, Yee's Density-Based TVD and ARC2D for Supersonic Flow Over a NACA0012 Airfoil at $M_\infty = 1.2$ and $\alpha = 7.0^\circ$	
4-3. Comparison of the Present Pressure-Based TVD, Yee's Density-Based TVD and ARC2D for Supersonic Flow Over a NACA0012 Airfoil at $M_\infty = 1.8$ and $\alpha = 7.0^\circ$	47
4-4. Transonic Flow Over a NACA0012 Airfoil at $M = 0.8$ and $\alpha = 1.25^\circ$ by the Present Pressure-Based TVD Scheme	49
4-5. Convergence History of Regular Iteration Method and Newton's Iteration Method with Hyperbolic Pressure Correction for Inviscid Flow Over a NACA0012. Grid 100×50 , $M_\infty = 0.8$, and $\alpha = 1.25^\circ$	50
4-6. Grid Distribution (200×63) for a NACA0012 Airfoil for Viscous Transonic Computation	52
4-7. Results of Viscous Transonic Flow Over a NACA0012 Airfoil at $\alpha = 1.49^\circ$, $M_\infty = 0.7$, and $Re = 9 \times 10^6$	53
4-8. Results of Viscous Transonic Flow Over a NACA0012 Airfoil at $\alpha = 8.34^\circ$, $M_\infty = 0.55$, and $Re = 9 \times 10^6$	54
4-9. Results of Viscous Transonic Flow Over a NACA0012 Airfoil at $\alpha = 2.26^\circ$, $M_\infty = 0.749$, and $Re = 9 \times 10^6$	56
4-10. Lift Coefficients (C_L) vs. Angle of Attack for Transonic Flow Over a NACA0012 at $M_\infty = 0.7$ and $Re = 9 \times 10^6$	57
4-11. O-Grid (144×64) Around RAE 2822 Airfoil for Viscous Transonic Computations	58
4-12. RAE 2822 Airfoil Surface Pressure Distribution at $M_\infty = 0.749$, $Re = 9 \times 10^6$ and $\alpha = 1.943^\circ$ (Case 1)	59

List of Figures (Cont.)

<u>Figure</u>	<u>Page</u>
4-13. RAE 2822 Airfoil Surface Pressure Distribution at $M_\infty = 0.725$ $Re = 6.5 \times 10^6$ and $\alpha = 2.79^\circ$ (Case 1)	61
4-14. Local View of a 200×77 O-Grid Around NACA0015 Airfoil for Constant Pitch-Rate Simulation	63
4-15. Comparison of Computed Flow Field with Experiment for NACA0015 Airfoil at Constant-Rate Pitch, $Re = 45,000$, $k = 0.2$, 200×77 grid	64
4-16. Comparison of Computed Flow Field with Experiment for NACA0015 Airfoil at Constant-Rate Pitch, $Re = 45,000$, $k = 0.4$, 200×77 grid	65
4-17. Lift Coefficient for a NACA0012 Airfoil Undergoing Oscillatory Motion, $Re = 4.8 \times 10^6$, $M_\infty = 0.6$, and $k = 0.081$	67
4-18. Pressure Coefficients for a NACA0012 Airfoil Undergoing Oscillatory Motion, $Re = 4.8 \times 10^6$, $M_\infty = 0.6$, and $k = 0.162$	69
4-19. Density Contours Around a NACA0012 Airfoil Harmonically Pitching About Quarter Chord, $Re = 4.8 \times 10^6$, $M = 0.6$, and $k = 0.162$	70
4-20. Comparison of Density Contours between the Present Prediction and Experiments of Carr <i>et al.</i> for Steady Flow over a NACA0012 at $M_\infty = 0.4$, $\alpha = 0.0$, and $Re = 5.4 \times 10^6$	72
4-21. Comparison of Density Contours between the Present Prediction and Experiments of Carr <i>et al.</i> for Steady Flow over a NACA0012 at $M_\infty = 0.3$, $\alpha = 10.78^\circ$, and $Re = 5.4 \times 10^6$	73
4-22. Density and Streamlines During an Oscillation Cycle for NACA0012 at $M_\infty = 0.3$, $f = 21.64\text{Hz}$, $k = 0.05$, $Re = 5.4 \times 10^5$, $\alpha_m = 10^\circ$ and $\Delta\alpha = 10^\circ$	75
4-23. Density Contours and Experimental Fringes Around a NACA0012 During the Reattachment Process of an Oscillating Cycle. $M_\infty = 0.3$, $f = 21.64\text{Hz}$, $k = 0.05$, $Re = 5.4 \times 10^5$, $\alpha_m = 10^\circ$ and $\Delta\alpha = 10^\circ$	78

List of Figures (Cont.)

<u>Figure</u>	<u>Page</u>
4-24. C_L vs α for $Re = 5.4 \times 10^5$, $M_\infty = 0.3$, $f = 21.64$ Hz, and $k = 0.05$	79
5-1. Pressure Coefficient Comparisons. NACA0012 Airfoil Section, Large-Aspect-Ratio, (TR = 1.0, $M_\infty = 0.5$, $\alpha = 0^\circ$, and $Re = 3 \times 10^6$)	81
5-2. Rectangular NACA0015 Wing and Grid Distribution	83
5-3. Surface Pressure Distributions for Several Spanwise Stations and Comparison with Experimental Data for NACA0015 Rectangular Wing. $M_\infty = 0.16$, $\alpha = 11^\circ$ and $Re = 2 \times 10^6$	85
5-4. Surface Oil-Flow Pattern (Simulated) for the Rectangular NACA0015 Wing. $M_\infty = 0.16$, $\alpha = 11^\circ$ and $Re = 2 \times 10^6$	86
5-5. Three-Dimensional View of Particle Traces	87
5-6. Surface Pressure Contours for the Rectangular NACA0015 Wing. $M_\infty = 0.16$, $\alpha = 11^\circ$ and $Re = 2 \times 10^6$	89
5-7. Static and Dynamic Stalls on a Rectangular Wing of a NACA0015 at 0.98c Inboard. $Re = 42,000$ and $M = 0.02$	91
5-8. Particle Traces on the Upper Surface of NACA0015 Rectangular Wing and at Several Spanwise Locations for Static Stall. $Re = 42,000$, $M = 0.02$ and $\alpha = 18.3^\circ$	92
5-9. Particle Traces on the Upper Surface of NACA0015 Rectangular Wing and at Several Spanwise Locations for Dynamic Stall. $Re = 42,000$, $M = 0.02$ and $\alpha = 18.3^\circ$ Downstroke (\downarrow)	93
5-10. Flow Patterns over One Pitching Cycle at 0.67c Inboard. $Re = 42,000$, $k = 1.0$ (experimental), $K = 0.93$ (computation)	95
5-11. Flow Patterns over One Pitching Cycle at 0.67c Inboard, 3D Rectangular Wing, $Re = 42,000$, $k = 0.93$	96

List of Figures (Cont.)

<u>Figure</u>	<u>Page</u>
5-12. Oil-Flow Patterns (Simulated) and Pressure Contours on the Upper Surface of a Rectangular NACA0015 Wing over One Pitching Cycle. $Re = 42,000$, $k = 0.93$, $\alpha_m = 15^\circ$ and $\Delta\alpha = 10^\circ$	98
5-13. Lift Coefficient versus Angle of Attack for a Rectangular NACA0015 Wing under Oscillating Motion. $Re = 42,000$, $M = 0.02$ and $k = 0.10$	102
5-14. Top View of the Computational Grid and Boundary Conditions on a 30° Forward Swept Wing	104
5-15. Present Calculations and Flow Visualizations for a 3D Forward Swept Wing at $\alpha = 3^\circ$, $Re = 40,000$	106
5-16. Present Calculations and Flow Visualizations for a 3D Forward Swept Wing at $\alpha = 15^\circ$, $Re = 40,000$	107
5-17. Present Calculations and Flow Visualizations for a 3D Forward Swept Wing at $\alpha = 27^\circ$, $Re = 40,000$	108
5-18. Particle Traces on a 30° Forward Swept Wing, Top View	109
5-19. Particle Traces on a 30° Forward Swept Wing, Side View	110
5-20. Oil Flow Pattern (Simulated) on a 30° Forward Swept Wing at $Re = 4 \times 10^4$, $\alpha = 27^\circ$ and $M = 0.02$	111
5-21. Oil Flow Pattern (Simulated) and Particle Traces for a 30° Forward Swept Wing Undergoing Oscillatory Pitching. $Re = 4 \times 10^4$, $k = 1.0$, $\alpha_m = 10^\circ$ and $M = 0.02$	113
5-22. Oil Flow Pattern (Simulated) and Particle Traces for a 30° Swept Back Wing Undergoing Oscillatory Pitching. $Re = 4 \times 10^4$, $k = 1.0$, $\alpha_m = 10^\circ$ and $M = 0.02$	118

List of Figures (Cont.)

<u>Figure</u>	<u>Page</u>
5-23. Comparison of Oil-Flow Patterns (Simulated) on the Upper Surface of a 30° Swept Back Wing, a Rectangular wing, and a 30° Forward Swept Wing During Downstroke of an Oscillation Cycle around $\alpha = 22^\circ$	123
5-24. Comparison of Oil-Flow Patterns (Simulated) on the Upper Surface of a 30° Swept Back Wing, a Rectangular wing, and a 30° Forward Swept Wing During Downstroke of an Oscillation Cycle around $\alpha = 8^\circ$	124
5-25. Lift Coefficients versus α for a Rectangular wing, a 30° Swept Back Wing, and a 30° Forward Swept Wing Undergoing Oscillatory Pitching	125
5-26. Configuratin of a 45° Delta Wing	127
5-27. Surface Oil-Flow Patterns (Simulated) for a Static Delta Wing at $\alpha = 5^\circ, 10^\circ, 15^\circ$ and 20° , $Re = 17,000$, and $M_\infty = 0.02$	129
5-28. Leading Edge Vortices Formed Above a Delta Wing	130
5-29. Particle Traces Around a Static Delta Wing, Side View. $M = 0.02$, $\alpha = 15^\circ$, and $Re = 17,000$	131
5-30. Particle Traces Around a Static Delta Wing, Top View. $M = 0.02$, $\alpha = 15^\circ$, and $Re = 17,000$	132
5-31. Oil-Flow Patterns (Simulation) for on a 45° Swept Delta Wing Undergoing Oscillatory Pitching. $Re = 1.7 \times 10^4$, $k = 0.24$, $M = 0.02$, $\alpha_m = 15^\circ$, and $\Delta\alpha = 10^\circ$	133
6-1. Typical Vortical Structure over a Double-Delta Wing at High Angle of Attack	139

List of Figures (Cont.)

<u>Figure</u>		<u>Page</u>
6-2.	Some Novel Control Concepts	139
6-3.	Potential Vortex Control Concepts for Phase II Study	140

NOMENCLATURE

A_{nb}, A_{cnb}	Link coefficients for finite difference equations
c	chord length
C	convective flux
C_L	lift coefficient
C_p	pressure coefficient
C-O	Chakravarthy-Osher third-order scheme
D	diffusive flux
f	oscillation frequency of the airfoil
g^{ij}	matrix tensor
G	mass flux over a control volume surface
H	Total enthalpy
J	Jacobian of transformation
k	raduced-frequency parameter, $k = \omega c / 2U_\infty$, or $k = \dot{\alpha} c / U_\infty$
M_∞	free-stream Mach number
p	pressure
Re	Reynolds number, $Re = \rho_\infty U_\infty c / \mu_\infty$
S	source term
TVD	Total Variation Diminishing
T	temperature
t	time
u_i	velocity component in Cartesian coordinates (u, v, w)
U_i	contravariant velocity component
U_∞	free-stream velocity
x_i	Cartesian coordinates (x, y, z)

Greek Symbols

α	angle of attack, degrees
α_m	mean angle of attack, degrees
$\Delta\alpha$	amplitude of angle of attack variation, degrees
Γ	thermal conductivity
ξ^i	general curvilinear coordinates (ξ, η, ζ)
μ	dynamic viscosity
ρ	density
ϕ	general dependent variable, or spacial accuracy parameter
ω	circular frequency, $2\pi f$
τ	time in transformed space

Subscripts

e,w,n,s,h,l	the value at the east, west, north, south, high or low face of a control volume
E,W,N,S,H,L	the value at the center of east, west, north, south, high or low control volume
u_i, H	with respect to u_i equation or H equation
∞	conditions in free-stream

Superscripts

o	previous time level
------	---------------------

1. INTRODUCTION

1.1 Dynamic Stall Phenomenon and Its Significance

Dynamic stall is a complex physical event induced by a large amplitude motion of aerodynamic bodies. It is a phenomenon characterized by the shedding and passage over the upper surface of a lifting surface of vortex-like disturbances. Associated with this phenomenon is the generation of intense vorticity near the nose of the body, which occurs as the pitching of the lifting surface dynamically surpasses its stall angle of attack. This vorticity increases the circulation of the flow and thus the lift force acting on the body. As a result, large unsteady aerodynamic forces are generated from which the lift, drag and moment coefficients greatly exceed their maximum static counterparts. The unsteady effects of dynamic stall are usually dominated by turbulent flow and the production of large scale vortices. The dynamic stall events will either proceed with the generation of weaker vortices if the body remains pitched above its static stall angle of attack, or terminate if the body returns to an angle of attack sufficiently small for reattachment of the flow. Figure 1-1 illustrates the typical flow field during dynamic stall. Excellent reviews on the subject have been presented by McCroskey^{1,2} and Carr.³

Dynamic stall is of importance in various aerodynamic applications including aircraft maneuverability, helicopter rotors, and wind turbine. For example, when the dynamic stall appears in the retreating blade of a helicopter rotor, it produces a loss of lift, thus an increase in power is required which in turn increases the pitching loads and vibratory stresses. Therefore, significant efforts have been devoted to understand and eliminate the undesirable effects associated with dynamic stall on helicopter rotors. Recent efforts are exploring the possibility of utilizing the unsteadiness of the flow field to enhance aircraft performance and to attain the sustained dynamic maneuvering in the post-stall flight regime. For

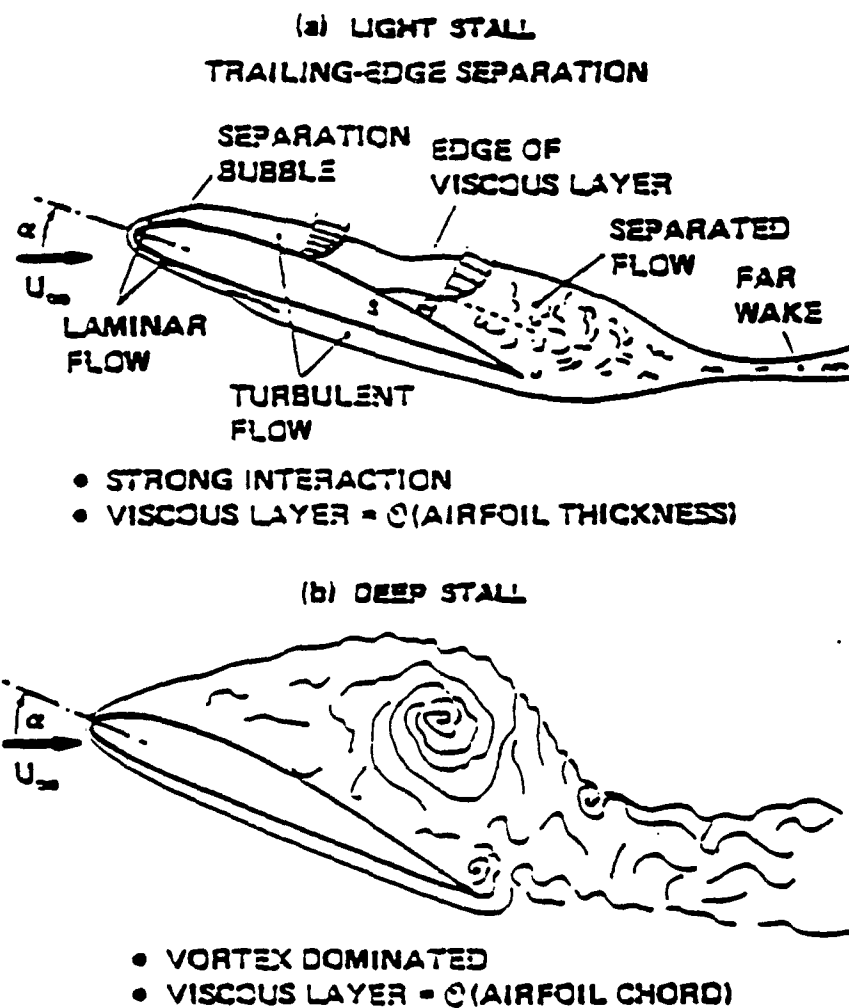


Figure 1-1. Sketches of Flow Fields During Dynamic Stall

(a) Light Stall; and (b) Deep Stall¹

example, Robinson and Luttges^{4,5} have analyzed the repetitive interaction of the dynamic stall vortices as a means of maintaining flow attachment to increase lift at high angles of attack. They also correlated this phenomenon as a function of the driving parameters involved, *i.e.*, pivot location, airfoil shape, Reynolds number and mean angle of attack. Indeed, the impetus to exploit the energetic nature of large vortices to potentially enhance performance has already been demonstrated.¹ However, it is clear that before such a realistic usage is possible, extensive studies must be undertaken to expand our knowledge of fundamental aspects.

1.2 Literature Review

Dynamic stall is much more difficult to analyze and predict than static stall because it depends on many parameters, including:

- airfoil pitch rate, pitch amplitude, and pitch axis location;
- mean and maximum angles of ramp or oscillation;
- airfoil geometry, including thickness, leading edge curvature, and camber;
- wing or blade tip shape;
- free stream Reynolds and Mach numbers.

In the past, dynamic stall research has proceeded along several avenues: analytical, experimental, and computational. Analytical methods were used primarily to complement both the experimental and computational methods. Due to the complexity of the flow field, analytical methods were often found not self-sufficient, and as such will not be discussed herein.

As this study concerns computational investigation of dynamic stall phenomenon, the related works on computational approach, experimental visualizations, and

three-dimensional effect have been reviewed, and briefly summarized in the following three sections.

1.2.1 Computational Approach

The recent advancement of Computational Fluid Dynamics (CFD) has provided a prediction capability that was unattainable only a few years ago. The earliest computational investigations of dynamic stall appeared in the 1970s and early 1980s with the works of Mehta,⁶ Gulcat,⁷ and Sankar⁸⁻¹⁰ as the most representative ones. In 1977 Mehta⁶ solved the Navier-Stokes equations for laminar flows to determine the flow field around an oscillatory NACA0012 airfoil. Although the flow field was computed in detail, it was limited to low Reynolds number flows and required large amounts of computer time.

Relatively recently, Sankar and his co-workers⁸⁻¹⁰ used the unsteady, compressible, Reynolds averaged Navier-Stokes equations in the computation of laminar and turbulent flow fields around oscillating airfoils. Their aerodynamic load prediction agreed with the experimental data during the upstroke prior to the stall. Yet, they could not resolve the details in the post-stall regime.

In the mid 1980s, Wu and his co-workers¹¹⁻¹³ developed a method for computing massively separated unsteady incompressible flow fields. This method was based on the velocity-vorticity formulation of the Navier-Stokes equations which consists of the vorticity transport equation and an integral equation for velocity. The results were consistent with experimental data.

Cebeci, *et al.*^{14,15} have reported extensive investigations using an interactive approach which solves inviscid and boundary-layer equations and allows them to influence each other in an iterative manner. This method was developed and

tested for steady flows and was used in a quasi-steady manner to examine the evolution of the flow behavior around oscillatory airfoils operating in light stall conditions.¹⁵

Visbal and Shang¹⁶⁻¹⁹ presented a series of papers describing the development and application of a compressible Navier-Stokes solver. These papers address many of the physical variables associated with dynamic stall. Rumsey and Anderson²⁰ applied an upwind-biased, implicit approximate factorization algorithm to several unsteady flows on dynamic meshes. They used the thin-layer form of the compressible Navier-Stokes equations to solve both laminar and turbulent flows over airfoils pitching about the quarter chord. Shida and Kuwahara²¹ modeled the time-accurate static stall of a NACA 0012 airfoil with artificial viscosity that permitted resolution of a small scale structure. Shida, *et al.*²² further modeled the dynamic stall of the NACA 0012 airfoil using a time-accurate unsteady Navier-Stokes equation solver and computed the flow over the NACA 0012 airfoil oscillatory in pitch at $M = 0.3$, $Re = 4 \times 10^6$.

Ono²³ simulated the dynamic stall process on a two-dimensional NACA0012 airfoil oscillating in pitch. The qualitative agreement with experimental data was fairly good, but quantitative agreement wasn't satisfactory. Currier and Fung²⁴ conducted a numerical study to assess the sensitivity of the separating boundary layer to the transition location. They found that the bursting of the separation bubble at the airfoil leading edge is the onset mechanism for most of the dynamic stalls. Jang *et al.*²⁵ applied the implicit approximate factorization solution algorithm of Beam-Warming²⁶ to the computation of the unsteady boundary layers on a rapidly pitching NACA0012 airfoil and found good agreement with the unsteady pressure measurements of Landon²⁷.

The most recent computational studies have been presented by Shrewsbury and Sankar²⁸, Grohsmyer *et al.*²⁹, and Ghia *et al.*³⁰

1.2.2 Experimental Approach

Experimental data has provided the basis for the current understanding of the dynamic flowfield. Most of the experimental data for unsteady separated flow over airfoils have been obtained for oscillatory airfoils undergoing relatively small sinusoidal pitch oscillations ($\pm 1 - \pm 10$ degrees) about a relatively small mean angle of attack ($0 - 15^\circ$) as typified by the experiments reported by McCroskey and Philippe,³¹ McAlister and Carr,³² and Martin, *et al.*,³³. A limited amount of experimental data have been obtained for airfoils undergoing constant pitching rate motions up to moderate angles of attack of at least 30° . These works include the study of Harper and Flanigan,³⁴ who obtained force balance data on a small aircraft model pitching up to 30° , the work of Ham and Garelick,³⁵ who measured surface pressure on an airfoil pitching up to 30° , and the work of Francis, *et al.*³⁶ who measured surface pressure on an airfoil pitching up to 60° . None of the above mentioned works contain any flow visualization data. Deekens and Kuebler³⁷ obtained flow visualization data from a NACA 0015 airfoil and observed the dynamic leading-edge separation phenomenon for several low Reynolds numbers (less than 3×10^4) and non-dimensional pitch rates up to 0.26. Daley³⁸ obtained leading-edge dynamic stall data for Reynolds numbers up to 3×10^5 and non-dimensional pitch rates up to 0.06. Walker, *et al.*³⁹ obtained flow visualization data along with hot wire data on a NACA 0015 airfoil undergoing constant pitch rate motions. These data were obtained for a Reynolds number on the order of 4.5×10^4 and non-dimensional pitch rates up to 0.30.

Compressibility effects have been addressed experimentally during the last few years. Results of Schlieren studies by Chandrasekhara and Carr⁴⁰ on an oscillatory

airfoil have indicated that compressibility effects set in at $M = 0.3$. Further studies by Chandrasekhara and Ahmed⁴¹ using LDV have shown the formation of a separation bubble near the leading edge prior to the formation of a dynamic stall vortex. Studies using the PDI technique by Carr, *et al.*^{42,43} have confirmed the presence of the separation bubble and have shown that the flow gradients are slow to develop in the oscillatory case compared to the steady-state resulting in the delay of stall known as dynamic stall. Ahmed and Chandrasekhara⁴⁴ carried out a detailed study of the reattachment process of dynamic stall flow over an oscillatory airfoil. They have found that reattachment progresses through a separation bubble, which change size during the process and disappears at a low angle of attack.

Chandrasekhara and Brydges⁴⁵ documented the effects of increasing amplitude on an oscillatory airfoil in both compressible and incompressible flows and showed that larger amplitudes resulted in vortex retention at higher angle of attack for a given Mach number and reduced frequency.

1.2.3 Three-Dimensionality of Flow

The effect of three-dimensionality on aircraft dynamic stall is significant and must be included at the onset if a full representation of dynamic stall on an aircraft is to be attained. The effect of pitch oscillation on a delta wing was studied experimentally by Gad-el-Hak and Ho.⁴⁶ They found significant interaction between the vortices shed from the leading edge and those shed during the dynamic stall process. They also studied the low Reynolds number, and time-dependent flows around the delta and swept wings⁴⁷ and found that on the rectangular wing, the leading edge separation vortex convects downstream, while it is stationary during part of the angle on the swept wing. On the delta wing, the leading edge vortex does not convect, rather it experiences a grow-decay cycle.

Adler and Luttges⁴⁸ obtained flow visualization for a rectangular wing with an aspect ratio of two, and showed that flow features were similar to two-dimensional stalls appearing within a chord length of the tip. Carta⁴⁹ studied the effect of sweep on an oscillatory airfoil and found that sweep effects appeared near the leading edge, and that there were large phase shifts in the lift results for the swept and unswept wing, but only if dynamic stall had occurred in the cycle. Wagner⁵⁰ observed that the location and size of the tip-vortex changes significantly with small variation in the amplitude of oscillation.

In their measurement of unsteady pressure distribution on a pitching rectangular wing, Robinson and Wissler⁵¹ observed the interaction between the dynamic stall vortex and the tip vortex resulting in prolonging the passage of the stall vortex which in turn enhances the value of sectional lift coefficient. Ashworth, *et al.*⁵² studied three-dimensional flow field about a forward swept NACA 0015 wing. They found that strong helical tip flow vortices dominated most of the observed flow structures near the wing tip across all test conditions, and the far inboard span locations were dominated by flows related to the leading edge vortex. St. Hilaire, *et al.*^{53,54} examined the effect of sweep on an oscillatory wing model. They found that sweep tends to delay the onset of dynamic stall and slightly reduces the magnitude of the hysteresis loop. Garta⁵⁵ found that near the leading edge the sweep effect is significant, and there are phase shifts in the aerodynamic forces between swept and unswept wings when dynamic stall has occurred in the cycle.

Ashworth, *et al.*^{56,57}, Luttges and M.C. Robinson⁵⁸, and Adler and Luttges⁵⁹ have made a series of studies on three-dimensional vortex flows created by sinusoidal oscillation of wings.

Salari and Roache⁶⁰ investigated the influence of sweep on the deep dynamic stall of a rapidly pitching swept wing using numerical simulations. They found that sweep

tends to delay the onset of dynamic stall and reduce the magnitude of unsteady aerodynamic loads. Chaderjian and Guruswamy⁶¹ used a zonal grid approach to simulate unsteady transonic viscous flow about a three-dimensional rectangular wing with an oscillatory angle of attack. Computed real and imaginary pressure coefficients compared well with the experimental values.

1.3 Phase I Study and Its Merits

In this project we developed and demonstrated the high-order accurate and efficient pressure-based algorithm for predicting the quantitative features of separating unsteady flows, such as dynamic stall in the two- and three-dimensional stationary and maneuvering bodies of aerospace vehicles. The major innovations and contributions to the state-of-the-art of the Computational Fluid Dynamic of the pressure-based method are:

1. Development of high-order TVD scheme for the pressure-based algorithm;
2. Newton's iteration technique for fast convergence; and
3. Novel concept of hyperbolic pressure correction equation to improve solver efficiency.

1.3.1 Why Pressure-Based Algorithm ?

Most aerospace vehicles tend to operate in the transonic regime where the flow field is primarily subsonic with regions of supersonic flows. This often gives rise to complex fluid physics such as steady and time dependent vortical flow, shocks and separations. A solution algorithm is needed which is equally effective for a high-speed compressible flow regime as well as for a separated and stagnated mildly compressible regime.

Current state-of-the-art of CFD technology can be divided into two groups: density-based methods and pressure-based methods. In the density based approach, density is treated as a transport variable in the continuity equation. Pressure is derived from the equation of state. The density-based algorithms have been widely used for compressible and external flows. The merit of this approach lies in its ability to obtain high order accuracy, which is accomplished by applying recently developed high resolution schemes, such as TVD⁶²⁻⁶⁶, ENO^{67,68}, MUSCL⁶⁹ and PPM⁷⁰. Indeed, the density-based method incorporates the non-linear wave properties into the numerical solutions in the form of Riemann problems and characteristic equations. This leads to algorithms which are robust and accurate for high-speed compressible flows⁷¹.

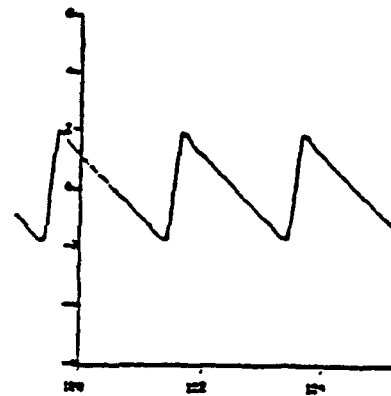
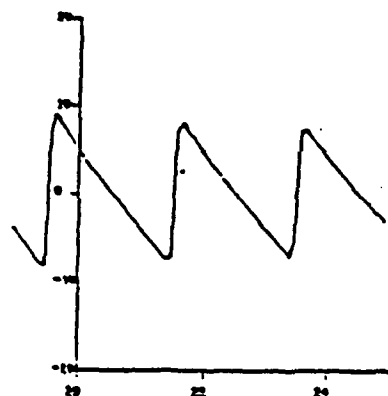
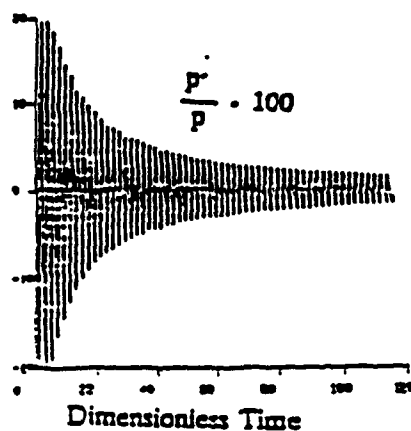
The accuracy and efficiency of the density-based methods, however, breaks down at low Mach numbers and for recirculating flows. Here acoustic wave speed becomes very high relative to the fluid velocity, and CFL restriction requires a very small time step. Whereas in the incompressible flow limit, density is constant and is independent of pressure, so that the pressure field in the momentum equation cannot be extracted from the density field, and density-based methods fail. To date, the methods have rarely been used for incompressible or low-speed turbulent and recirculating flows. Artificial compressibility has to be introduced in the continuity equation to use the density based approach for incompressible flows.

Pressure based methods, on the other hand, are effectively characterized by combining the continuity and momentum equations to form a Poisson-like equation for pressure or pressure correction. Here any change in density is then considered a function of pressure via an equation of state. As a result, it can handle both compressible and incompressible flows with equal accuracy and efficiency. This approach has been very successful in complex, recirculating and turbulent flows.

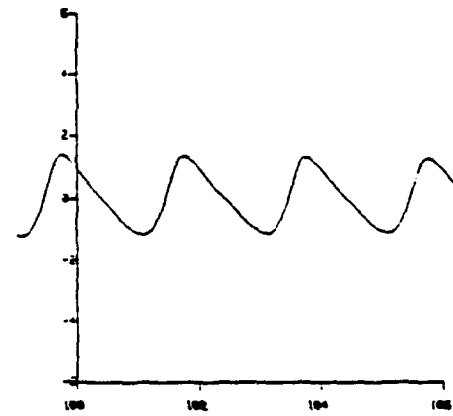
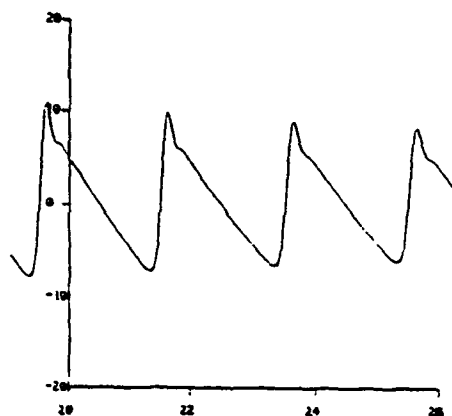
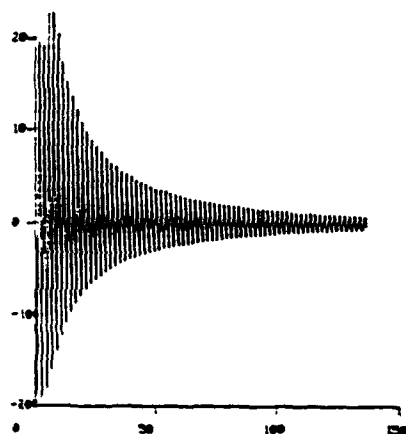
The governing equations in the pressure-based approach are usually solved in a segregated manner (one variable at a time). Instead of solving block matrix equations in a factorized form, as in the density based methods, a single equation matrix is solved on the entire computational domain. For elliptic flow problems, as in a dynamic stall case, it is very efficient and requires less computational storage. Recent assessment of the pressure-based algorithms⁷², for one-dimensional fast transient and resonant compressible flows with shocks, shows a very promising future for the method in high-speed flows. In Figure 1-2 results of the compressible flow with moving shock in a resonant pipe calculated by density and pressure based methods are displayed. The selected test case is very challenging in that it requires the numerical method to be non-dissipative and non-dispersive, be able to capture shock without wiggles, and be able to keep shock amplitude for a long time. As seen from the Figure 1-2, the proposed pressure-based method is as accurate as density-based method.

1.3.2 Merits of the Present Methodology

There are several merits of the presently proposed methodology. First, the present pressure-based approach has the advantage of being a unified methodology. It can be applied to a wide variety situations: unsteady and steady flows; low speed subsonic, transonic, supersonic and hypersonic flows; perfect and real gas; viscous and inviscid flows; single and multiple spatial dimensions; simple and complex geometries; internal and external flows; *etc.* Secondly, since the convective terms in the governing equations are modeled by a high order TVD scheme, it requires no user-specified dissipation terms. In contrast, most of the existing pressure-based codes require user-specified dissipation, which can result in lost accuracy of the solution not only near discontinuities but also across the computational domain.



C-O Third-Order TVD Scheme, Density-Based Method



C-O Third-Order TVD Scheme, Pressure-Based Method

Figure 1-2. Reflection and Propagation of Shock Wave in One-Dimensional Tube Calculated by Density- and Pressure-Based Methods

C-O = Chakravarthy-Osher Third-Order Scheme⁶⁵

Thirdly, by strongly coupling the velocity and pressure fields, the presently developed Newton's iteration technique greatly improves the numerical convergence rate and does not require the difficult evaluation of Jacobian matrix. Finally, proposed innovative hyperbolic form of the pressure correction equation can be solved more efficiently than the commonly used elliptic equation form.

1.4 Technical Objectives and Approach

The objective of the proposed project is to develop a high order TVD scheme and efficient pressure-based algorithm and to demonstrate their capability for a model problem of stall flow on static and dynamic maneuvering three-dimensional wings in subsonic condition. The specific objectives of Phase I effort include:

- Develop a conservative and consistent formulation of third-order TVD scheme applicable for conservative and primitive variables;
- Develop Newton's iteration technique for a complete set of primitive variables (u , v , w , p , H , k , ϵ , ...) solved by a "whole-field" rather than Block-TDMA type or Block-Gauss-Seidel type solvers. Utilize the maximum available information from Riemann solutions and entropy condition;
- Perform and evaluate the effectiveness of hyperbolized form of pressure correction equation; and
- Use the modified code to investigate the flow physics of dynamic stall on a static and dynamic maneuvering three-dimensional wing in subsonic flow.

The proposed methodology has been partially evaluated on a one-dimensional nonlinear acoustic problem with excellent results⁷². The challenge for this project is

to extend it to multidimensional flows and retain the high numerical accuracy for low and high Reynolds numbers, and for sub- and supersonic flows.

The development of the above new methodologies has been achieved by adapting and modifying an existing advanced CFD code, REFLEQS.⁷³⁻⁷⁵

The REFLEQS code has been developed by CFDRC personnel. Its main capabilities/methodologies directly related to the present work are:

1. Solution of two- and three-dimensional Navier-Stokes equations for compressible and incompressible flows;
2. Cartesian, polar, and non-orthogonal body-fitted-coordinates and body-conforming moving grid;
3. Fully implicit and strong conservation formulation;⁷⁶
4. Central differencing with damping terms;
5. Second-order time accurate formulation;
6. Four turbulence models: Baldwin-Lomax model; Standard $k-\epsilon$; multiple-scale model of Chen;⁷⁷ and Low Re $k-\epsilon$ model of Chien;
7. Symmetric and periodic whole field solver;
8. Pressure-based solution algorithms, with an enhanced variant of SIMPLEC, SIMPLE, and PISO; and
9. User friendly pre-processor and graphical post-processor.

Significant emphasis has been placed on the systematic and quantitative validation of REFLEQS. It has already been validated for over thirty benchmark problems. References 73 through 75 describe some of these problems.

1.5 Outline of the Report

The next section (Section 2) describes the basic pressure-based methodology in current REFLEQS code. Section 3 presents the proposed improvements including high-order TVD schemes, Newton's iteration, and hyperbolization of pressure correction equation.

Section 4 presents the validation of the REFLEQS code on 2D airfoils for inviscid supersonic and transonic flows, and viscous transonic flow. Several dynamic stall conditions are also simulated. Section 5 describes the simulations and discusses flow physics of static and dynamic stalls on three-dimensional rectangular, forward swept, backward swept, and delta wings. Comparisons are made, wherever possible, with experimental data and visualization.

Finally, Section 6 presents the summary of the present study and recommendations for further investigations. Preliminary recommendations for the SBIR Phase II study are also outlined. Further selection and elaboration of these recommendations will be presented in the proposal for Phase II work.

2. PRESSURE-BASED METHODOLOGY

The objective of the present study is to develop advanced pressure-based methodology to study the physics of three-dimensional dynamic stall. To accomplish the above objective, an existing advanced CFD code, REFLEQS, will be modified by implementing the proposed techniques. This section will briefly describe the basic pressure-based methodology available in REFLEQS. The proposed more advanced techniques and their uniqueness will be presented in the next section.

2.1 Governing Equations and Transformation

The flow governing equations are the compressible, Reynolds-averaged, Navier-Stokes equations. They can be written in a Cartesian tensor form as:

$$\frac{\partial \rho}{\partial t} + \frac{\partial}{\partial x_j} (\rho u_j) = 0 \quad (2.1)$$

$$\frac{\partial}{\partial t} (\rho u_i) + \frac{\partial}{\partial x_j} (\rho u_j u_i) = -\frac{\partial p}{\partial x_i} + \frac{\partial}{\partial x_j} \left[\mu \left(\frac{\partial u_j}{\partial x_i} + \frac{\partial u_i}{\partial x_j} - \frac{2}{3} \frac{\partial u_k}{\partial x_k} \delta_{ij} \right) \right] \quad (2.2)$$

$$\frac{\partial (\rho H)}{\partial t} + \frac{\partial}{\partial x_j} (\rho u_j H) = \frac{\partial p}{\partial t} + \frac{\partial}{\partial x_j} \left(\Gamma \frac{\partial T}{\partial x_j} \right) + \frac{\partial}{\partial x_j} \left[\mu u_i \left(\frac{\partial u_j}{\partial x_i} + \frac{\partial u_i}{\partial x_j} - \frac{2}{3} \frac{\partial u_k}{\partial x_k} \delta_{ij} \right) \right] \quad (2.3)$$

where ρ is density, u_i is the Cartesian velocity component, p is the pressure, H the total enthalpy, T the temperature, and t the time. x_i is the Cartesian coordinate,

$$x_1 = x, \quad x_2 = y, \quad x_3 = z \quad (2.4)$$

μ and Γ are the effective dynamic viscosity and effective thermal conductivity, respectively:

$$\mu = \mu_l + \mu_t \quad (2.5)$$

$$\Gamma = \Gamma_l + \Gamma_t \quad (2.6)$$

The subscript l denotes laminar quantity, and t the turbulent quantity.

For most engineering applications, including the present problem, Cartesian coordinates are rarely adequate in describing the geometric configuration. Thus, a generalized coordinate mapping is introduced in the form

$$x = x(\xi, \eta, \zeta, \tau), \quad y = y(\xi, \eta, \zeta, \tau), \quad z = z(\xi, \eta, \zeta, \tau), \quad t = \tau \quad (2.7)$$

or simply

$$x_i = x_i(\xi^j, \tau), \quad t = \tau \quad (2.8)$$

where

$$\xi^1 = \xi, \quad \xi^2 = \eta, \quad \xi^3 = \zeta \quad (2.9)$$

The purpose of introducing temporal variation of the coordinates is to accommodate body-conforming moving coordinates.

Using the chain rule we have,

$$\frac{\partial}{\partial t} = \frac{\partial}{\partial \tau} + \frac{\partial \xi^j}{\partial t} \frac{\partial}{\partial \xi^j} \quad (2.10a)$$

$$\frac{\partial}{\partial x_i} = \frac{\partial \xi^j}{\partial x_i} \frac{\partial}{\partial \xi^j} \quad (2.10b)$$

By some manipulation, Equations 2.1 to 2.3 can be written in a strong conservation form, except pressure term:

$$\frac{\partial}{\partial t} \left(\frac{\rho}{J} \right) + \frac{\partial}{\partial \xi^j} \left(\frac{\rho U_j}{J} \right) = 0 \quad (2.11)$$

$$\begin{aligned} \frac{\partial}{\partial t} \left(\frac{\rho u_i}{J} \right) + \frac{\partial}{\partial \xi^j} \left(\frac{\rho U_j u_i}{J} \right) = & - \frac{1}{J} \frac{\partial \xi^j}{\partial x_i} \frac{\partial p}{\partial \xi^j} + \\ & \frac{\partial}{\partial \xi^k} \left[\frac{\mu}{J} \frac{\partial \xi^k}{\partial x_j} \left(\frac{\partial \xi^l}{\partial x_j} \frac{\partial u_i}{\partial \xi^l} + \frac{\partial \xi^l}{\partial x_i} \frac{\partial u_j}{\partial \xi^l} - \frac{2}{3} \delta_{ij} \frac{\partial u_l}{\partial \xi^m} \frac{\partial \xi^m}{\partial x_l} \right) \right] \end{aligned} \quad (2.12)$$

$$\begin{aligned} \frac{\partial}{\partial t} \left(\frac{\rho H}{J} \right) + \frac{\partial}{\partial \xi^j} \left(\frac{\rho U_j H}{J} \right) = & \frac{1}{J} \frac{\partial p}{\partial t} + \frac{\partial}{\partial \xi^k} \left(\frac{\Gamma}{J} \frac{\partial \xi^k}{\partial x_j} \frac{\partial \xi^l}{\partial x_j} \frac{\partial T}{\partial \xi^l} \right) \\ & + \frac{\partial}{\partial \xi^k} \left[\frac{\mu}{J} u_i \frac{\partial \xi^k}{\partial x_j} \left(\frac{\partial \xi^l}{\partial x_j} \frac{\partial u_i}{\partial \xi^l} + \frac{\partial \xi^l}{\partial x_i} \frac{\partial u_j}{\partial \xi^l} - \frac{2}{3} \delta_{ij} \frac{\partial u_l}{\partial \xi^m} \frac{\partial \xi^m}{\partial x_l} \right) \right] \end{aligned} \quad (2.13)$$

where U_j is the velocity component in the ξ^j direction, also known as the contravariant velocity component,

$$U_j = \frac{\partial \xi^j}{\partial t} + \frac{\partial \xi^j}{\partial x_k} u_k \quad (2.14)$$

τ has been replaced by t in the above equations. J is the coordinate transformation Jacobian, given by

$$\begin{aligned} \frac{1}{J} &= \frac{\partial(x^1, x^2, x^3)}{\partial(\xi^1, \xi^2, \xi^3)} = \frac{\partial x_1}{\partial \xi^1} \left(\frac{\partial x_2}{\partial \xi^2} \frac{\partial x_3}{\partial \xi^3} - \frac{\partial x_3}{\partial \xi^2} \frac{\partial x_2}{\partial \xi^3} \right) + \\ &\frac{\partial x_1}{\partial \xi^2} \left(\frac{\partial x_3}{\partial \xi^1} \frac{\partial x_2}{\partial \xi^3} - \frac{\partial x_2}{\partial \xi^1} \frac{\partial x_3}{\partial \xi^3} \right) + \frac{\partial x_1}{\partial \xi^3} \left(\frac{\partial x_2}{\partial \xi^1} \frac{\partial x_3}{\partial \xi^2} - \frac{\partial x_3}{\partial \xi^1} \frac{\partial x_2}{\partial \xi^2} \right) \end{aligned} \quad (2.15)$$

or

$$\frac{1}{J} = x_\xi (y_\eta z_\zeta - z_\eta y_\zeta) + x_\eta (x_\xi y_\zeta - y_\xi z_\zeta) + x_\zeta (y_\xi z_\eta - z_\xi y_\eta) \quad (2.16)$$

The coordinate-transformation matrices are defined as

$$\begin{aligned} \xi_x &= J (y_\eta z_\zeta - z_\eta y_\zeta), \quad \eta_x = J (z_\xi y_\zeta - y_\xi z_\zeta), \\ \xi_y &= J (z_\eta x_\zeta - x_\eta z_\zeta), \quad \eta_y = J (x_\xi z_\zeta - z_\xi x_\zeta), \\ \xi_z &= J (x_\eta y_\zeta - y_\eta x_\zeta), \quad \eta_z = J (y_\xi x_\zeta - x_\xi y_\zeta), \\ \zeta_x &= J (y_\xi z_\eta - z_\xi y_\eta), \quad \xi_t = -x_t \xi_x - y_t \xi_y - z_t \xi_z, \\ \zeta_y &= J (z_\xi x_\eta - x_\xi z_\eta), \quad \eta_t = -x_t \eta_x - y_t \eta_y - z_t \eta_z, \\ \zeta_z &= J (x_\xi y_\eta - y_\xi x_\eta), \quad \zeta_t = -x_t \zeta_x - y_t \zeta_y - z_t \zeta_z \end{aligned} \quad (2.17)$$

Unlike the density-based method, where pressure is directly expressed in terms of density and kinetic energy by the equation of state, the pressure-based method keeps the pressure gradient terms in the momentum equation for the coupling with velocity.

2.2 Discretization of Governing Equations

The discretized finite-difference forms of the governing differential equations are obtained using a finite-volume approach. First, the solution domain is divided into a finite number of discrete volumes or "cells," where all variables are stored at their

geometric centers. In the current REFLEQS code, a non-staggered grid system is adapted, and a typical control volume is shown in Figure 2-1.

Equations 2.11 to 2.13 are then integrated over all the control volumes by using the Gauss's theorem. For example, the integration of the continuity equation of 2.11 leads to

$$\frac{(\rho \text{ vol})_P - (\rho \text{ vol})_P^o}{\Delta t} + G_e - G_w + G_n - G_s + G_h - G_l = 0 \quad (2.18)$$

where vol is the volume of the cell, and the G's represent the mass flux over the control volume surfaces.

$$\begin{aligned} G_e &= \left(\frac{\Delta \xi^2 \Delta \xi^3}{J} \rho U_1 \right)_e, & G_w &= \left(\frac{\Delta \xi^2 \Delta \xi^3}{J} \rho U_1 \right)_w, \\ G_n &= \left(\frac{\Delta \xi^3 \Delta \xi^1}{J} \rho U_2 \right)_n, & G_s &= \left(\frac{\Delta \xi^3 \Delta \xi^1}{J} \rho U_2 \right)_s, \\ G_h &= \left(\frac{\Delta \xi^1 \Delta \xi^2}{J} \rho U_3 \right)_h, & G_l &= \left(\frac{\Delta \xi^1 \Delta \xi^2}{J} \rho U_3 \right)_l \end{aligned} \quad (2.19)$$

The subscripts e, w, n, s, h, and l represent the values at east, west, north, south, high, and low faces. The superscript "o" represents the previous time level. For clarity, the first-order backward Euler differencing scheme is shown. For second order accuracy in time, the fluxes of G's can be interpolated between the present time level and the previous time level "o". The detailed derivation will be omitted here.

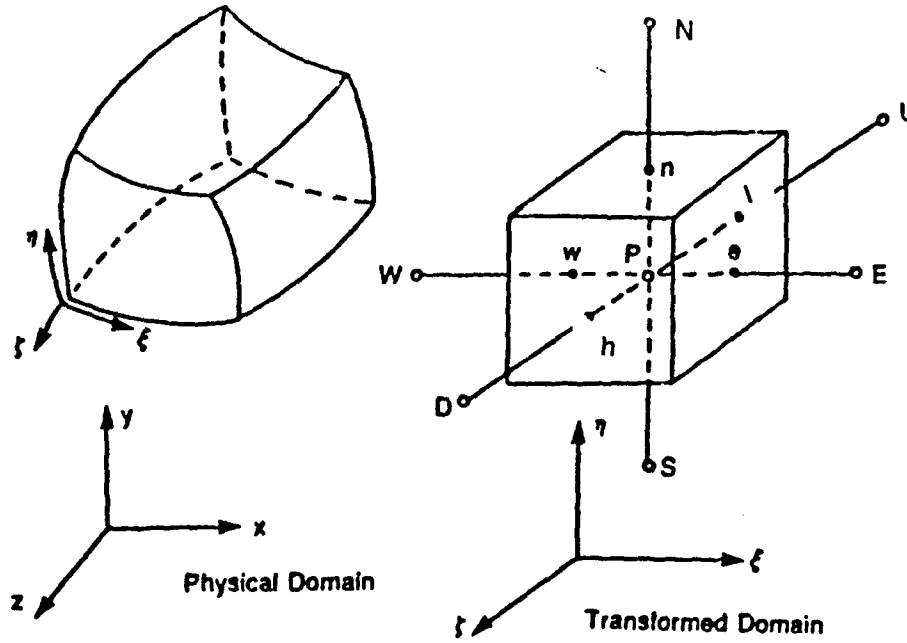


Figure 2-1. Curvilinear Coordinates and Finite-Volume Representation

Integration of momentum equation 2.12 results in

$$\begin{aligned}
 & \frac{(\rho \text{ vol } u_i)_P - (\rho \text{ vol } u_i)_P^0}{\Delta t} + \left[(Gu_i) - \frac{\mu \Delta \xi^2 \Delta \xi^3}{J} g^{1k} \frac{\partial u_i}{\partial \xi^k} \right]_w^e + \\
 & \left[(Gu_i) - \frac{\mu \Delta \xi^3 \Delta \xi^1}{J} g^{2k} \frac{\partial u_i}{\partial \xi^k} \right]_s^n + \left[(Gu_i) - \frac{\mu \Delta \xi^1 \Delta \xi^2}{J} g^{3k} \frac{\partial u_i}{\partial \xi^k} \right]_l^h = \\
 & - \left(\frac{\Delta \xi^2 \Delta \xi^3}{J} \frac{\partial \xi^1}{\partial x_i} \right)_P (p_e - p_w) - \left(\frac{\Delta \xi^3 \Delta \xi^1}{J} \frac{\partial \xi^2}{\partial x_i} \right)_P (p_n - p_s) - \left(\frac{\Delta \xi^1 \Delta \xi^2}{J} \frac{\partial \xi^3}{\partial x_i} \right)_P (p_h - p_l) + S_{u_i}
 \end{aligned} \tag{2.20}$$

where

$$g^{ik} = \frac{\partial \xi^i}{\partial x_j} \cdot \frac{\partial \xi^k}{\partial x_j} \quad (2.21)$$

and

$$\begin{aligned} S_{u_i} = & \left\{ \frac{\mu \Delta \xi^2 \Delta \xi^3}{J} \left[\left(\frac{\partial \xi^1}{\partial x_j} \frac{\partial \xi^l}{\partial x_i} \right) \frac{\partial u_j}{\partial \xi^l} - \frac{2}{3} \left(\frac{\partial \xi^1}{\partial x_j} \frac{\partial \xi^m}{\partial x_l} \right) \frac{\partial u_l}{\partial \xi^m} \delta_{ij} \right] \right\}_w^e + \\ & \left\{ \frac{\mu \Delta \xi^3 \Delta \xi^1}{J} \left[\left(\frac{\partial \xi^2}{\partial x_j} \frac{\partial \xi^l}{\partial x_i} \right) \frac{\partial u_j}{\partial \xi^l} - \frac{2}{3} \left(\frac{\partial \xi^2}{\partial x_j} \frac{\partial \xi^m}{\partial x_l} \right) \frac{\partial u_l}{\partial \xi^m} \delta_{ij} \right] \right\}_s^n + \\ & \left\{ \frac{\mu \Delta \xi^1 \Delta \xi^2}{J} \left[\left(\frac{\partial \xi^3}{\partial x_j} \frac{\partial \xi^l}{\partial x_i} \right) \frac{\partial u_j}{\partial \xi^l} - \frac{2}{3} \left(\frac{\partial \xi^3}{\partial x_j} \frac{\partial \xi^m}{\partial x_l} \right) \frac{\partial u_l}{\partial \xi^m} \delta_{ij} \right] \right\}_l^h \end{aligned} \quad (2.22)$$

Similarly, the energy equation can be written as:

$$\begin{aligned} & \frac{(\rho \text{ vol } H)_p - (\rho \text{ vol } H)_p^0}{\Delta t} + \left[(GH) - \frac{\Gamma \Delta \xi^2 \Delta \xi^3}{J c_p} g^{1k} \frac{\partial H}{\partial \xi^k} \right]_w^e + \\ & \left[(GH) - \frac{\Gamma \Delta \xi^3 \Delta \xi^1}{J c_p} g^{2k} \frac{\partial H}{\partial \xi^k} \right]_s^n + \left[(GH) - \frac{\Gamma \Delta \xi^1 \Delta \xi^2}{J c_p} g^{3k} \frac{\partial H}{\partial \xi^k} \right]_l^h \\ & = S_H \end{aligned} \quad (2.23)$$

In the above equation, the heat diffusion terms have been replaced by the diffusion of total enthalpy. S_H is:

$$\begin{aligned}
S_H = & \left[\frac{\Gamma \Delta \xi^2 \Delta \xi^3}{J} g^{1k} \left(\frac{\partial T}{\partial \xi^k} - \frac{1}{c_p} \frac{\partial H}{\partial \xi^k} \right) \right]_w^e + \left[\frac{\Gamma \xi^3 \Delta \xi^1}{J} g^{2k} \left(\frac{\partial T}{\partial \xi^k} - \frac{1}{c_p} \frac{\partial H}{\partial \xi^k} \right) \right]_s^n \\
& + \left[\frac{\Gamma \Delta \xi^1 \Delta \xi^2}{J} g^{3k} \left(\frac{\partial T}{\partial \xi^k} - \frac{1}{c_p} \frac{\partial H}{\partial \xi^k} \right) \right]_l^h \\
& + \left\{ \frac{\mu \Delta \xi^2 \Delta \xi^3}{J} u_i \left[\left(\frac{\partial \xi^1}{\partial x_j} \frac{\partial \xi^l}{\partial x_i} \right) \frac{\partial u_j}{\partial \xi^l} - \frac{2}{3} \left(\frac{\partial \xi^1}{\partial x_j} \frac{\partial \xi^m}{\partial x_i} \right) \frac{\partial u_l}{\partial \xi^m} \delta_{ij} \right] \right\}_w^e \\
& + \left\{ \frac{\mu \Delta \xi^3 \Delta \xi^1}{J} u_i \left[\left(\frac{\partial \xi^2}{\partial x_j} \frac{\partial \xi^l}{\partial x_i} \right) \frac{\partial u_j}{\partial \xi^l} - \frac{2}{3} \left(\frac{\partial \xi^2}{\partial x_j} \frac{\partial \xi^m}{\partial x_i} \right) \frac{\partial u_l}{\partial \xi^m} \delta_{ij} \right] \right\}_s^n \\
& + \left\{ \frac{\mu \Delta \xi^3 \Delta \xi^2}{J} u_i \left[\left(\frac{\partial \xi^3}{\partial x_j} \frac{\partial \xi^l}{\partial x_i} \right) \frac{\partial u_j}{\partial \xi^l} - \frac{2}{3} \left(\frac{\partial \xi^3}{\partial x_j} \frac{\partial \xi^m}{\partial x_i} \right) \frac{\partial u_l}{\partial \xi^m} \delta_{ij} \right] \right\}_l^h
\end{aligned} \tag{2.24}$$

As seen from above, the momentum equation and the energy equation are in the same form. The key issue is to approximate convective terms and diffusion terms from cell faces (e, w, n, s, h and l) to cell centers (P, E, W, N, S, H , and L). We will take the east face as an example. The convective term C can be generally written as:

$$C_e = (G\phi)_e; \quad \phi = u_i, H \tag{2.25}$$

The following approximation can be made:

$$C_e = \beta C_e^{UP} + (1 - \beta) C_e^{CN} \tag{2.26}$$

where superscript UP stands for upwind differencing and CN for central differencing.

$$C_e^{UP} = \frac{G_e}{2}(\phi_E + \phi_P) - \frac{|G_e|}{2}(\phi_E - \phi_P) \quad (2.27a)$$

$$C_e^{CN} = \frac{G_e}{2}(\phi_E - \phi_P) \quad (2.27b)$$

As a result Equation (2.26) becomes,

$$C_e = \frac{G_e}{2}(\phi_E + \phi_P) - \frac{\beta}{2}|G_e|(\phi_E - \phi_P) \quad (2.28)$$

As for the diffusion term, D_e :

$$\begin{aligned} D_e &= \left(\frac{\Gamma \Delta \xi^2 \Delta \xi^3}{J} g^{1k} \frac{\partial \phi}{\partial \xi^k} \right)_e \\ &= \frac{\Gamma \Delta \xi^2 \Delta \xi^3}{J} \left(g^{11} \frac{\partial \phi}{\partial \xi^1} + g^{12} \frac{\partial \phi}{\partial \xi^2} + g^{13} \frac{\partial \phi}{\partial \xi^3} \right)_e \\ &= \frac{\Gamma \Delta \xi^2 \Delta \xi^3}{J} \left(g^{11} \frac{\phi_E - \phi_P}{\Delta \xi^1} + g^{12} \frac{\phi_{ne} - \phi_{se}}{\Delta \xi^2} + g^{13} \frac{\phi_{he} - \phi_{le}}{\Delta \xi^3} \right) \end{aligned} \quad (2.29)$$

A further approximation is made as to express ϕ_{ne} , ϕ_{se} , ϕ_{he} , and ϕ_{le} in terms of the values at cell center:

$$\begin{aligned} \phi_{ne} &= \frac{1}{4}(\phi_N + \phi_E + \phi_P + \phi_{NE}) \\ \phi_{se} &= \frac{1}{4}(\phi_S + \phi_E + \phi_P + \phi_{SE}) \\ \phi_{he} &= \frac{1}{4}(\phi_H + \phi_E + \phi_P + \phi_{HE}) \\ \phi_{le} &= \frac{1}{4}(\phi_L + \phi_E + \phi_P + \phi_{LE}) \end{aligned} \quad (2.30)$$

The same procedure applies to the convective and diffusive terms at west, north, south, high, and low faces. With these representations, a finite-difference analog of the governing equations can be expressed as:

$$\begin{aligned}
A_P \phi_P = & A_E \phi_E + A_W \phi_W + A_N \phi_N + A_S \phi_S + A_H \phi_H + A_L \phi_L + \\
& A_{SW} \phi_{SW} + A_{NW} \phi_{NW} + A_{SE} \phi_{SE} + A_{NE} \phi_{NE} + \\
& A_{WL} \phi_{WL} + A_{EL} \phi_{EL} + A_{WH} \phi_{WH} + A_{EH} \phi_{EH} + \\
& A_{LS} \phi_{LS} + A_{HS} \phi_{HS} + A_{LN} \phi_{LN} + A_{HN} \phi_{HN} + S_\phi
\end{aligned} \tag{2.31}$$

or simply

$$A_P \phi_P = \sum_{nb} A_{nb} \phi_{nb} + \sum_{cnb} A_{cnb} \phi_{cnb} + S_\phi \tag{2.32}$$

where

$$\phi = u_r H$$

$$nb = E, W, N, S, H, L$$

$$cnb = SW, NW, SE, NE, WL, EL, WH, EH, LS, HS, LN, HN$$

cnb means cross-neighbor. A_{cnb} vanishes when the grids are orthogonal, and it is small compared to the other part if the grid non-orthogonality is not severe.

2.3 Pressure-Velocity Coupling

The discretized finite difference equation (2.32) does not apply to continuity equation. Unlike the density-based method where density is treated as a transport variable in the continuity equation, the pressure-based method takes pressure as the dependent variable in the continuity equation. It requires a proper coupling between velocity and pressure. Presently, the coupling of pressure and velocity is achieved via the well known SIMPLE algorithm⁷⁸ and its variants SIMPLER⁷⁹ and PISO.⁸⁰

As seen from Equation 2.18, the contravariant velocity component is needed at a control volume face. For example, at the east face,

$$(U_1)_e = \left(\frac{\partial \xi^1}{\partial t} \right)_e + \left(\frac{\partial \xi^1}{\partial x_i} \right)_e \cdot (u_i)_e \quad (2.33)$$

Since only the values U_i at cell center P and E are known, an interpolation is required. The first choice may be the linear interpolation. This, however, will give rise oscillations in the final resolution, as explained by Patankar⁷⁸. Early practice was to use a staggered grid arrangement to avoid any possible oscillation.

In the staggered grid arrangement, velocity components at cell faces are solved from momentum equations and hence no interpolation for the velocity components is necessary. In the current REFLEQS code, a non-staggered grid system is used, and to avoid oscillations, a special interpolation practice is employed, as suggested by Rhie and Chow⁸¹, and by Peric⁸².

The idea is based on the supposition that if the velocity values at the cell faces were obtained by solving the momentum equations at the cell faces, these momentum equations would contain a pressure gradient which could be evaluated as the difference between neighboring pressure locations. To illustrate this procedure, we write the momentum equation as:

$$(u_i)_P = \left[\frac{\sum A_{nb} u_{nb} + \sum A_{cnb} u_{cnb} + S_{u_i}}{A_P} \right]_P - \left[D_{ij} \frac{\partial p}{\partial \xi^j} \right]_P \quad (2.34)$$

where

$$D_{ij} = \left[\frac{\Delta \xi^1 \Delta \xi^2 \Delta \xi^3}{A_P J} \frac{\partial \xi^j}{\partial x_i} \right] \quad (2.35)$$

In comparison to Equation 2.32, the pressure gradient terms have been taken out of S_p and shown explicitly. To evaluate $(u_i)_e$ (at east face) the terms on the right-hand side of Equation 2.34 are selectively interpolated for "e" location. Thus,

$$(u_i)_e = \left[\frac{\sum A_{nb} \phi_{nb} + \sum A_{cnb} \phi_{cnb} + S_{u_i}}{A_p} \right]_e - \left[\bar{D}_{ij} \frac{\partial p}{\partial \xi^j} \right]_e \quad (2.36)$$

where the overbar denotes linear interpolation. The cell face velocities are thus made dependent on the pressure at two neighboring nodes, as is the case in the true staggered arrangement. For uniform grid, with the use of Equation 2.34, we can write the above expression as:

$$(u_i)_e = \frac{1}{2} [(u_i)_E + (u_i)_P] + \frac{1}{2} \left\{ \left(D_{ij} \frac{\partial p}{\partial \xi^j} \right)_E - [(D_{ij})_E + (D_{ij})_P] \left(\frac{\partial p}{\partial \xi^j} \right)_e + \left(D_{ij} \frac{\partial p}{\partial \xi^j} \right)_P \right\} \quad (2.37)$$

It is equivalent to linear interpolation with added third order pressure damping. This pressure damping term is necessary for incompressible flows, and it may cause accuracy problems for source dominant (such as rotational and gravitational) flows, as well as compressible flows. Therefore, a coefficient is multiplied to this term:

$$(u_i)_e = \frac{1}{2} [(u_i)_E + (u_i)_P] + \frac{\alpha_d}{2} \left\{ \left(D_{ij} \frac{\partial p}{\partial \xi^j} \right)_E - [(D_{ij})_E + (D_{ij})_P] \left(\frac{\partial p}{\partial \xi^j} \right)_e + \left(D_{ij} \frac{\partial p}{\partial \xi^j} \right)_P \right\} \quad (2.38)$$

For incompressible flow $\alpha_d = 1.0$, and for compressible flows $\alpha_d = 0.1$. With $(u_i)_e$ calculated as the above, the contravariant component can be found from Equation (2.33).

From now on the SIMPLE strategy can be used in its standard form, developed for the staggered arrangement grid system. The mass imbalance resulting from continuity equation 2.18 is:

$$\frac{(\rho \text{ vol})_p - (\rho \text{ vol})_p^0}{\Delta t} + G_e^* - G_w^* + G_n^* - G_s^* + G_h^* - G_l^* = S_m \quad (2.39)$$

where superscript * denotes values employed in and resulting from the momentum equations.

To enforce the continuity equation, a mass flux correction G' is introduced, which in turn relates velocity correction u_i' , which is further related to the pressure correction p' by:

$$u_i' = -D_{ij} \frac{\partial p'}{\partial \xi^j} \quad (2.40)$$

The continuity equation then reads

$$\frac{(\rho \text{ vol})'}{\Delta t} + G_e' - G_w' + G_n' - G_s' + G_h' - G_l' + S_m = 0 \quad (2.41)$$

For G_e' we have

$$G_e' = \frac{\Delta \xi^2 \Delta \xi^3}{I} (\rho' U_1 + \rho U_1')_e \quad (2.42)$$

From equation of state and Equation 2.33, we have

$$\rho_e' = \frac{\partial \rho}{\partial p} p_e' \quad (2.43)$$

and

$$(U_1')_e = \left(\frac{\partial \xi^1}{\partial x_i} \right)_e (u_i')_e = \left(\frac{\partial \xi^1}{\partial x_i} \right)_e \bar{D}_{ij} \frac{\partial p'}{\partial \xi^j} \quad (2.44)$$

This leads to

$$\begin{aligned} & \left[\frac{\partial \rho}{\partial p} \text{vol } p' \right]_P + \left[\frac{\Delta \xi^2 \Delta \xi^3}{J} \left(\frac{\partial \rho}{\partial p} U_1 p' - \rho \frac{\partial \xi^1}{\partial x_i} \bar{D}_{ij} \frac{\partial p'}{\partial \xi^j} \right) \right]_w^e + \\ & \left[\frac{\Delta \xi^3 \Delta \xi^1}{J} \left(\frac{\partial \rho}{\partial p} U_2 p' - \rho \frac{\partial \xi^2}{\partial x_i} \bar{D}_{ij} \frac{\partial p'}{\partial \xi^j} \right) \right]_s^n + \left[\frac{\Delta \xi^1 \Delta \xi^2}{J} \left(\frac{\partial \rho}{\partial p} U_3 p' - \rho \frac{\partial \xi^3}{\partial x_i} \bar{D}_{ij} \frac{\partial p'}{\partial \xi^j} \right) \right]_l^h = -S_m \end{aligned} \quad (2.45)$$

Equation 2.45 is the same form as Equation 2.20, and hence it leads to an equation for the pressure correction which has the same form as Equation 2.32.

For the solution domain as a whole this results in a system of N equations with N unknowns, where N is the number of control volumes. Several efficient iterative solvers have been employed to solve the system equations, for example, modified strongly implicit procedure (SIP) of Stone,⁸³ based on an incomplete LU factorization of the coefficient matrix.

2.4 Solution Algorithm

Based on the proceeding discretization, the solution algorithm for the transient flows in body-fitted moving coordinates can be summarized as follows:

1. Specify initial grid and values of dependent variables (initial conditions);
2. Determine grid velocity ξ_i, η_i, ζ_i from the new grid position after the time has advanced by Δt ;
3. Calculate the coefficients of the momentum equation and solve to obtain a new velocity field;
4. Calculate new values of mass fluxes through the cell faces using Equations 2.33 and 2.19, and determine the mass imbalance using Equation 2.39;

5. Calculate the coefficients of the pressure-correction equation and solve to obtain the pressure-correction field;
6. Correct the mass fluxes, nodal velocity components and pressure by the calculated pressure;
7. Calculate the coefficients of other scalar equations which may be coupled with the momentum equation (*e.g.* total enthalpy, turbulent kinetic energy and its dissipation rate,*etc.*) and update the fluid properties (density, viscosity) if necessary;
8. Return to step 3 and repeat until the sum of the absolute residuals in the momentum and continuity equations has failed by a specified order of magnitude; and
- 9 Advance the time by another increment Δt and return to step 2; repeat until the prescribed number of time steps is completed or the prescribed time has been reached.

The number of iterations per time step (steps 3-7) depends on the size of the time increment Δt ; for smaller Δt fewer iterations are needed to reach the solution at the new time level.

2.5 Turbulence Modeling

When the Reynolds number is high, the flow around an airfoil or wing is turbulent. Due to the finite resolution of computational grids, a computer simulation will not be able to capture the small scale vortices. This requires the modeling of the turbulence effect. In the current REFLEQS code, there are four turbulence models available: Baldwin-Lomax model; Standard $k-\epsilon$; Multiple Scale $k-\epsilon$, and Low Reynolds number $k-\epsilon$, proposed by K.Y. Chien.

Previous studies on the effect of turbulence models on dynamic stall have been conducted by Wu *et al*⁸⁴. They compared, for a variety of flows, three eddy viscosity models: the algebraic Baldwin-Lomax model, the one equation Johnson-King model, and the two equation Gorski k- ϵ model. They found that the Baldwin-Lomax model⁸⁵ is as reliable and accurate as any other model for massively separated flows, but that all models are to date inaccurate in the same regime. Furthermore, the Baldwin-Lomax model is simple to employ and cost efficient. In light of Wu *et al.*'s conclusions⁸⁴, we will simulate the effect of turbulence by the Baldwin-Lomax two layer eddy viscosity model⁸⁵.

2.6 Grid Generation

The time-dependent coordinate transformation (*i.e.* moving grid) required for the present flow simulation was implemented using a "rigid" grid attached to the airfoil or the wing. This approach eliminates the need for multiple grid generation, and only one grid is required. In the present study, an O-H grid topology is employed, and a typical three-dimensional grid around a wing is shown in Figure 2-2. First an O-grid is generated using algebraic method around an airfoil. An elliptic solver based on Thompson *et al.*'s methods⁸⁶ is then applied to improve grid orthogonality, if required. An algebraic method is then used to generate three-dimensional grid from 2-D O-grid.

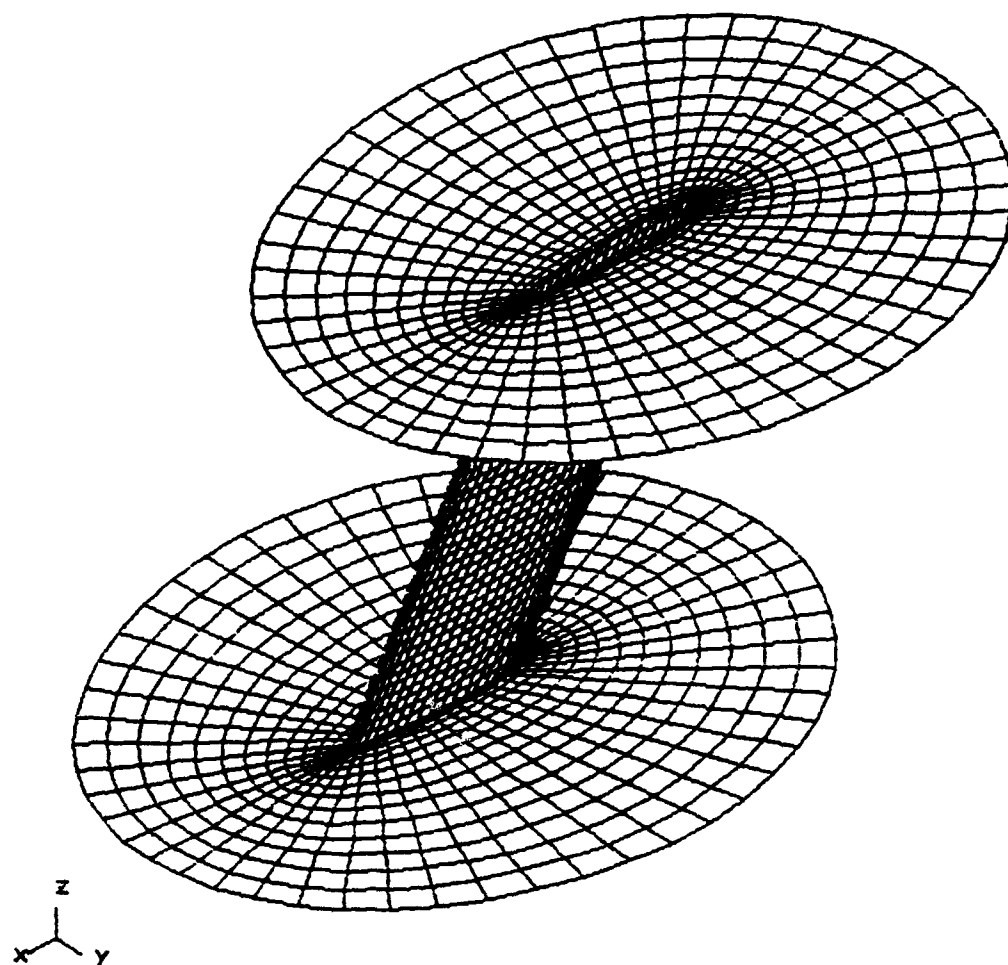


Figure 2-2. An O-H Grid Around a Rectangular Wing
with NACA0012 Cross-Section

2.7 Boundary Conditions

The present procedure requires boundary conditions to be set on: a) solid boundary; b) symmetric boundary; c) far field boundary; and d) periodic boundary.

2.7.1 Solid Boundary

At the solid boundary the "no-slip" condition requires the fluid velocity to be the same as that of the solid, and the motion of the solid is a known function of time. Also adiabatic flow conditions have been applied on the solid surface. The pressure at the solid surface may be evaluated in various ways, such as solving the normal momentum equation at the surface. In the present study, a two point extrapolation was used. For example, if the east face is a solid boundary and uniform grid is used:

$$p_e = \frac{3}{2} p_P - \frac{1}{2} p_W \quad (2.46)$$

The above form was found to give virtually the same results as those obtained by solving the normal momentum equations at the solid surface.

2.7.2 Symmetric Boundary

This boundary applies to a three-dimensional wing root where the viscous effect is neglected. It also applies to the wall for inviscid calculation. At this boundary, the normal contravariant component is set to zero, and other components are extrapolated from the interior. The pressure is found by Equation 2.46.

2.7.3 Far Field Boundary

At the far field boundaries, except in the downstream boundary, the flowfield is assumed to be prescribed and undisturbed. At the downstream boundary, the velocity field and total enthalpy, as well as pressure, are extrapolated from the interior.

2.7.4 Periodic Boundary

On the O-grid cut, spatial periodicity is imposed. This leads to a system of periodic matrix equations.

3. PROPOSED NEW METHODOLOGIES AND IMPROVEMENTS

The pressure-based numerical solution procedure for the dynamic stall around an airfoil or a wing has been described in the previous section. In comparison, most of the previous numerical studies relied on the density based method. The typical representatives of density-based codes are Pulliam-Steger's ARC2D and ARC3D flow solver⁸⁷⁻⁸⁹. These codes solve either the Euler or the simplified Reynolds-averaged Navier-Stokes equations with the standard thin-layer approximation. Two numerical algorithms are generally supported by the ARC 3D flow solver, including ADI algorithm that solves block-tri-diagonal matrices along each coordinate direction due to Beam and Warming²⁶ and a diagonalized ADI algorithm that solves scalar pentadiagonal matrices along each coordinate direction due to Pulliam and Chaussee⁸⁹.

In comparison to the density-based method, which is generally limited to compressible flows, the pressure-based method can solve all speed flows ranging from incompressible to high Mach number compressible flows. Instead of solving systems of equations, the pressure-based method solves one variable at a time, in a segregated approach, which requires less computer storage. Segregated solution approach, however, may lead to numerical difficulties when strong coupling among all of the variables exists (*e.g.* high Reynolds number flows). The presently proposed Newton's iteration technique aims to resolves this problem.

High resolution TVD schemes have been well proven for density-based method, and are still to be explored for pressure-based method. This section describes three new methodologies:

1. High-Order TVD Schemes, improving the accuracy;
2. Newton's Iteration Technique, accelerating numerical convergence rate;
and
3. Hyperbolic Pressure Correction, for pressure solver efficiency.

3.1 High-Order TVD Schemes

Total Variation Diminishing (TVD) concept was first introduced by Harten⁶⁴. An excellent consolidation of various TVD methods has been given by Yee⁹⁰. These high order TVD schemes have shown excellent accuracy in solving Euler equations for compressible inviscid flows. They have also been applied in a straightforward manner for the evaluation of the convective terms of the Navier-Stokes equations within the framework of density-based algorithms.⁹¹⁻⁹⁵ The Research Group at CFDRC has initiated a study on high order TVD schemes in the pressure-based algorithm,⁷² and the results obtained for quasi-one-dimensional nozzle (Figure 3-1), 1D Riemann problem (Figure 3-2), and resonant pipe problem (Figure 1-2) are very promising.

The fundamental success of the TVD schemes lies in the accurate, conservative and consistent evaluation of the convective flux (Equation 2.26). The key issue is how to evaluate the "damping" parameter β of Equation (2.26), so that the solution is high-order accurate and oscillation free. In TVD schemes, the damping β is adaptive based on the profile of the local transport variable. By manipulating Chakravarthy and Osher's TVD scheme⁶⁵, we can find the east face flux as:

$$C_e^{TVD} = \beta C_e^{UP} + (1-\beta) C_e^{CN} \quad (3.1)$$

where

$$\beta = \frac{3-\phi}{4} \text{minimod} \left(\frac{r}{\omega}, 1 \right) + \frac{1+\phi}{4} \text{minimod} (1, \omega r) \quad (3.2)$$

with ω as a compressibility parameter,

$$\omega = \frac{3 - \phi}{1 - \phi} \quad (3.3)$$

and r is the flux difference ratio:

$$r = \frac{(C^{CN} - C^{UP})_e}{(C^{CN} - C^{UP})_{e-\sigma}}, \text{ and } \sigma = \text{sign}(U_e) \quad (3.4)$$

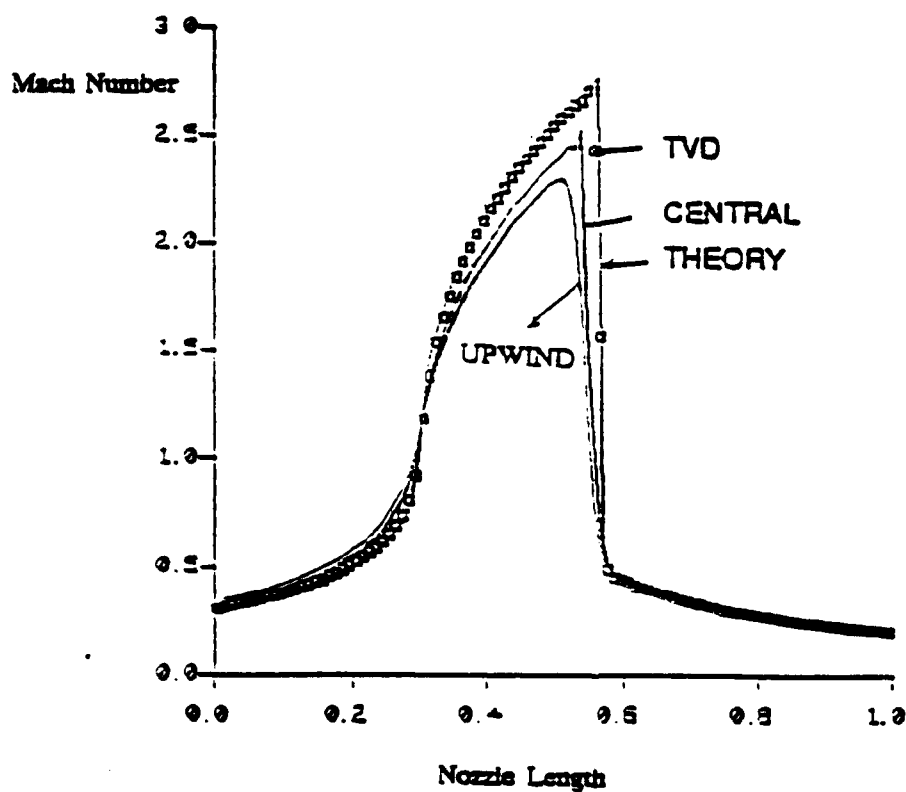


Figure 3-1. Mach Number Calculated Along a Converging-Diverging Nozzle Length by Upwind, Central, and TVD Schemes With Pressure-Based Method

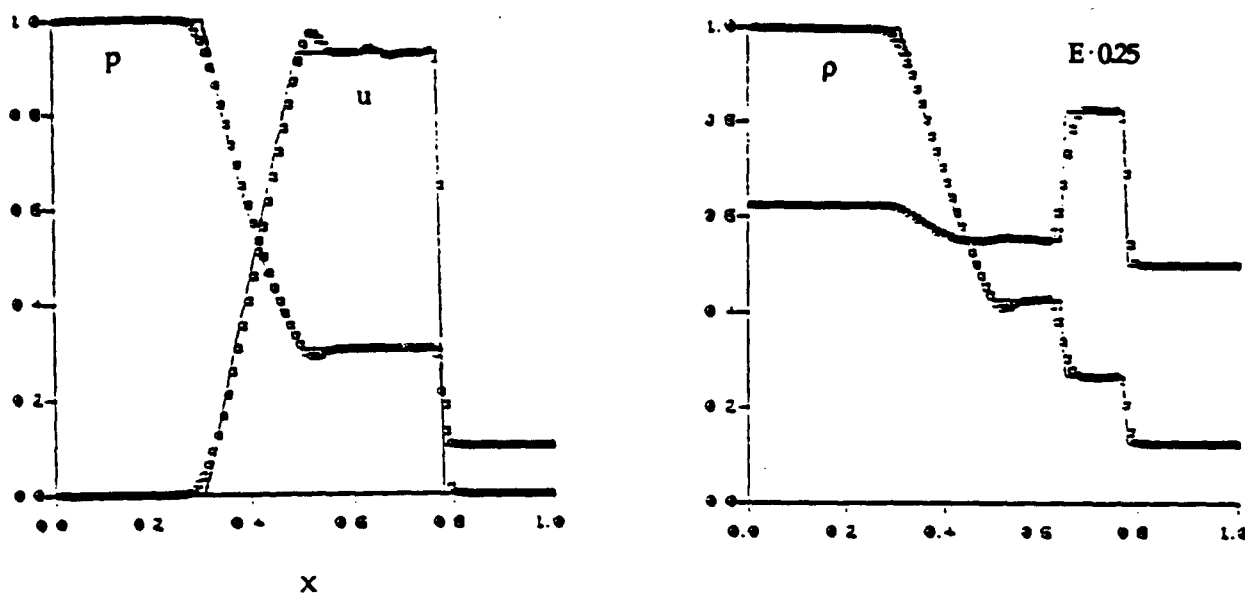


Figure 3-2. 1-D Shock Tube Problem by TVD Scheme With Pressure-Based Method

Based on the value of ϕ , one can recover different schemes

$$\begin{aligned}
 \phi &= 1/3 && \text{Third-order scheme} \\
 &= -1 && \text{Fully-upwind} \\
 &= 0 && \text{Fromm's} \\
 &= 1/2 && \text{Low truncation error second-order} \\
 &= 1 && \text{Central} \\
 &= -1/3 && \text{No Name}
 \end{aligned} \tag{3.5}$$

The minimod function is defined as:

$$\text{minimod}(a,b) = \text{sign}(a) \max \{0, \min [|a|, \text{sign}(a) \cdot b]\} \tag{3.6}$$

The mathematical meaning of this limiting procedure is to pick up the smallest value between a and b, if both have the same sign, or to pick up zero if both have different signs.

3.2 Newton's Iteration Technique

It is well known that Newton's iterative method gives a superior convergence rate. However, Newton's method is frequently used to solve small systems of nonlinear algebraic equations, and it is less often used for the large systems of nonlinear equations, such as those generated by the discretization of Navier-Stokes equations for fluid dynamics. This is because Newton's method requires EXACT evaluation and inversion of the Jacobian matrix, which is almost impractical due to limited computer memory and speed. Many of the approaches for solving Navier-Stokes equations are only an approximation to the pure Newton's method. For example the popular Alternating Direction Implicit (ADI) method in density-based algorithms uses an approximate factorization of the Jacobian matrix to reduce numerical operations as well as memory storage requirements. In addition, it is quite common to make approximations for elements of the Jacobian corresponding to algebraically complicated terms or terms that increase the bandwidth of the factorized Jacobian matrix, *e.g.* terms that arise from the turbulence model.

The proposed Newton's method requires less storage while making no approximations to the Jacobian matrix. To illustrate this method, we use Equation 2.32:

$$A_p \phi_p - \sum A_{nb} \phi_{nb} - \sum A_{cnb} \phi_{cnb} = S_\phi \quad (3.7)$$

where ϕ can be velocity, total enthalpy or pressure correction. The nonlinearity of the above equation comes from the link coefficient A's, due to

- a. velocity quadratic convective features;
- b. variable density in convection term; and
- c. nonlinear turbulent diffusion.

Let subscript "o" denote the last time step value. The standard linearization in the pressure-based method is:

$$A_p^o \phi_p' - \sum A_{nb}^o \phi_{nb}' - \sum A_{cnb}^o \phi_{cnb}' = S_\phi - A_p^o \phi_p^o + \sum A_{nb}^o \phi_{nb}^o + \sum A_{cnb}^o \phi_{cnb}^o \quad (3.8)$$

$$\phi' = \phi - \phi^o$$

The convergence rate of the above method is first-order in a single time step. We propose a Newton's iteration method as:

$$A_p^o \phi_p' - \sum A_{nb}^o \phi_{nb}' - \sum A_{cnb}^o \phi_{cnb}' = S_\phi - A_p^o \phi_p^o + \sum A_{nb}^o \phi_{nb}^o + \sum A_{cnb}^o \phi_{cnb}^o \quad (3.9)$$

$$- A_p^* \phi_p^o + \sum A_{nb}^* \phi_{nb}^o + \sum A_{cnb}^* \phi_{cnb}^o$$

where "*" means the last iteration value. The iteration loop is imposed for velocity and pressure equations, so that it will not only accelerate the convergence, but will also strongly couple all the variables. The method is efficient for steady-state as well as for transient problems.

For the turbulence model, e.g. k-ε model, the Newton linearization (Equation 3.9) also applies to the k and ε equations. This will couple the whole system equation and will result in fast convergence.

3.3 Hyperbolic Pressure Correction

It has been recognized that the pressure correction equation (p' equation) in the pressure-based method has difficulties to converge, specially for convection

dominated, high Reynolds number, incompressible and compressible flows. Even though various solvers, such as block correction, conjugate gradient, coupled whole field solver, multi-grid method, ... have been tested, success is still limited. Our experience indicates that the residual error of momentum equations can be reduced to machine round-off in just a few iteration sweeps of linear equation solver. However, the iterative convergence rate of pressure correction equation is much slower than that of momentum equations. It is particularly difficult to converge the p' -equation for fine grids with large cell aspect ratios and for high Reynolds number flows. We believe that the difference between momentum equations and pressure correction equation in the finite difference form lies at link coefficients (or coefficient matrix). For the momentum equation, when convection is important, the link coefficients are hyperbolic. In the sense, for one-dimensional equation if velocity is positive, the simple upwind scheme gives:

$$A_E = D_e, A_W = C_w + D_w \quad (3.10)$$

where

$$D = \text{diffusion flux}, C = \text{convective flux}$$

Whereas for the pressure correction equation, the link coefficients are always elliptic regardless the importance of convection. By being elliptic, it means that

$$A_E = D_e, A_W = D_w \quad (3.11)$$

In a multi-dimensional iterative solver, when the link coefficients are hyperbolic, the residual (or signal) can propagate from one end to another end in one iteration sweep. Whereas for elliptic coefficients, the propagation of the residual is by "diffusion," which is much slower, and needs a large number of iteration sweeps. The "elliptic" nature of pressure correction equation comes from the general assumption: velocity variation is proportional to pressure gradient:

$$u' \sim \nabla p' \quad (3.12)$$

This relation is Darcy's law, and it holds for very viscous flow. Actually, by using this relation, one can obtain the lubrication equation (Reynolds Equation) or the equation for porous medium. On the other hand, for inviscid flow, Bernoulli equation says:

$$\frac{1}{2} \rho u^2 + p = \text{const} \quad (3.13)$$

or

$$u' \sim p' \quad (3.14)$$

if we substitute this relation into continuity equation for incompressible flow, we have:

$$\nabla u' = -\nabla u^* \quad (3.15)$$

which is hyperbolic for pressure correction. However, if we substitute Equation 3.12 into Equation 3.15 it becomes an elliptic equation. Here we propose an innovative relation for pressure-velocity relation of the form:

$$u' \sim ap' + b\nabla p' \quad (3.16)$$

a, in the above equation, is a coefficient representing hyperbolic contribution, and, b, is that representing elliptic contribution. To determine the constants a and b, let us consider one-dimensional inviscid flow of the form:

$$\frac{\partial u}{\partial t} + \frac{\partial(u^2)}{\partial x} = -\frac{\nabla p}{\rho} \quad (3.17)$$

After discretization, we have:

$$s_p u_i + A_{nb} \nabla u_i = -\frac{\nabla p}{\rho} p_i + s_p u_i^o \quad (3.18)$$

where

$$s_p = \frac{vol}{\Delta t}; \quad \nabla u_i = u_i - u_{nb} \quad (3.19)$$

The incremental form of the above equation is:

$$s_p u_i' + A_{nb} \nabla u_{nb}' = - \frac{vol}{\rho} \nabla p_i' \quad (3.20)$$

From the above equation, we expect the following asymptotic expression:

$$\text{when } s_p \rightarrow 0, \quad u_i' \sim - \frac{vol}{\rho A_{nb}} p_i' \quad (3.21)$$

$$\text{when } A_{nb} \rightarrow 0, \quad u_i' \sim - \frac{vol s_p}{\rho(s_p^2 + A_{nb}^2)} \nabla p_i'$$

one of the approximations for a and b leads to:

$$u_i' = - \frac{vol A_{nb}}{\rho(s_p^2 + A_{nb}^2)} p_i' - \frac{vol s_p}{\rho(s_p^2 + A_{nb}^2)} \nabla p_i' \quad (3.22)$$

Now the pressure correction equation should contain both hyperbolic and elliptic coefficients. One should be able to reduce the residual error of the pressure correction equation easily by standard solver, without using multi-grid or block correction.

4. TWO-DIMENSIONAL STATIC AND DYNAMIC STALLS

The Navier-Stokes solver, and its improvements, described in the previous sections has been applied to a number of test studies, for the purpose of validation and studying the physics of unsteady separation flows. In all cases, the computed results have been compared with available numerical and experimental data. This section considers the following test problems:

1. Steady, inviscid transonic and supersonic flows past a NACA 0012 airfoil;
2. Steady viscous transonic flow over a NACA 0012 and an ARE 2822 airfoil;
3. NACA 0015 airfoil undergoing constant rate pitching motions;
4. NACA 0012 airfoil undergoing oscillatory pitching motions; and
5. Parametric effect on dynamic stall on the airfoils.

Each of the above cases will be described and the results will be discussed in the following sub-sections.

4.1 Steady, Inviscid Transonic and Supersonic Flows Past a NACA 0012 Airfoil

The following calculations were performed for the NACA 0012 airfoil.

- a. $M_\infty = 1.2$, $\alpha = 7.0^\circ$
- b. $M_\infty = 1.8$, $\alpha = 7.0^\circ$
- c. $M_\infty = 0.8$, $\alpha = 1.25^\circ$

These cases have been chosen because of the existence of accurate numerical data, especially from density-based TVD code, available for detailed comparison. These cases are also used for proving the superiority of proposed TVD methodology and Newton's iteration technique.

A 100 x 50 O-grid is used. Figure 4-1 shows the grid near the airfoil surface. The outer boundary is placed at 12c distance (c is the chord length).

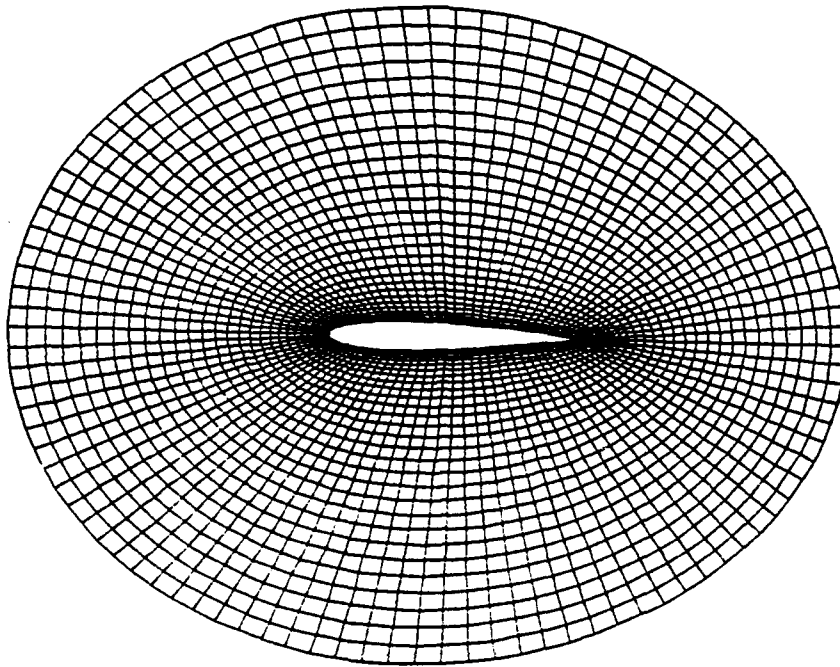
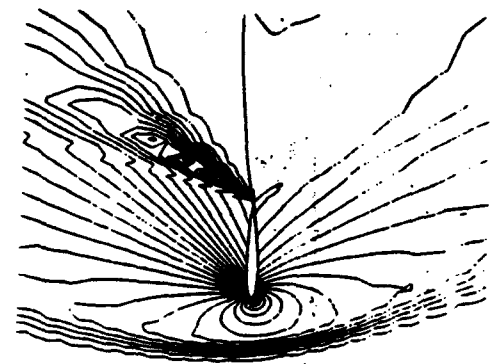
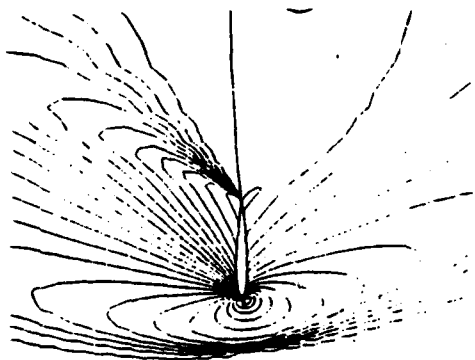
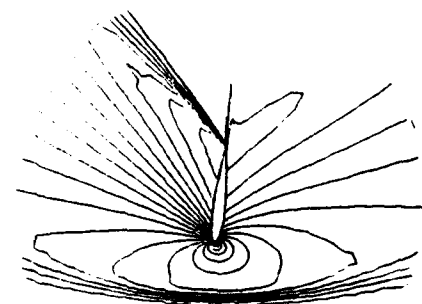


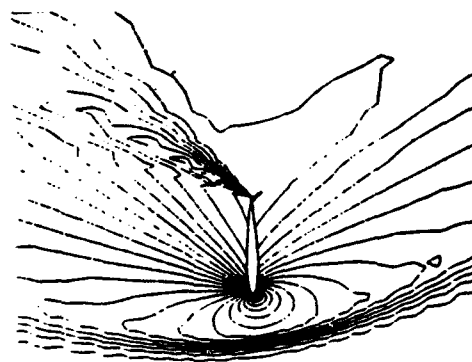
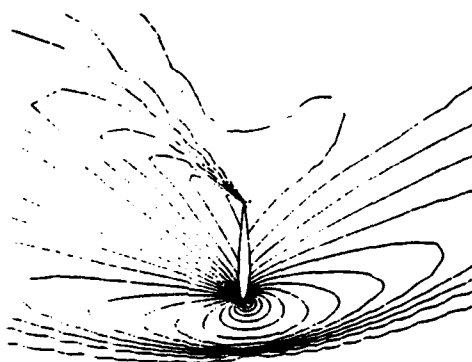
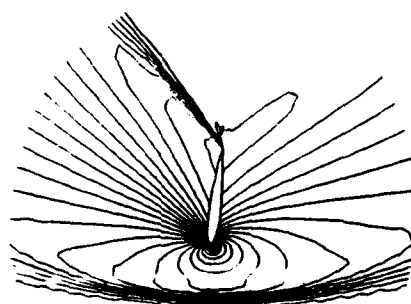
Figure 4-1. Local View of a 100 x 50 O-Grid Around a NACA 0012
Airfoil for Inviscid Computations

Figures 4-2 and 4-3 show the Mach number and pressure contours around the NACA 0012 at $\alpha = 7.0^\circ$, $M_\infty = 1.2$, and $M_\infty = 1.8$ obtained with the present third-order TVD scheme. For comparison purposes, those from Yee's density-based TVD,⁹⁰ and the widely distributed computer code ARC2D, version 150⁹⁶ are also displayed. Their results are obtained using a 163 x 49 C-grid. It is seen that the present TVD scheme gives a well-ordered flow structure and captures the shocks with a good resolution. It is very competitive with the density-based TVD scheme, and it actually performs better at the trailing edge of the airfoil. The ARC2D code, on the

Mach
Contours



Pressure
Contours



Pressure-Based TVD
Present Prediction

Density-Based TVD
H.C. Yee's Prediction
(NASA TM-101088, 1989)

ARC2D
Pulliam and Steger
(AIAA-85-0360, 1985)

Figure 4-2. Comparison of the Present Pressure-Based TVD, Yee's Density-Based TVD and ARC2D for Supersonic Flow Over a NACA0012 Airfoil at $M_\infty = 1.2$ and $\alpha = 7.0^\circ$

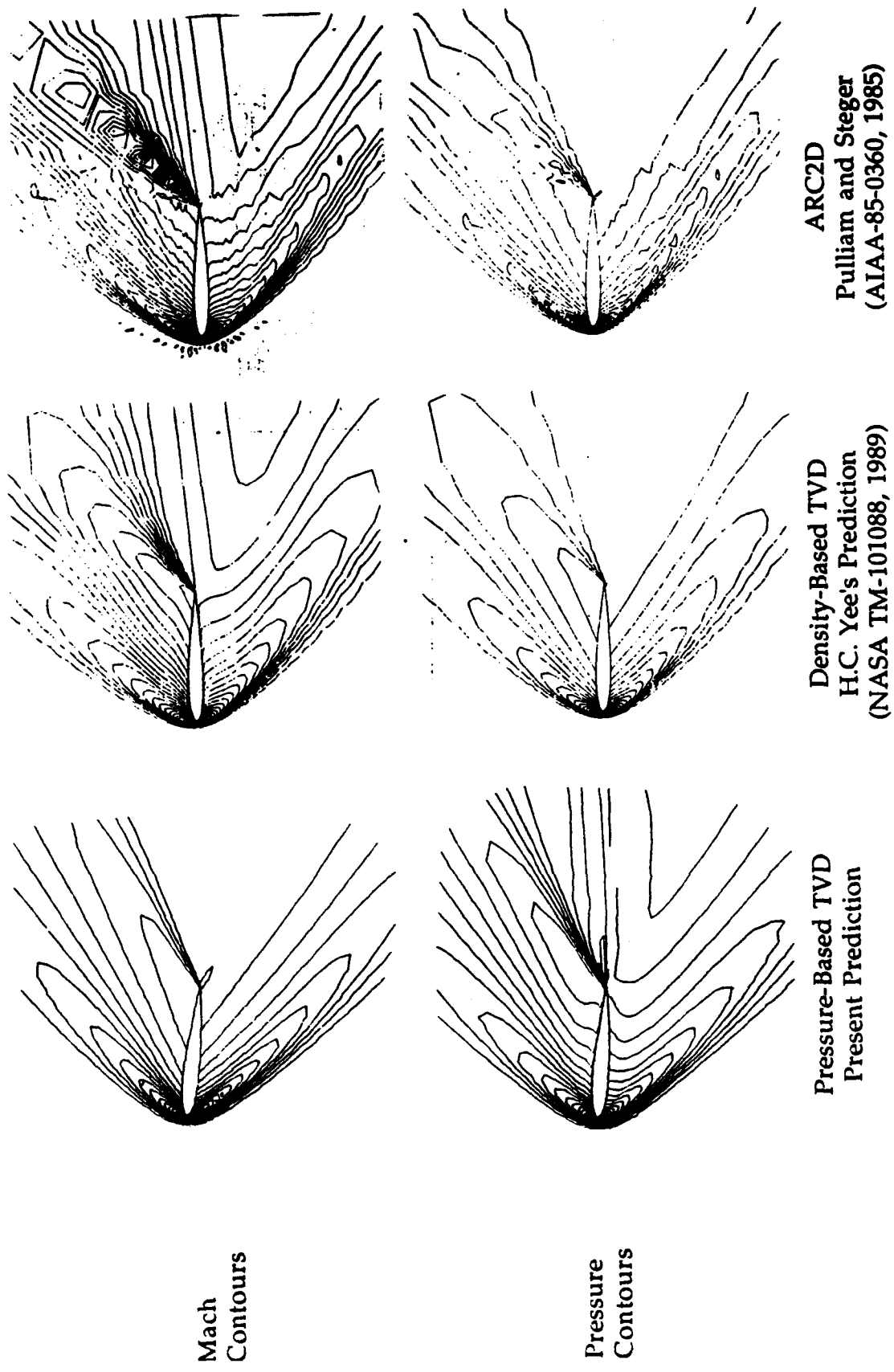


Figure 4-3. Comparison of the Present Pressure-Based TVD, Yee's Density-Based TVD and ARC2D for Supersonic Flow Over a NACA0012 Airfoil at $M_\infty = 1.8$ and $\alpha = 7.0^\circ$

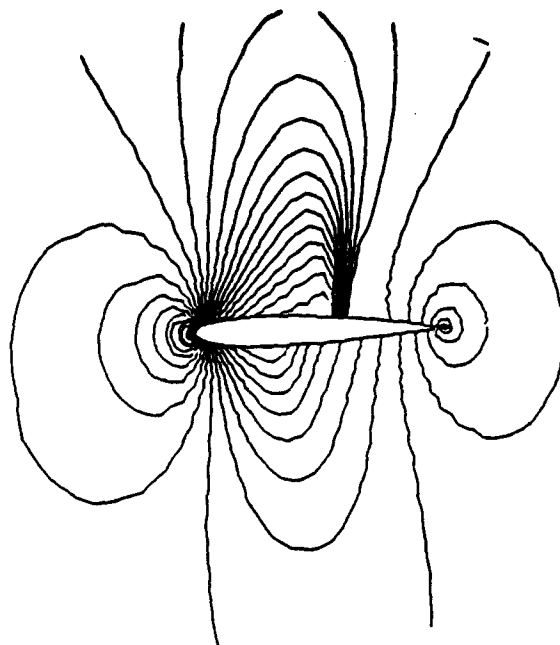
other hand, did rather poorly. The version of ARC2D⁹⁶ is based on the Beam-Warming ADI algorithm,²⁶ and uses a mixture of second- and fourth-order numerical dissipation terms. Due to the adaptive damping property inherent in TVD schemes, one can capture a shock in one to two grid points without the associated spurious oscillations near shock waves as opposed to three to four by ARC2D.

The above argument is proved in Figure 4-4 which shows the pressure distribution around the NACA 0012 airfoil when $M_\infty = 0.8$ and $\alpha = 1.25^\circ$ calculated by the present TVD scheme. From the pressure coefficient, one can clearly see that there is only one transonic point. The quality of the result is remarkable.

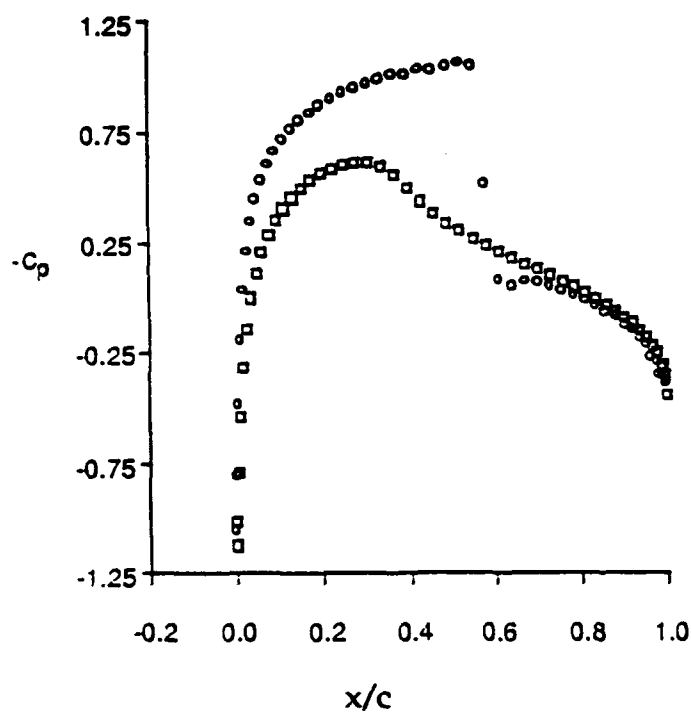
To prove the superior convergence rate of the proposed Newton's iteration method, along with hyperbolic pressure correction, Figure 4-5 shows the comparison between the regular iteration method by SIMPLEX algorithm and the present Newton's iteration method. Undoubtedly, residual errors drop dramatically at a constant rate by the present Newton's iteration, whereas traditional iteration method deteriorates and slows down with the number of iterations. Most importantly, for some problems where shock is strong, regular iterative method cannot converge, while the Newton iteration can bring the residual error down by several orders of magnitude without any difficulties!

4.2 Steady, Viscous Transonic Flow Over a NACA 0012 and an ARE 2822 Airfoil

A Viscous Transonic Airfoil Workshop was held during AIAA 25th Aerospace Sciences Meeting in 1985. In this workshop a series of two-dimensional airfoil Navier-Stokes computations were presented to establish the capability of various methods for computing viscous flow fields for a range of conditions and geometries. A compendium of the results is given by Holst.⁹⁷



(a) Pressure Contours



(b) Pressure Coefficient

Figure 4-4. Transonic Flow over a NACA 0012 Airfoil at $M = 0.8$ and $\alpha = 1.25$ by the Present Pressure-Based TVD Scheme

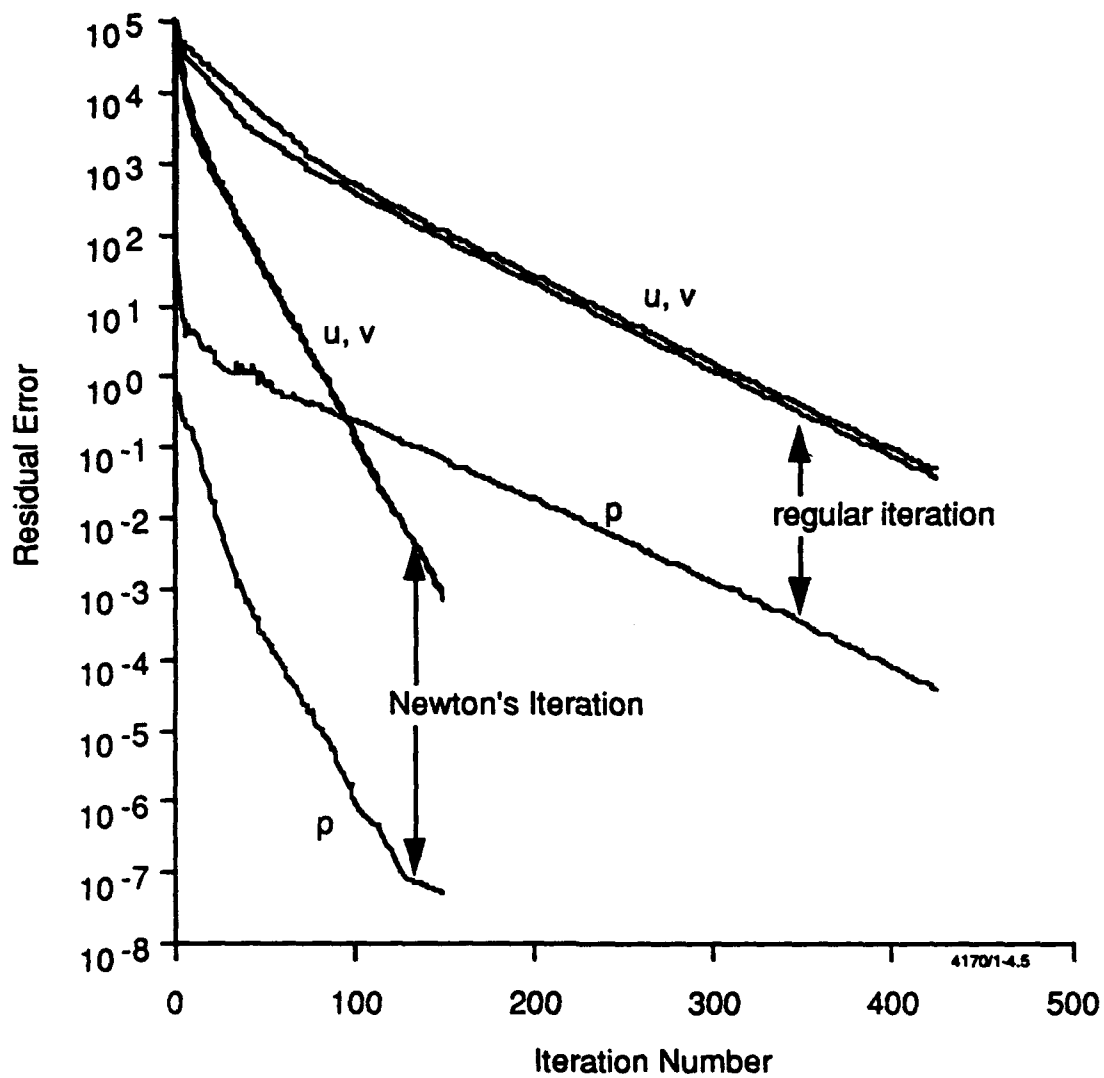


Figure 4-5. Convergence History of Regular Iteration Method and Newton's Iteration Method with Hyperbolic Pressure Correction for Inviscid Flow Over a NACA 0012. Grid 100×50 , $M_\infty = 0.8$, and $\alpha = 1.25^\circ$

The purpose of the present simulations is to evaluate the performance of the modified REFLEQS code in the numerical simulation of complex turbulent flows. The test cases have included a variety of different situations ranging from attached subcritical to transonic flows with both shock-induced and angle-of-attack-induced separations.

The Baldwin-Lomax algebraic eddy viscosity turbulence model⁸⁵ has been employed in the present study for the analysis of transonic airfoil flow. The model was chosen for its computational speed and simplicity. In addition, it has been shown to yield accurate results for many steady flow airfoil computations.^{98,99} The solutions are assumed to have reached convergence when the residual of all equations has dropped at least five orders of magnitude.

4.2.1 NACA 0012 Airfoil

Three computations were made for the NACA 0012 airfoil corresponding to experimental results of Harris.¹⁰⁰ All three were computed at a Reynolds number of 9 million. The grid used for the present NACA 0012 airfoil is a 200 x 63 O-mesh with outer boundary extending up to 12c (see Figure 4-6 for local view of the grid).

Figure 4-7a shows the computed surface pressure coefficients in comparison with experiments at $M_\infty = 0.7$, and a corrected angle-of-attack of 1.49° . Agreement is excellent. For this case, the flow is attached and just slightly supersonic near the leading edge upper surface. From density contours of Figure 4-7b, one can identify the development of viscous boundary layer on the airfoil surface. This comparison indicates satisfactory performance of the present code for attached, weakly transonic flow.

At a higher angle-of-attack of 8.34° , $M_\infty = 0.55$, agreement with experiment is good everywhere except near the shock, as shown in Figure 4.8a. Again, the angle of attack used in the computation (8.34°) is the corrected value obtained by Harris from the measured value (9.86°) using a linear analysis for wind tunnel-wall effects. For this case, the flow has a supersonic bubble located well forward on the airfoil upper surface and is slightly separated at the foot of the shock. The computation predicts the shock location slightly aft of experiment, but it does show (from Figure 4.8b) the small shock-induced separation evident in Harris's measurements between $x/c = 0.1$ and 0.2 .

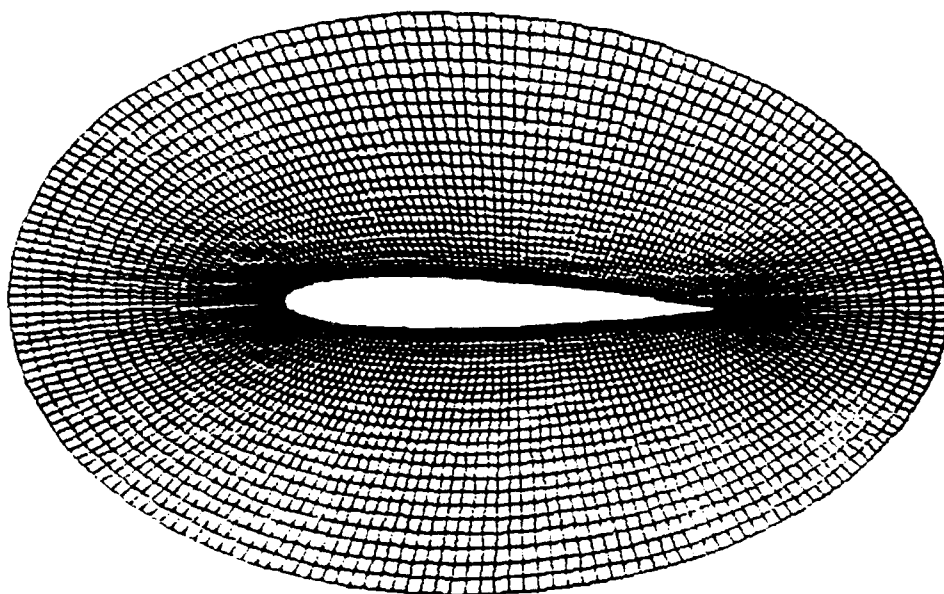
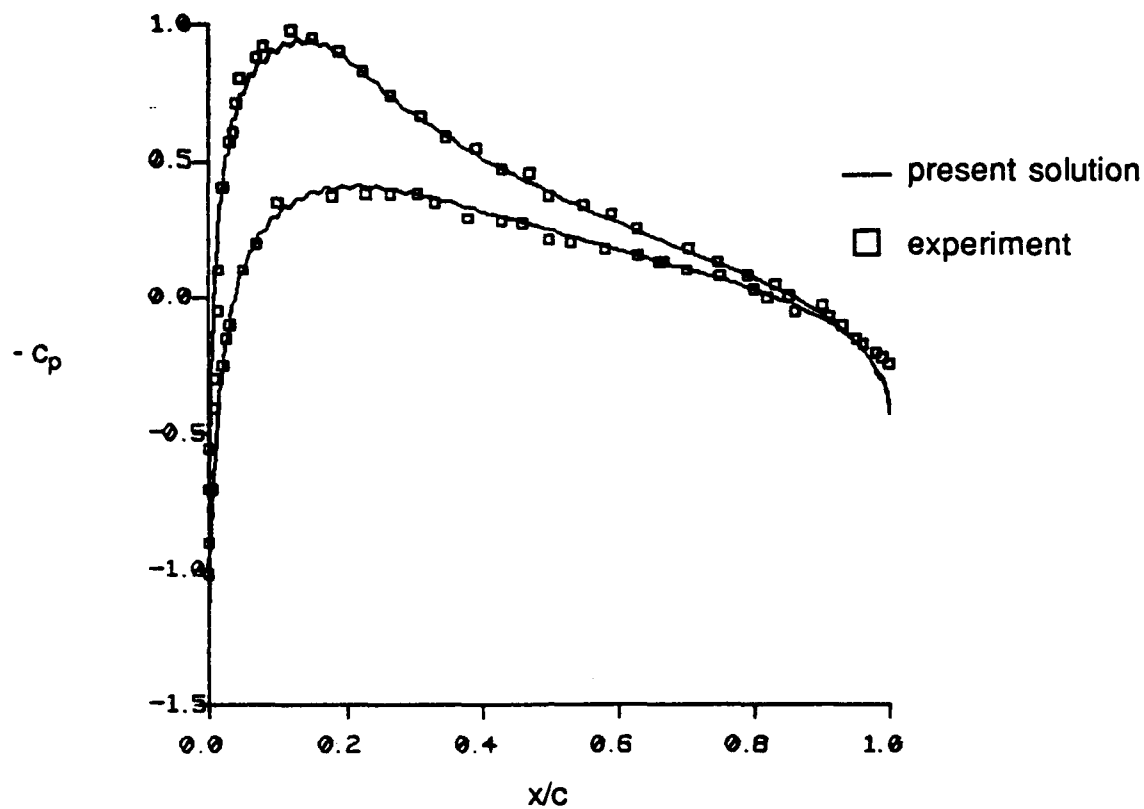
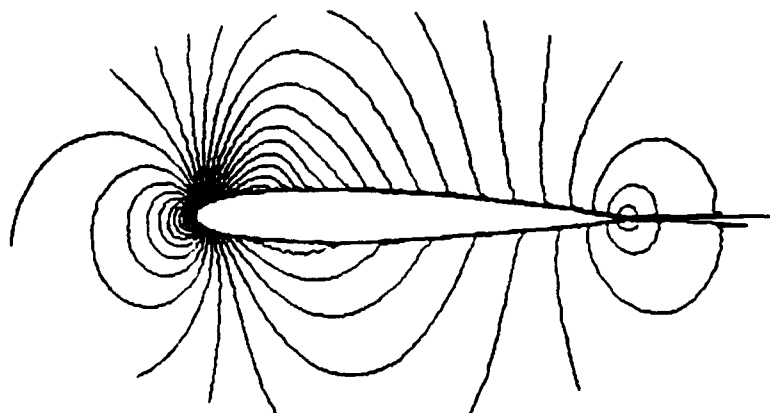


Figure 4-6. Grid Distribution (200×63) for a
NACA 0012 Airfoil for Viscous Transonic Computation

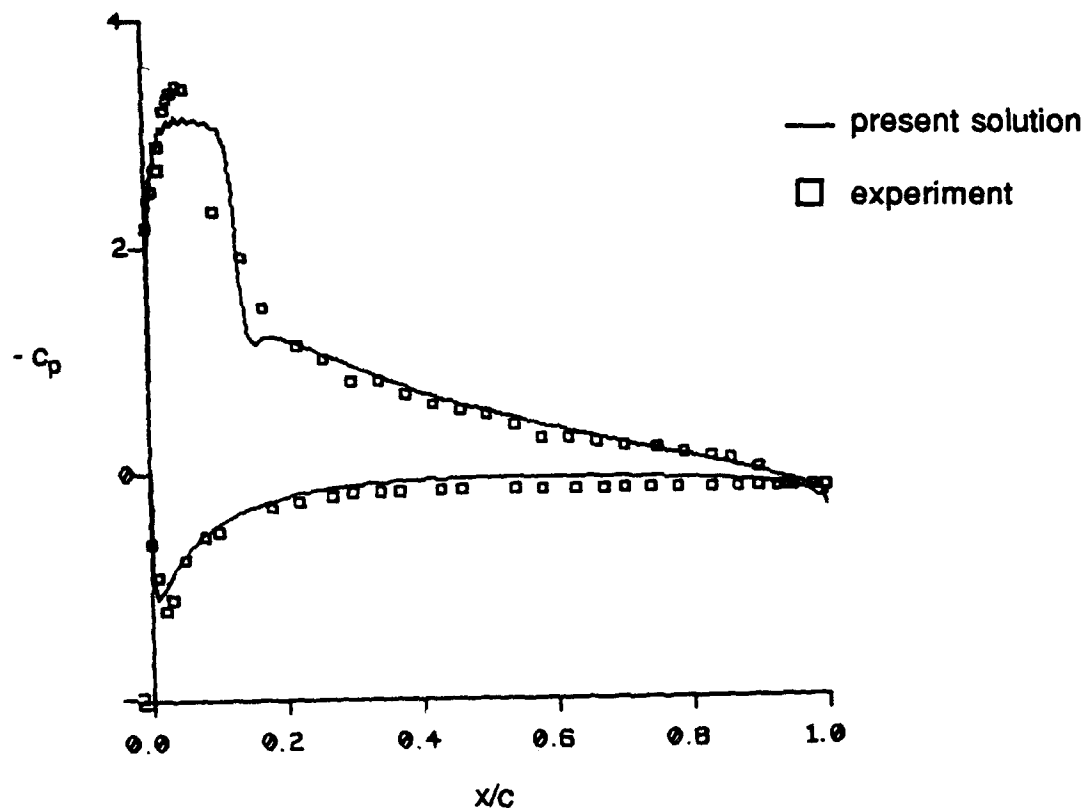


(a) Pressure Coefficient

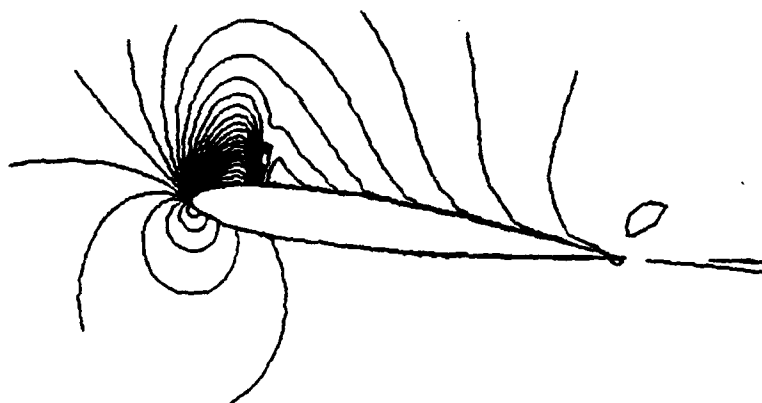


(b) Density Contours

Figure 4-7. Results of Viscous Transonic Flow Over a NACA 0012 Airfoil
at $\alpha = 1.49^\circ$, $M_\infty = 0.7$, and $Re = 9 \times 10^6$



(a) Pressure Coefficient



(b) Density Contours

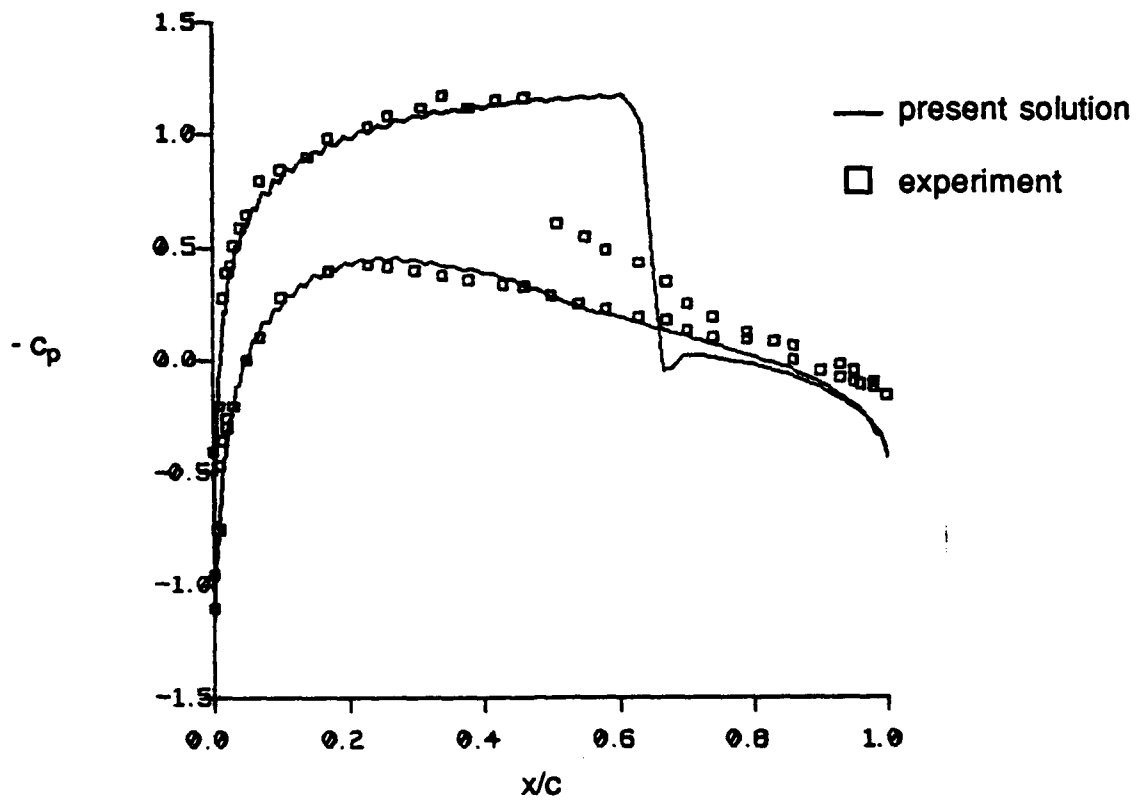
Figure 4-8. Results of Viscous Transonic Flow Over a NACA 0012 Airfoil
at $\alpha = 8.34$, $M_\infty = 0.55$, and $Re = 9 \times 10^6$

Figure 4-9a is a plot of pressure coefficient for the NACA 0012 airfoil at $\alpha = 2.26^\circ$, $M_\infty = 0.749$. Again, the angle 2.26° is obtained from the measured angle of attack (2.86°) using a linear wind-tunnel-wall correction procedure. For this flow field, a shock wave exists on the airfoil upper surface at about $x/c = 0.5$, which is strong enough to cause significant boundary-layer separation. For this case, like many others^{97,101-103} the present theory with the Baldwin-Lomax model does not capture the shock location accurately, and predicts its location too far aft of experiment.

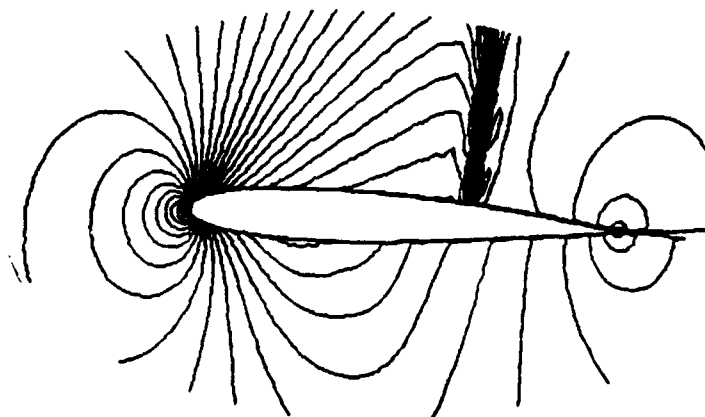
At a Mach number of 0.7, several angles of attack were computed to produce the lift coefficient C_L versus angle of attack α plot of Figure 4-10. The experimental data of Harris and the data with wind-tunnel-wall correction are shown. Agreement with the corrected data of Harris is very good.

4.2.2 RAE 2822 Airfoil

Two studies were completed for the RAE 2822 airfoil, corresponding to Case 1 and Case 6 from the experimental study of Cook, *et al.*¹⁰⁴ A 144×69 O-grid around the airfoil was generated by an algebraic method, and is shown in Figure 4-11. The outer boundary is located at a distance of 12 chord away. This airfoil is a supercritical airfoil with a significant amount of aft camber. Unlike NACA 0012, only one experiment¹⁰⁴ is available and the experimental accuracy is unknown. Case 1 of Reference 104 was simulated at $M_\infty = 0.676$, $Re = 5.7 \times 10^6$, and a corrected angle-of-attack of 1.93° . The surface pressure coefficients for this subcritical case in comparison to the experiment are given in Figure 4-12. As can be seen, both results are in good agreement.



(a) Pressure Coefficient



(b) Density Contours

Figure 4-9. Results of Viscous Transonic Flow Over a NACA 0012 Airfoil
at $\alpha = 2.26$, $M_\infty = 0.749$, and $Re = 9 \times 10^6$

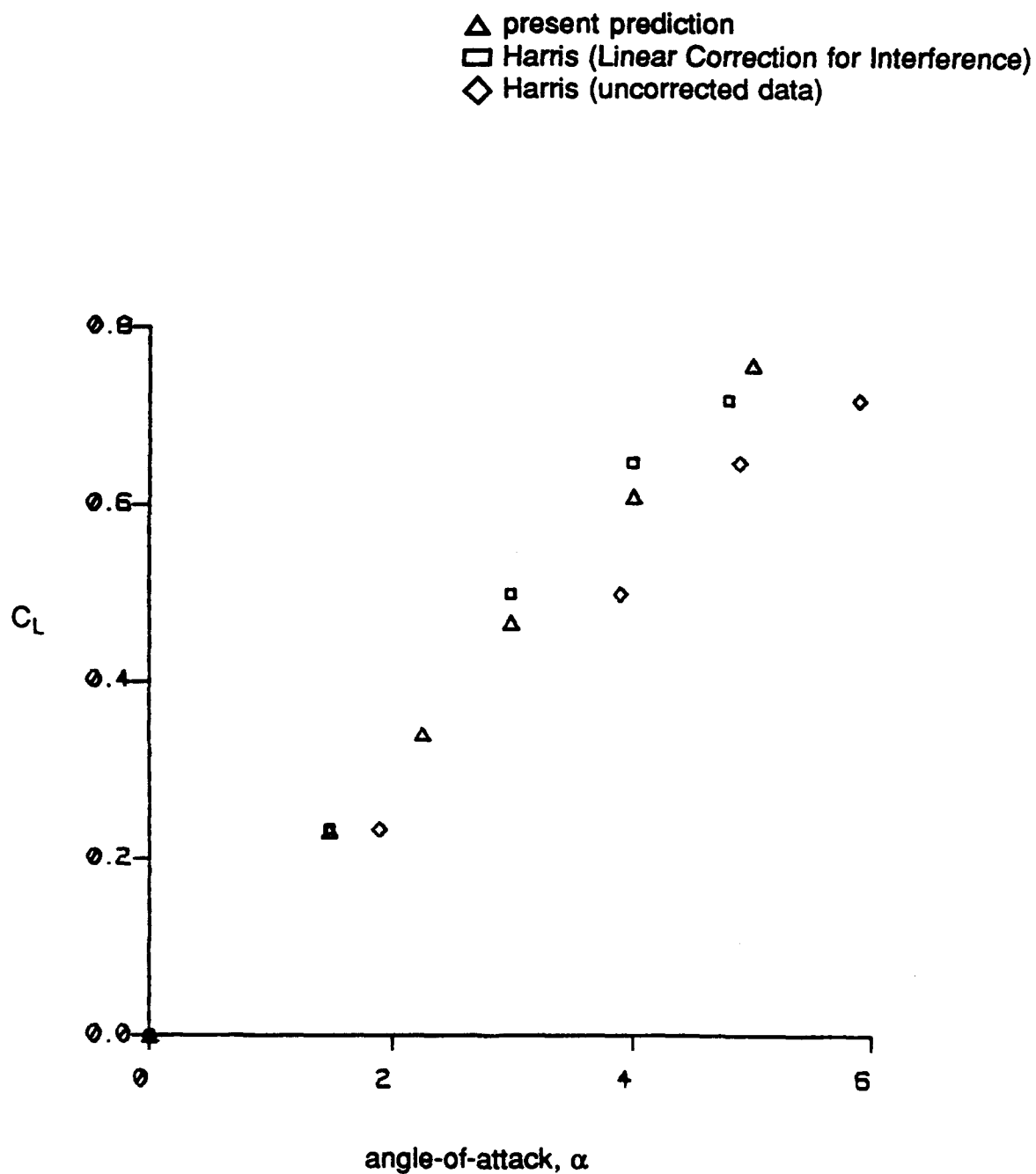


Figure 4-10. Lift Coefficients (C_L) vs. Angle-of-Attack for Transonic Flow Over a NACA 0012 at $M_\infty = 0.7$, and $Re = 9 \times 10^6$

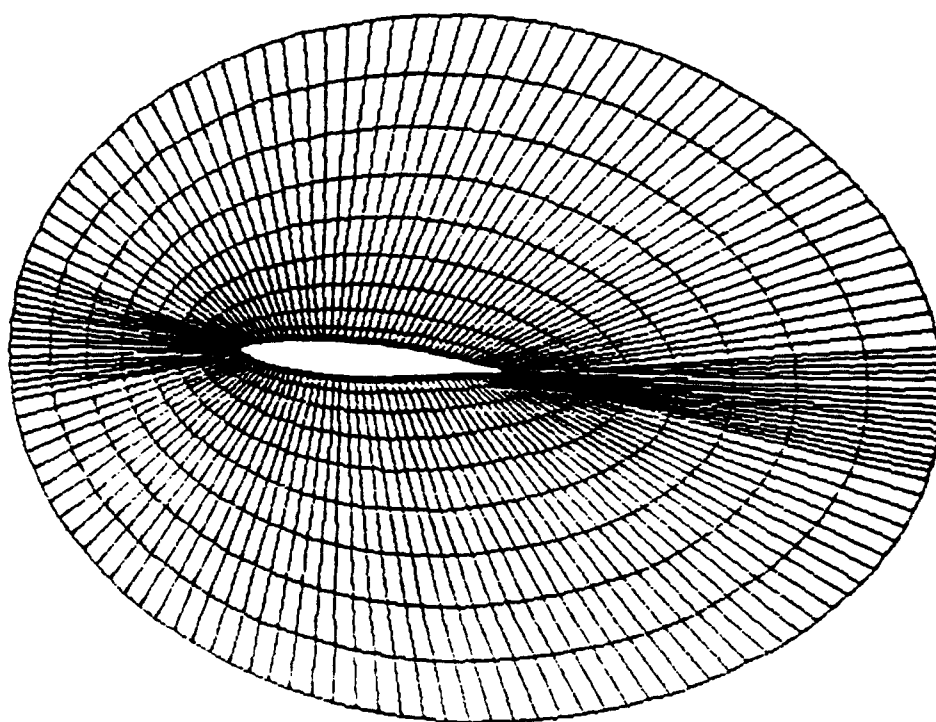
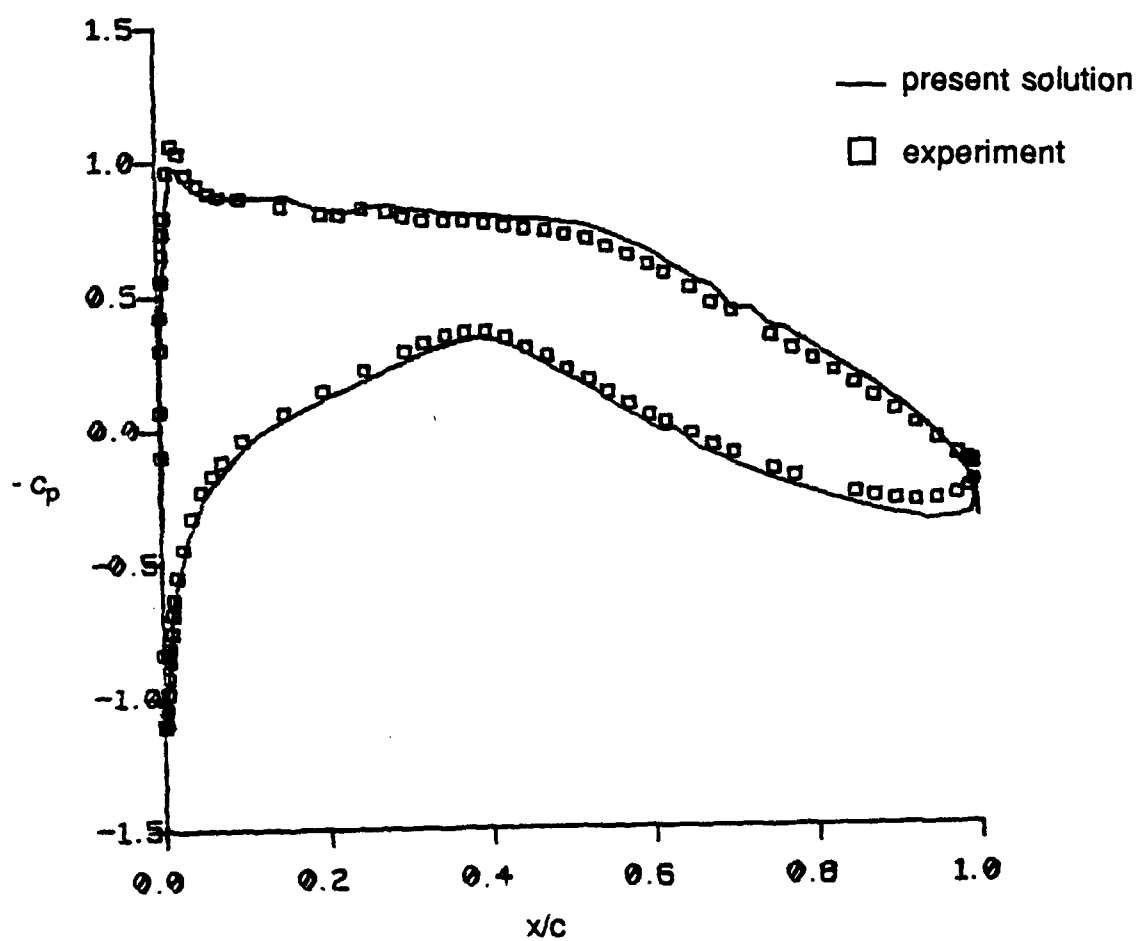


Figure 4-11. O-Grid (144 x 64) Around RAE 2822
Airfoil For Viscous Transonic Computations



Pressure Coefficient

Figure 4-12. RAE 2822 Airfoil Surface Pressure Distribution at $M_\infty = 0.749$, $Re = 9 \times 10^6$, and $\alpha = 1.93^\circ$ (Case 1)

Case 6 was computed at $M_\infty = 0.725$, $Re = 6.5 \times 10^6$, and a corrected angle-of-attack of 2.79° . Figure 4-13 shows the surface pressure coefficients in comparison to the experiment. The present method agrees fairly well everywhere, although the shock location is predicted slightly forward of the experiment.

4.3 NACA 0015 Airfoil Undergoing Constant Rate Pitching Motions

In this case, we considered a NACA 0015 airfoil pitching about a fixed axis at a constant rate from zero incidence to a maximum angle-of-attack of approximately 60° . This particular airfoil section was selected because many experimental studies are available.¹⁰⁵⁻¹⁰⁸ To accommodate the time-dependent coordinate transformation (moving grid) in the present flow simulation, a "rigid" grid attached to the airfoil is used. The advantage of this approach is that once an initial grid is generated, the physical coordinates (x,y) and grid speed (ξ_t, η_t) can be easily computed from the prescribed airfoil motion.

The free stream Mach number is 0.02 and the chord Reynolds number is 4.5×10^4 , which are the same as experiment of Walker, *et al.*¹⁰⁶. The laminar flow is assumed, as in the work of Rumsey and Anderson,²⁰ and Visbal and Shang.¹⁸

This laminar assumption can be justified from the following two reasons. First, a suitable model for transition and turbulence is not currently available for the present complex unsteady flow. Second, for the high pitch-rate regime, the energetic forcing motion is expected to temporarily dominate over some transition and turbulence effects. The favorable agreement shown below between the predicted and experimental flow features confirms the above hypothesis.

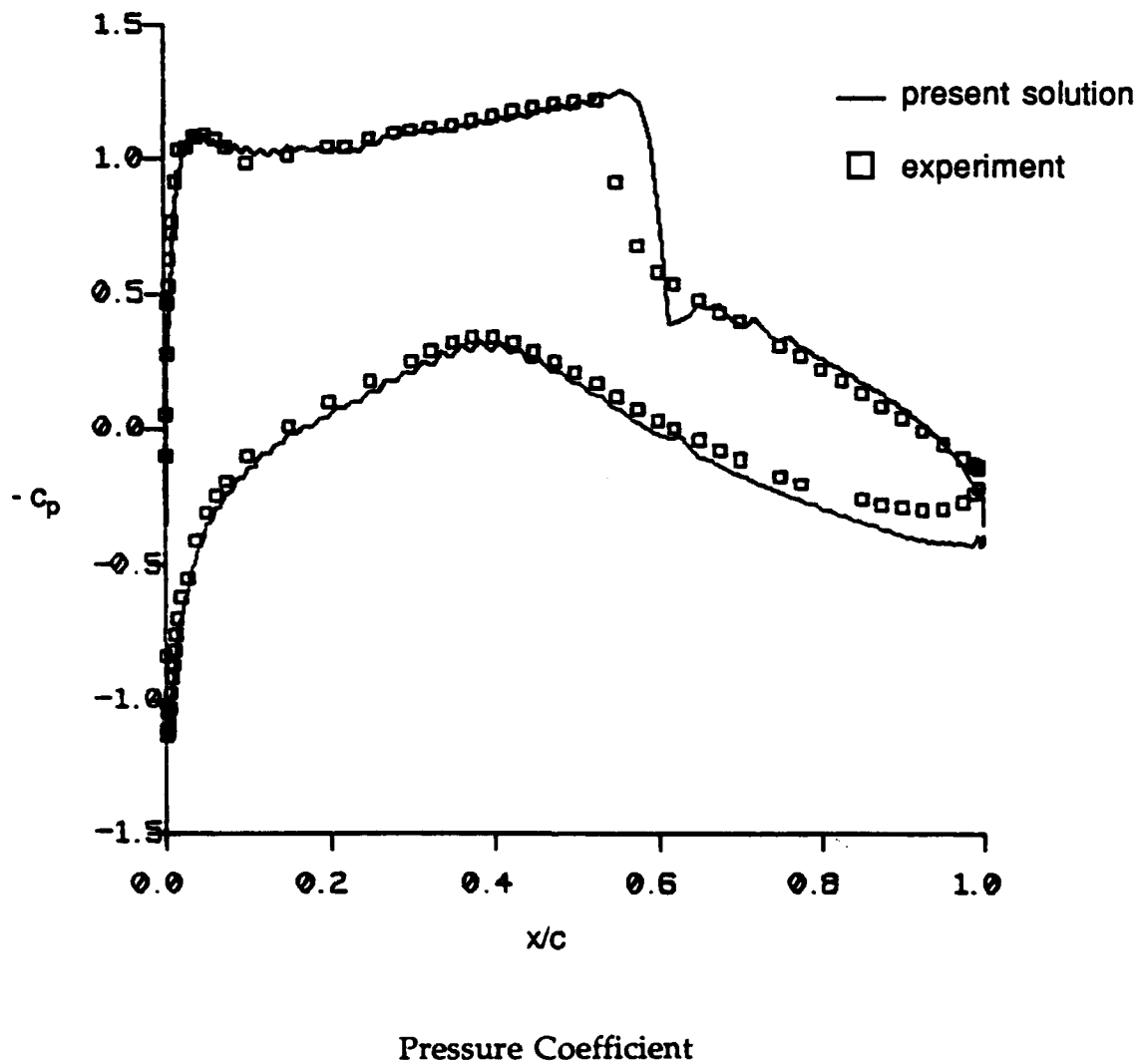


Figure 4-13. RAE 2822 Airfoil Surface Pressure Distribution at $M_\infty = 0.725$, $Re = 6.5 \times 10^6$, and $\alpha = 2.79^\circ$ (Case 6)

A grid of 200×77 with local view shown in Figure 4-14 was used in the present simulation. This grid size is compatible with the grid in the work of Rumsey and Anderson (257×97 C-grid)²⁰ and Visbal and Shang (203×101 O-grid)¹⁸. The grid extends 15 chords away from the airfoil. The temporal accuracy study has also been carried out, and it is found that for $\Delta t U_\infty / c = 0.002$ with first-order backward Euler in time, the solution is time-step independent. This time step was used in all the computations reported below.

Figure 4-15 displays the instantaneous streamlines at several angles of attack and the corresponding experimental visualization data for a non-dimensional pitch rate of $k = \alpha c / U_\infty = 0.2$.

Both experimental and computational data show a separation bubble (vortex) on the leading edge of the airfoil as well as a separated flow on the trailing edge at an angle of attack of 27° (Figure 4-15a). The leading edge vortex is also known as a dynamic stall vortex.¹⁰⁹ With the further increase in the angle of attack, Figure 4-15b, the leading edge vortex grows in size and convects along the upper surface. At the same time, a secondary bubble appears on the leading edge. At $\alpha = 59^\circ$, the dynamic stall vortex has grown to a size comparable with the airfoil chord length, and the flow falls into deep stall regime (Figure 4-15c). During the whole process, the flow is fully attached along the airfoil lower surface. In general, the present prediction compares favorably with the experiment of Walker, *et al.*¹⁰⁶

With an increase in the pitching rate to $k = 0.4$, the generation of the leading edge vortex is delayed until an angle of attack of 42° (Figure 4-16b). The trailing edge separation is visible at $\alpha = 28^\circ$ (Figure 4-16a). The vortical flow is less vigorous at $\alpha = 60^\circ$ (Figure 4-16c) in comparison to the case of $k = 0.2$ of Figure 4-15c. Again, the calculations predict well the experimental phenomenon.

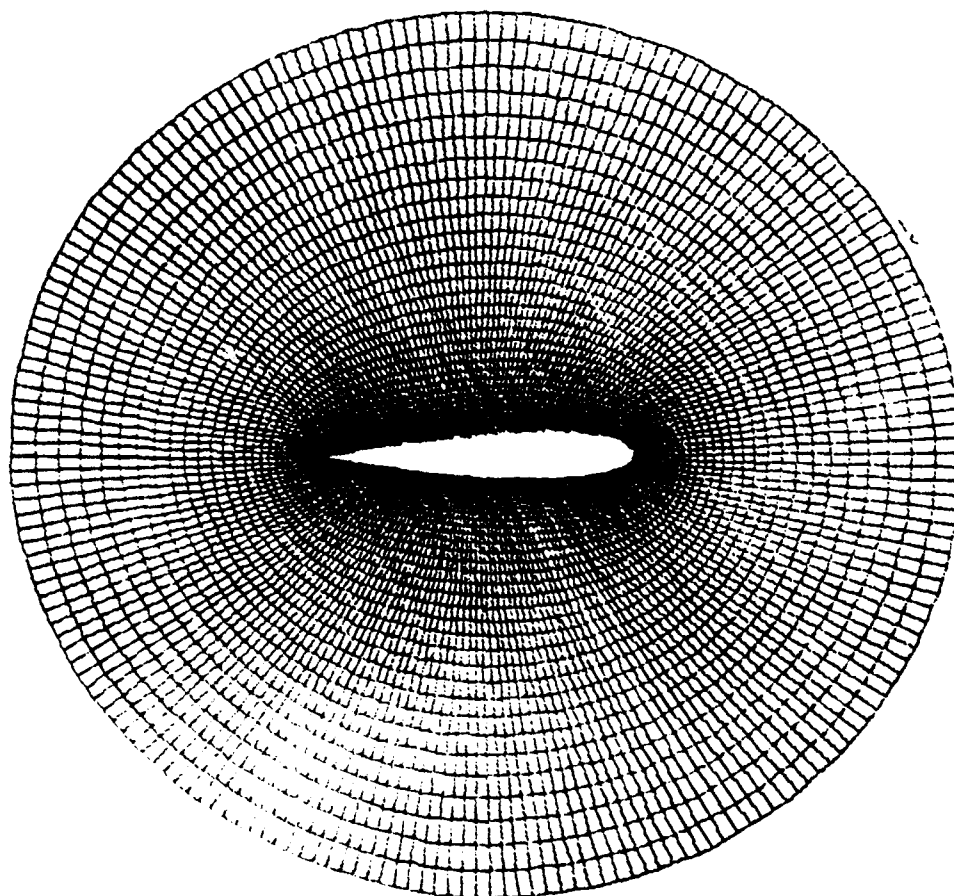
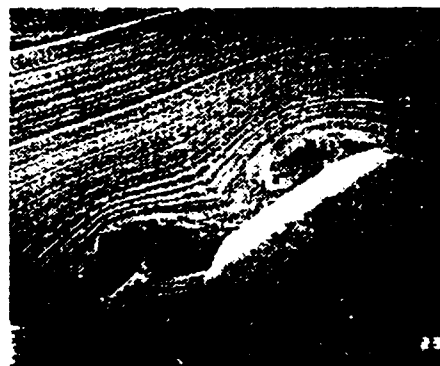
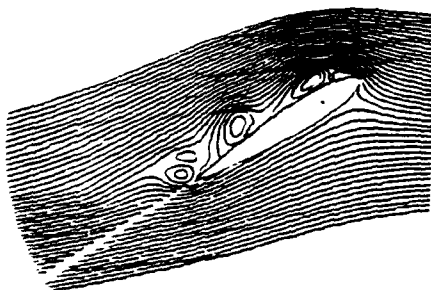


Figure 4-14. Local View of a 200×77 O-Grid Around
NACA 0015 Airfoil for Constant Pitch-Rate Simulation

present prediction

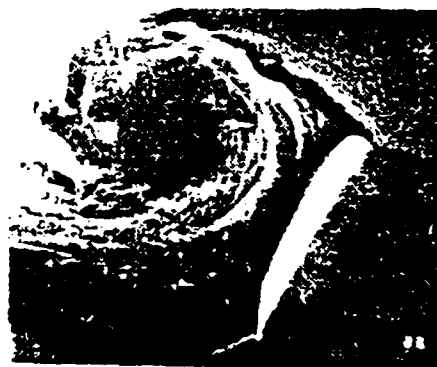
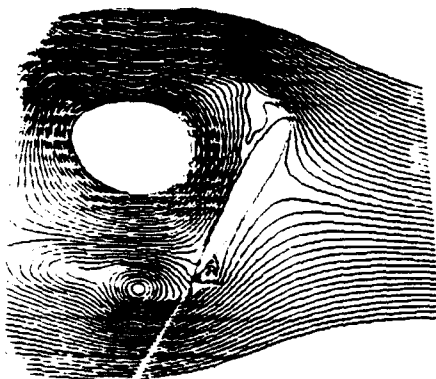
experiment



(a) $\alpha = 27^\circ$



(b) $\alpha = 46^\circ$

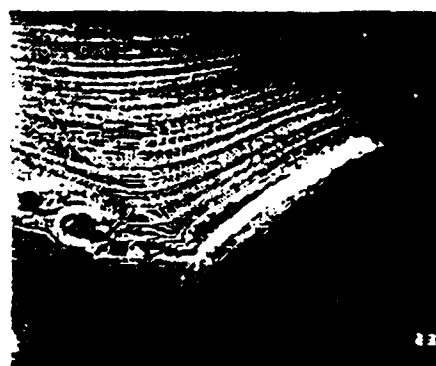
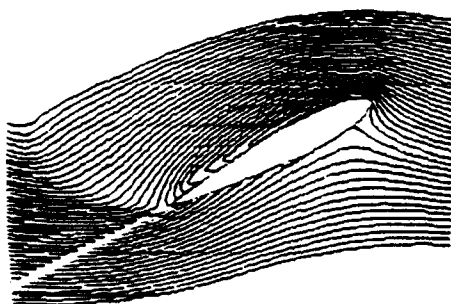


(c) $\alpha = 59^\circ$

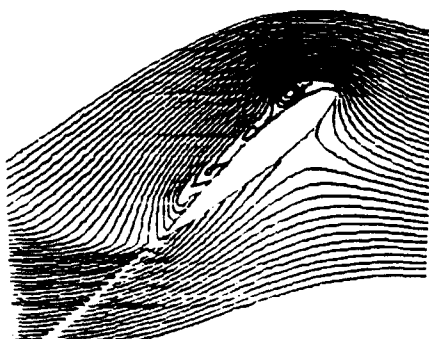
Figure 4-15. Comparison of Computed Flow Field With Experiment for NACA 0015 Airfoil at Constant-Rate Pitch, $Re = 45,000$, $k = 0.2$, 200×77 grid

present prediction

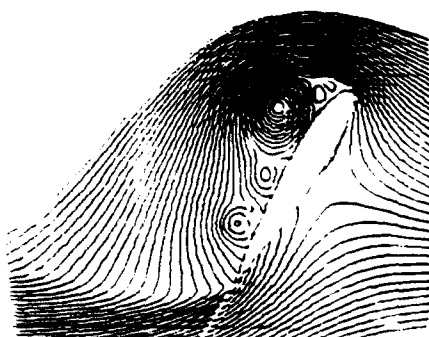
experiment



(a) $\alpha = 28^\circ$



(b) $\alpha = 42^\circ$



(c) $\alpha = 60^\circ$

Figure 4-16. Comparison of Computed Flow Field With Experiment for NACA 0015 Airfoil at Constant-Rate Pitch, $Re = 45,000$, $k = 0.4$, 200×77 grid

It should be emphasized that the pressure-based method can deal with highly compressible and incompressible flows with equal efficiency, while the density-based method has difficulties for the simulation of low Mach number flows, such as the experiment in Reference 106, where $M = 0.02$. It is due to this fact that Rumsey and Anderson,²⁰ and Visbal and Shang¹⁸ used $M = 0.2$ in their simulations.

4.4 NACA0012 Undergoing Oscillatory Pitching Motion at Transonic Conditions

Unsteady calculations were performed for a NACA 0012 airfoil pitching harmonically about the quarter chord with the following relation of angle-of-attack.

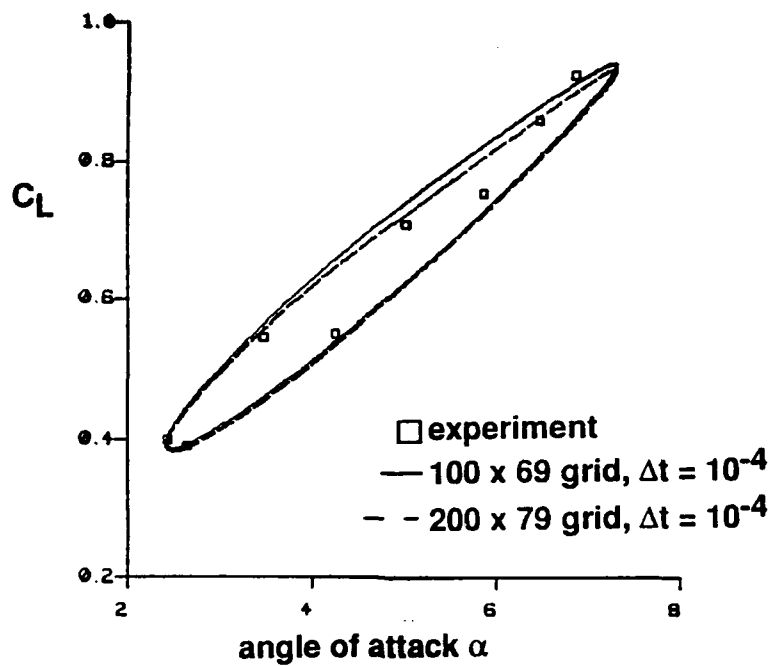
$$\begin{aligned}\alpha &= \alpha_m + \Delta\alpha \sin \omega t \\ \alpha_m &= 4.86^\circ, \Delta\alpha = 2.44^\circ\end{aligned}\tag{4.1}$$

The non-dimensional reduced frequency, k , defined as:

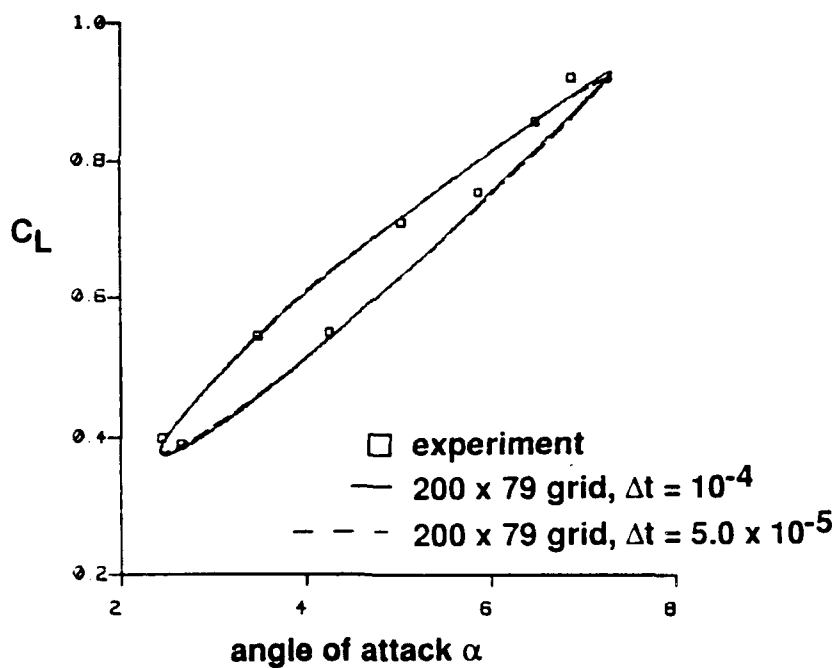
$$k = \frac{\omega c}{2U_\infty}\tag{4.2}$$

is 0.081. The free-stream Reynolds number is 4.8×10^6 , and Mach number is 0.6. Both 200×79 and 100×69 O-grids similar to Figure 4-6 are used in the present simulations. Third-order TVD scheme and second-order Crank-Nicolson in time are applied. The time step is 10^{-4} second, resulting in approximately 2,000 time steps per pitching cycle. The Baldwin-Lomax turbulence model is applied to account for the turbulence effects at this high Reynolds number.

Figure 4-17a shows lift coefficients as a function of angle-of-attack for two mesh sizes of 200×79 and 100×69 . The curves are followed in a counter-clockwise sense, *i.e.*, increase in α is represented on the lower portion of the plots. Both grids give good agreements with experimental data of London.¹¹⁰ Another computation with



(a) spatial accuracy



(b) temporal accuracy

Figure 4-17. Lift Coefficient for a NACA 0012 Airfoil Undergoing Oscillatory Motion, $Re = 4.8 \times 10^6$, $M_\infty = 0.6$, and $k = 0.081$

reduced time step size by a half ($\Delta t = 5.0 \cdot 10^{-5}$) with 200×79 grid (see Figure 4-17b) overlaps the one with $\Delta t = 10^{-4}$, which indicates the time step independence of the present solution.

The pressure coefficients at several angles-of-attack during a pitching cycle are compared with experimental measurement,¹¹⁰ as shown in Figure 4-18. The \uparrow symbol denotes that the angle-of-attack is increasing, and \downarrow denotes decreasing. As can be seen, the agreement is remarkable considering the complexity of the flow.

The generation and disappearance of a shock wave on the airfoil upper surface can be identified from the pressure coefficients. Figure 4-19 plots the density fields at several angles-of-attack within a pitching cycle. During the oscillatory motion, there is a shock wave on the upper surface of the airfoil, and the flow over the lower surface is predominately subcritical. Both pressure distributions and density contours indicate that the shock position oscillates over approximately 25% of the chord.

4.5 Parametric Effect on Dynamic Stall on the Airfoils

As it is generally known, dynamic stall depends on many parameters. This subsection intends to investigate the influence of some of these parameters and to explore the capability of the present code in predicting dynamic stall phenomenon under various conditions.

□ experiment

— present prediction

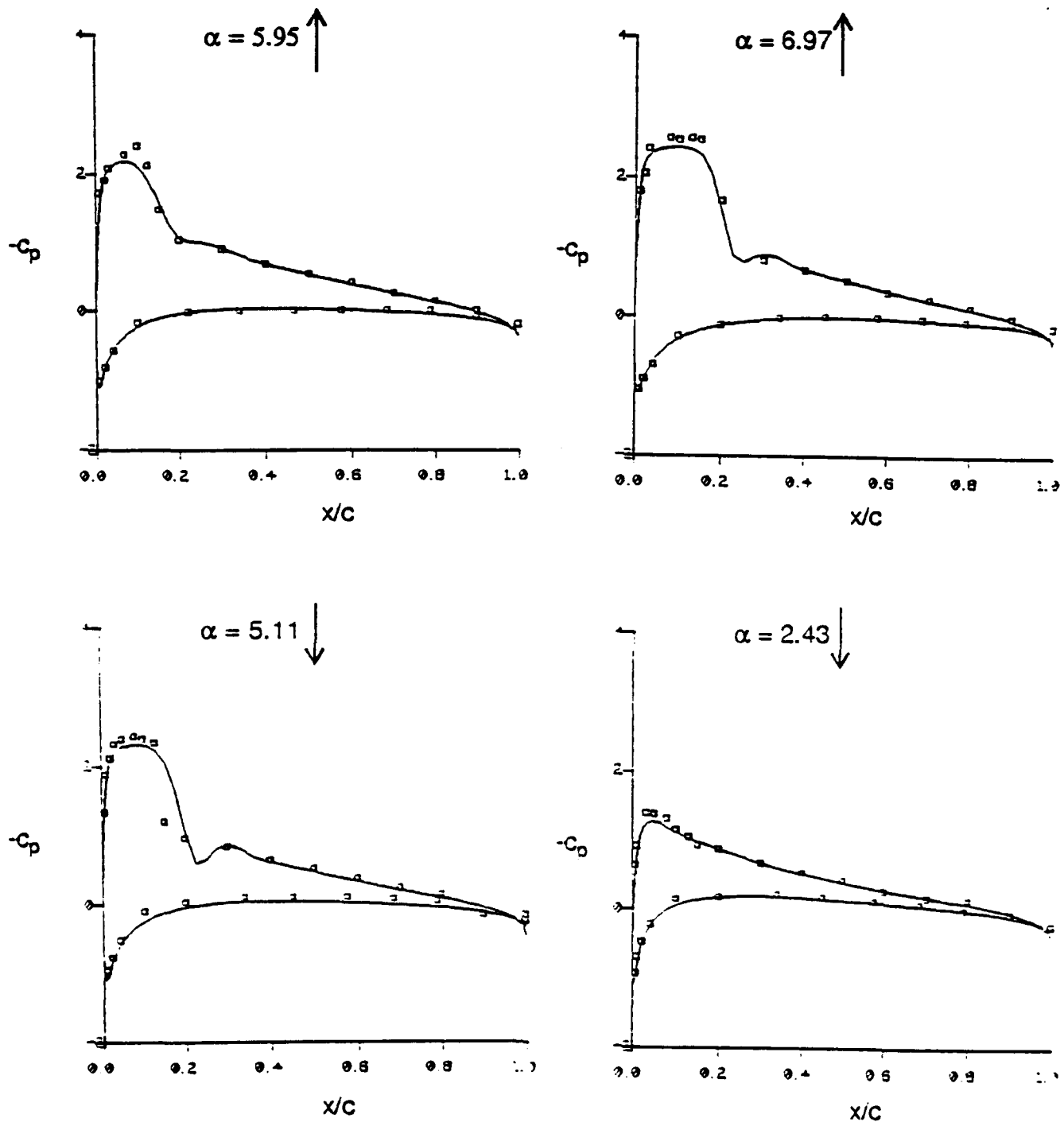


Figure 4-18. Pressure Coefficients for a NACA 0012 Airfoil Undergoing Oscillatory Motion, $Re = 4.8 \times 10^6$, $M_\infty = 0.6$, and $k = 0.162$

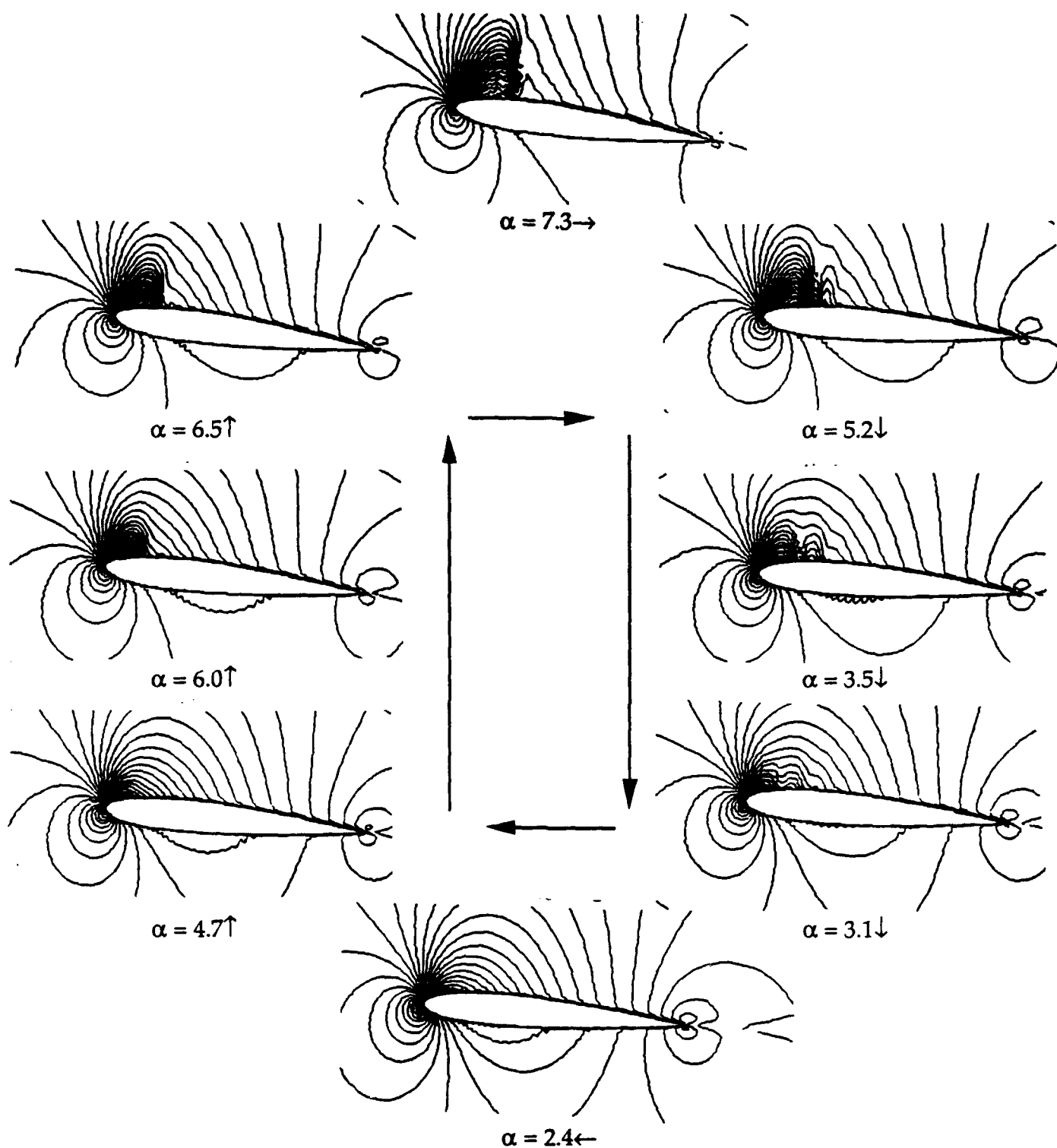


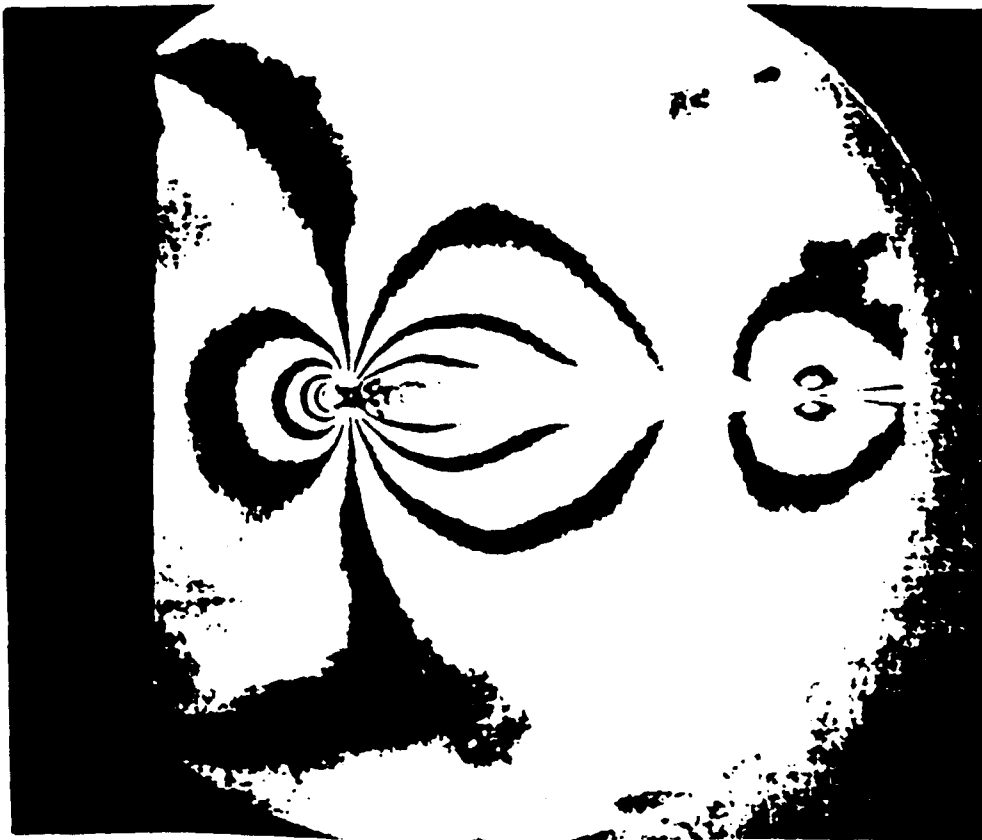
Figure 4-19. Density Contours Around a NACA 0012 Airfoil Harmonically Pitching About Quarter Chord, $Re = 4.8 \times 10^6$, $M = 0.6$, and $k = 0.162$

4.5.1 Compressibility Effect

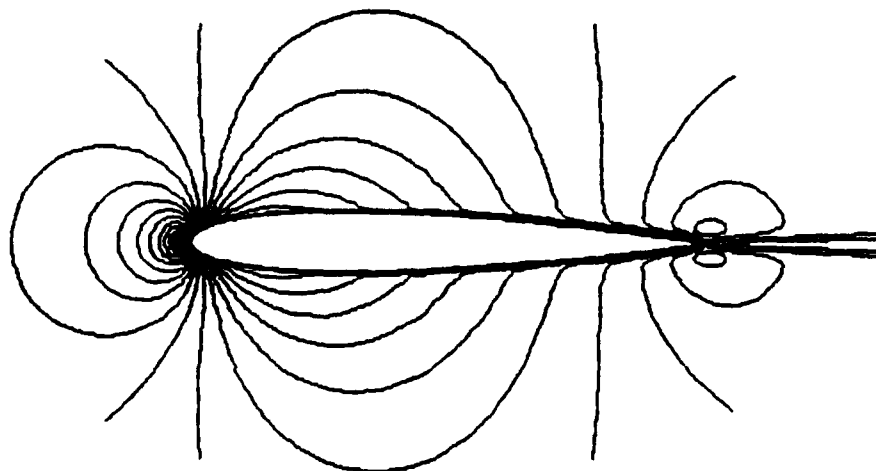
Here the experiments of Carr *et al*⁴² and Ahmed and Chandrasekhara⁴⁴ were simulated. The conditions are the same as in the experiments:

NACA0012 Airfoil	Chord Length $c=0.0762\text{m}$
Mach Number, $M_\infty = 0.3, 0.4$	Reynolds Number $Re = 5.4 \times 10^5$
Oscillating Frequency, $f = 21.64\text{Hz}$	Reduced Frequency, $k=0.05$
Angle of Attack as: $\alpha = \alpha_m + \Delta\alpha \sin \omega t$, $\alpha_m = 10^\circ$, $\Delta\alpha = 10^\circ$	

A grid containing 200×79 cells, as shown in Figure 4-6 is used. First, the steady state conditions are simulated. The density contours from the experiments of Carr *et al* using real time interferometry and from the present calculations are shown in Figure 4-20 and Figure 4-21. For Figure 4-20, $M_\infty = 0.4$ and $\alpha = 0.0^\circ$, whereas for Figure 4-21, $M_\infty=0.3$ and $\alpha = 10.78^\circ$. The experimental fringes seen are the constant density contours. The stagnation point in both experiment and calculation is characterized by the convergence of circular fringes (contours) which appear at the leading edge. The density contours are symmetric on both the upper and lower surfaces in Figure 4-20, which is appropriate for this 0° angle of attack. The abrupt turning of the density contours on the upper surface indicates the presence of boundary layer. At $\alpha = 10.78^\circ$ in Figure 4-21, the stagnation point moves to the lower surface of the airfoil. The concentration of fringes and contours near the leading edge indicates strong acceleration in that region. It is clearly seen that the present solutions correctly simulate the experimental observations.



(a) Experiment of Carr *et al.* (AIAA-91-0017, 1991)

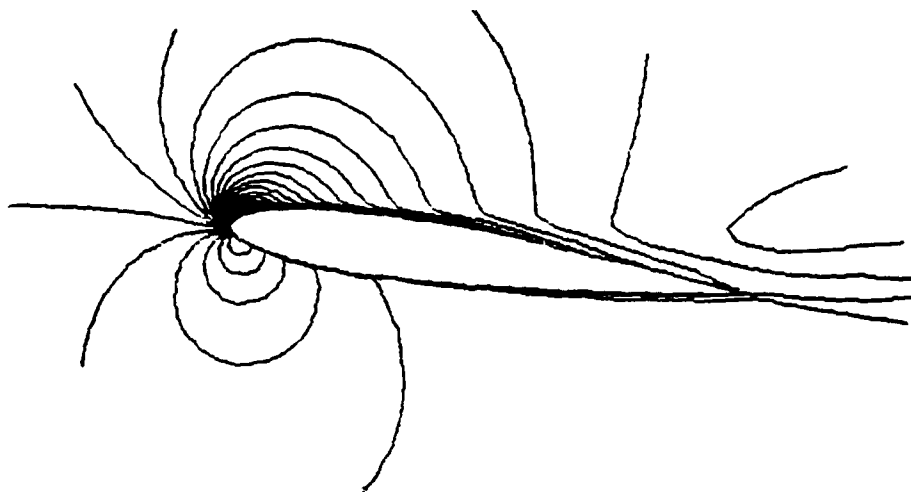


(b) Present Prediction

Figure 4-20. Comparison of Density Contours between the Present Prediction and Experiments of Carr *et al.* for Steady Flow over a NACA0012 at $M_\infty = 0.4$, $\alpha = 0.0$, and $Re = 5.4 \times 10^6$



(a) Experiment of Carr *et al.* (AIAA-90-0017, 1991)



(b) Present Prediction

Figure 4-21. Comparison of Density Contours between the Present Prediction and Experiments of Carr *et al.* for Steady Flow over a NACA0012 at $M_\infty = 0.3$, $\alpha = 10.78^\circ$, $Re = 5.4 \times 10^6$

Next the dynamic stall condition is simulated with $k=0.05$ and $M_\infty = 0.3$. The oscillatory motion is solved by marching in time with a constant time step. The time step size is such that it corresponds to 1,200 time steps to complete one oscillating cycle. The third-order TVD scheme in space and second-order accurate scheme in time are applied. The development of the unsteady flow field is shown in Figure 4-22. During the upstroke (\uparrow), at $\alpha = 4.3^\circ$ (Figure 4-22a) the flow is fully attached. As the airfoil reaches the proximity of the static stall angle ($\alpha \approx 12.0^\circ$), (Figure 4-22b), the attached flow persists. The boundary layer on the upper surface, however, has grown considerably, as seen from the density contours. At $\alpha = 20^\circ$ (Figure 4-22e), a shallow reversed flow region, which initiated at $\alpha = 12.0^\circ \uparrow$ (Figure 4-22b) at the trailing edge, expands upstream rapidly. This flow reversal grows in size and propagates upstream. It is this reversal flow that introduces an abrupt separation of the boundary layers and the subsequent development of a leading edge vortex. With further decrease in the angle of attack, the flow reattachment process starts from the leading edge downward (see Figure 4-22f-4-22k). At $\alpha = 6.4^\circ$, the flow on the upper surface attaches completely.

The local amplified view of density contours and experimental fringes during the reattachment process of the above oscillation cycle are shown in Figure 4-23. The leading edge bubble due to shear layer attachment and its growth can be observed.

4.5.2 Effect of Mean Angle of Attack

The effect of the mean angle of attack was studied by using the same conditions as the above, except that $\Delta\alpha = 6^\circ$, and α_m is selected as 6° and 12° . For $\alpha_m = 6^\circ$, it corresponds to light stall, and for $\alpha = 12^\circ$, it is a deep stall. The computed lift coefficients as a function of α in an oscillation cycle for $\alpha_m = 6^\circ$ and $\alpha_m = 12^\circ$ are shown in Figure 2-24. The experimental data of McCrosby¹ are also given. The comparison is fairly good.

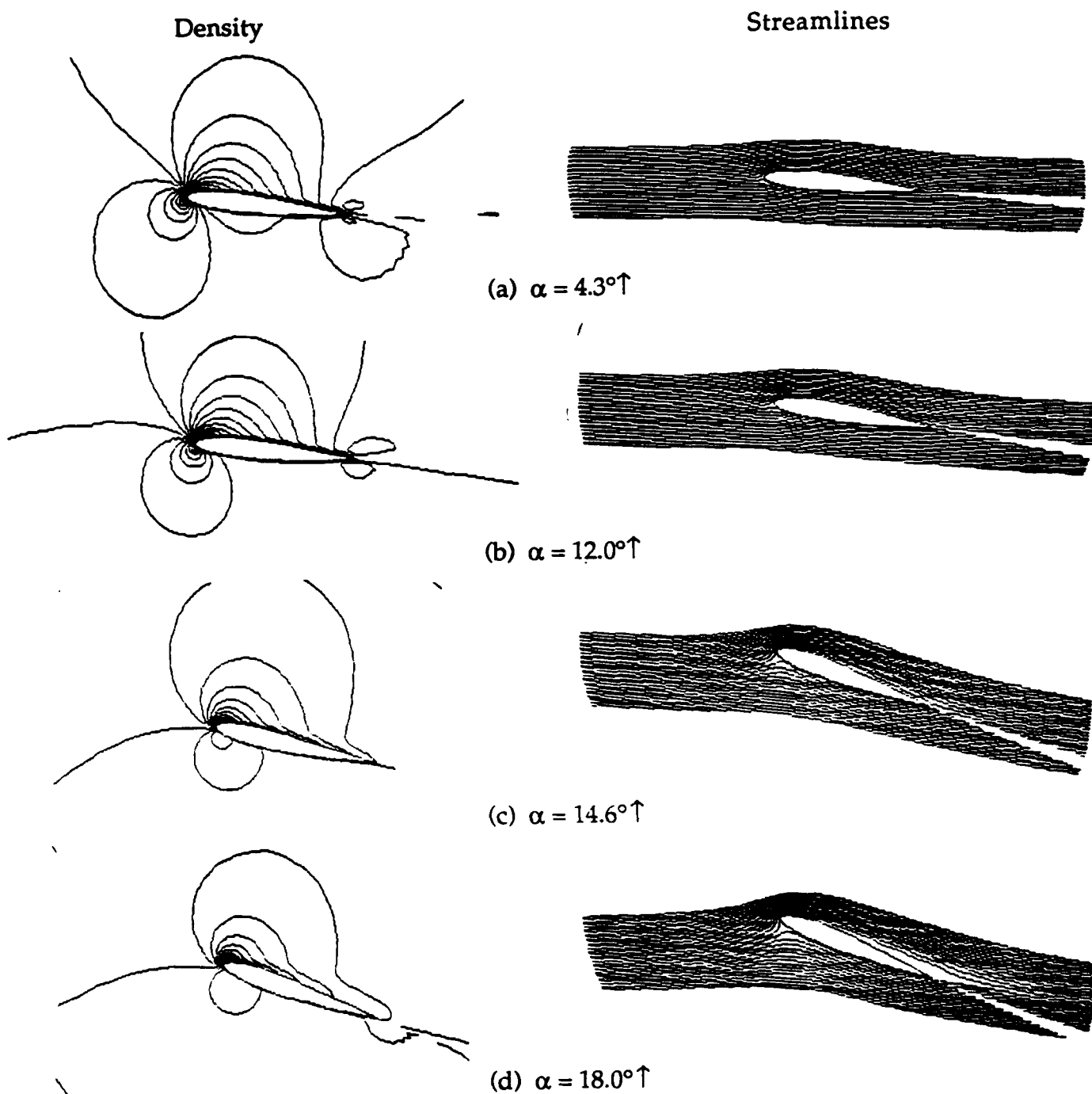
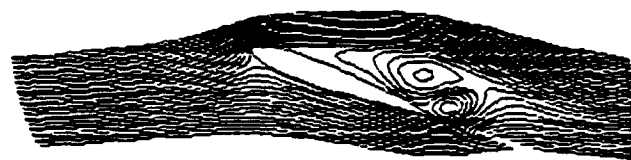
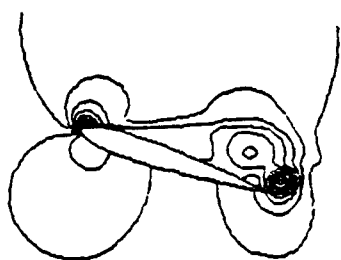


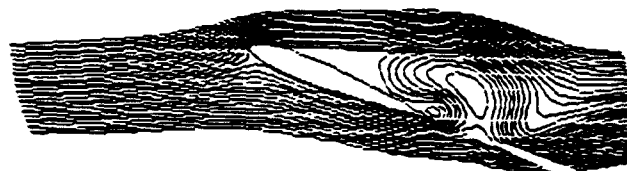
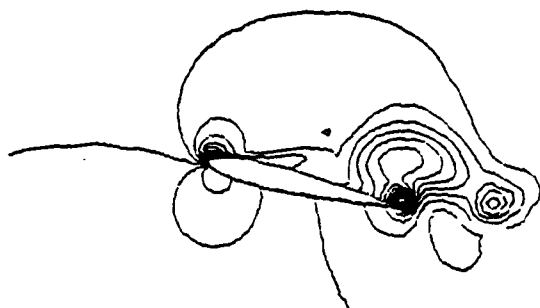
Figure 4-22. Density and Streamlines During an Oscillation Cycle
for NACA0012 at $M_\infty = 0.3$, $f = 21.64\text{Hz}$, $k = 0.05$,
 $Re = 5.4 \times 10^5$, $\alpha_m = 10^\circ$ and $\Delta\alpha = 10^\circ$

Density

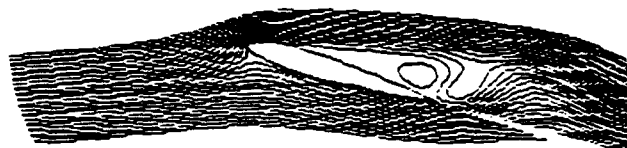
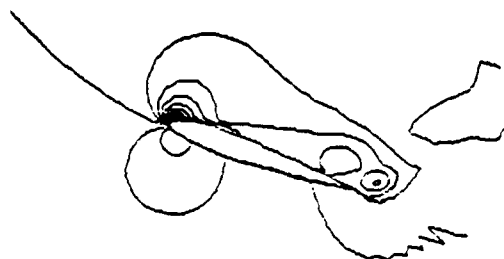
Streamlines



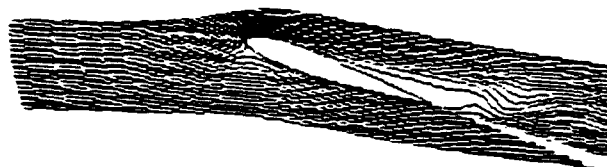
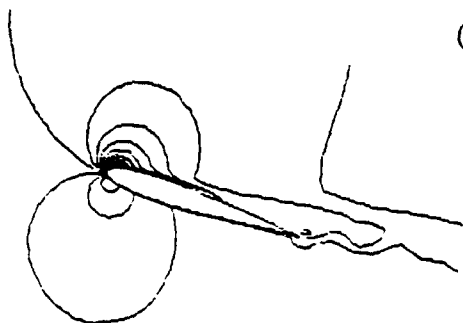
(e) $\alpha = 20^\circ$



(f) $\alpha = 19.8^\circ \downarrow$



(g) $\alpha = 18.4^\circ \downarrow$



(h) $\alpha = 14.7^\circ \downarrow$

Figure 4-22. (Continued)

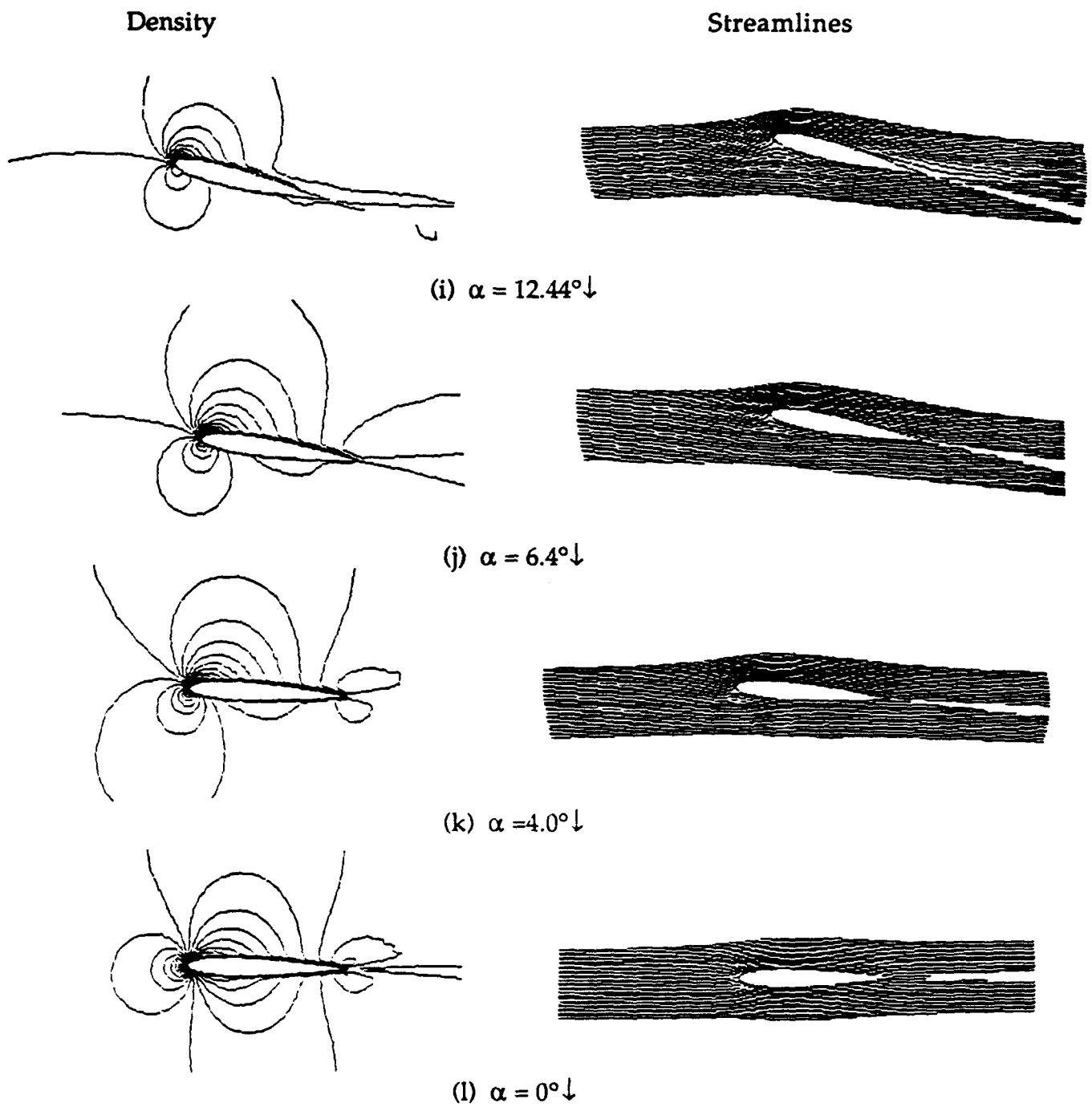


Figure 4-22. (Continued)

Present Simulation

Experiment

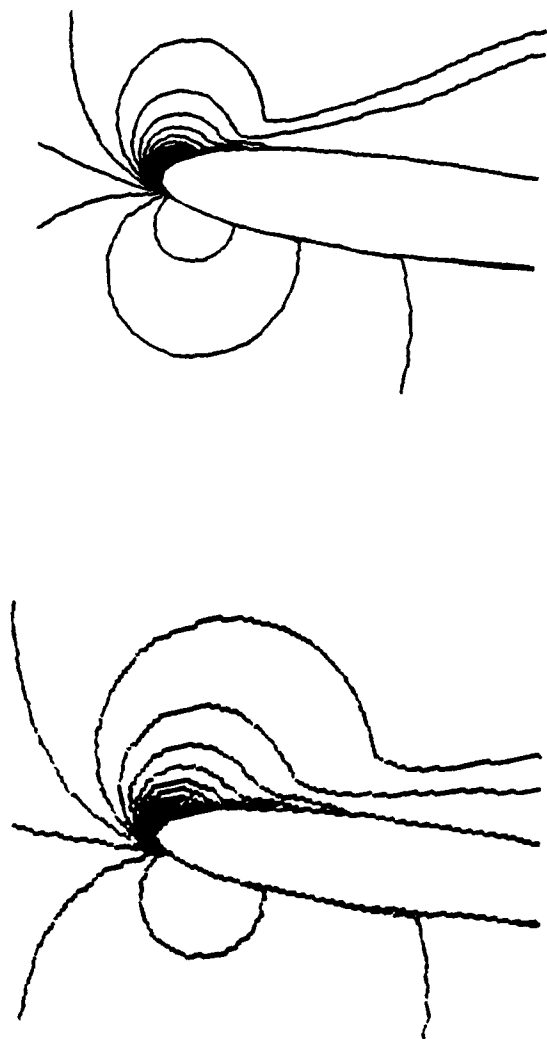
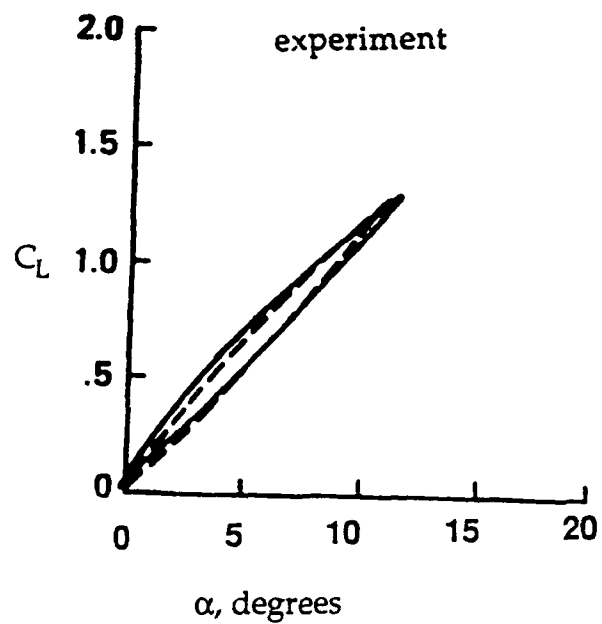
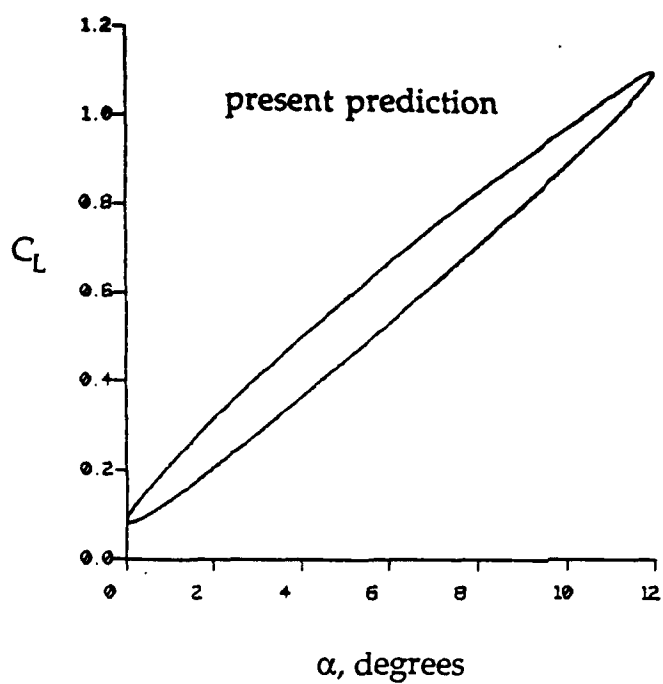
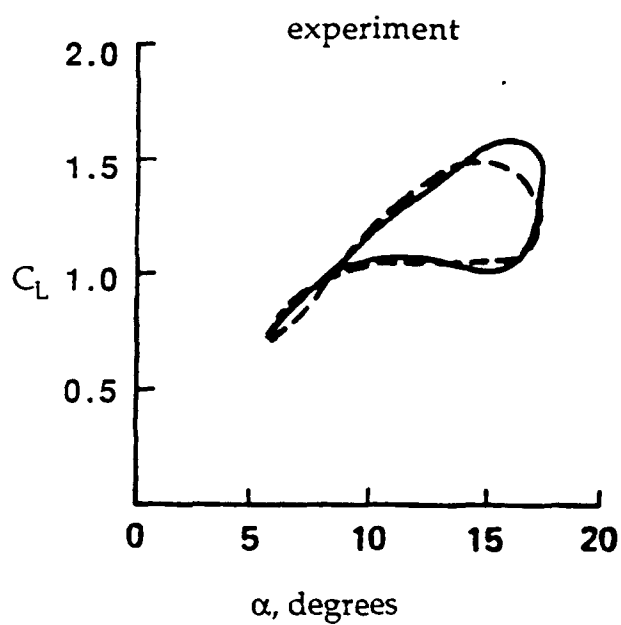
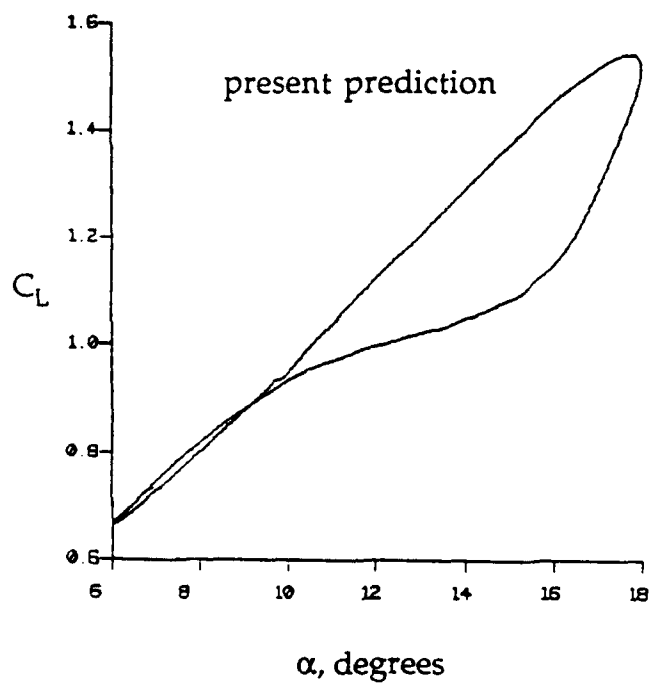


Figure 4-23. Density Contours and Experimental Fringes Around a NACA0012 During the Reattachment Process of an Oscillating Cycle.

$M_\infty=0.3$, $k=0.05$, $Re=5.4 \times 10^5$, $\alpha_m=10^\circ$ and $\Delta\alpha = 10^\circ$



(a) $\alpha = 6 + 6 \sin \omega t$



(b) $\alpha = 12 + 6 \sin \omega t$

Figure 4-24. C_L vs α for $Re=5.4 \times 10^5$, $M_\infty=0.3$, $f=21.64$ Hz, and $k=0.05$

5. THREE-DIMENSIONAL STATIC AND DYNAMIC STALLS ON THE WINGS

In this section, numerical results for flow fields and tip vortex formation are presented for several wing sections. These results are compared with the available experimental data. The different flow conditions and the wing geometries considered are:

1. Rectangular wings in subsonic flow;
2. Static and dynamic stalls on a rectangular wing;
3. Static and dynamic stalls on a forward swept wing;
4. Static and dynamic stalls on a swept back wing; and
5. Static and dynamic stalls on a delta wing.

5.1 Steady Flow over Rectangular Wings

In order to validate the present 3-D code, and the coding of the Baldwin-Lomax turbulence model, a simple non-lifting case is presented first. This case involves a subcritical flow ($M_\infty = 0.5$) about a large-aspect-ratio wing composed of NACA0012 airfoil sections. Because of the large-aspect-ratio characteristic, the symmetry plane solution at both the wing root and wing tip is essentially two-dimensional and should compare favorably with the two-dimensional counterpart. Such a comparison of pressure coefficients from both 2D and 3D, and experimental data of Thibert *et al.*¹¹¹ is shown in Figure 5-1. In the 2D calculation, a grid of 100×40 is used. For 3D, it is $100 \times 40 \times 2$, and symmetric boundary conditions are applied at two lateral planes. The agreement for this easy case is excellent.

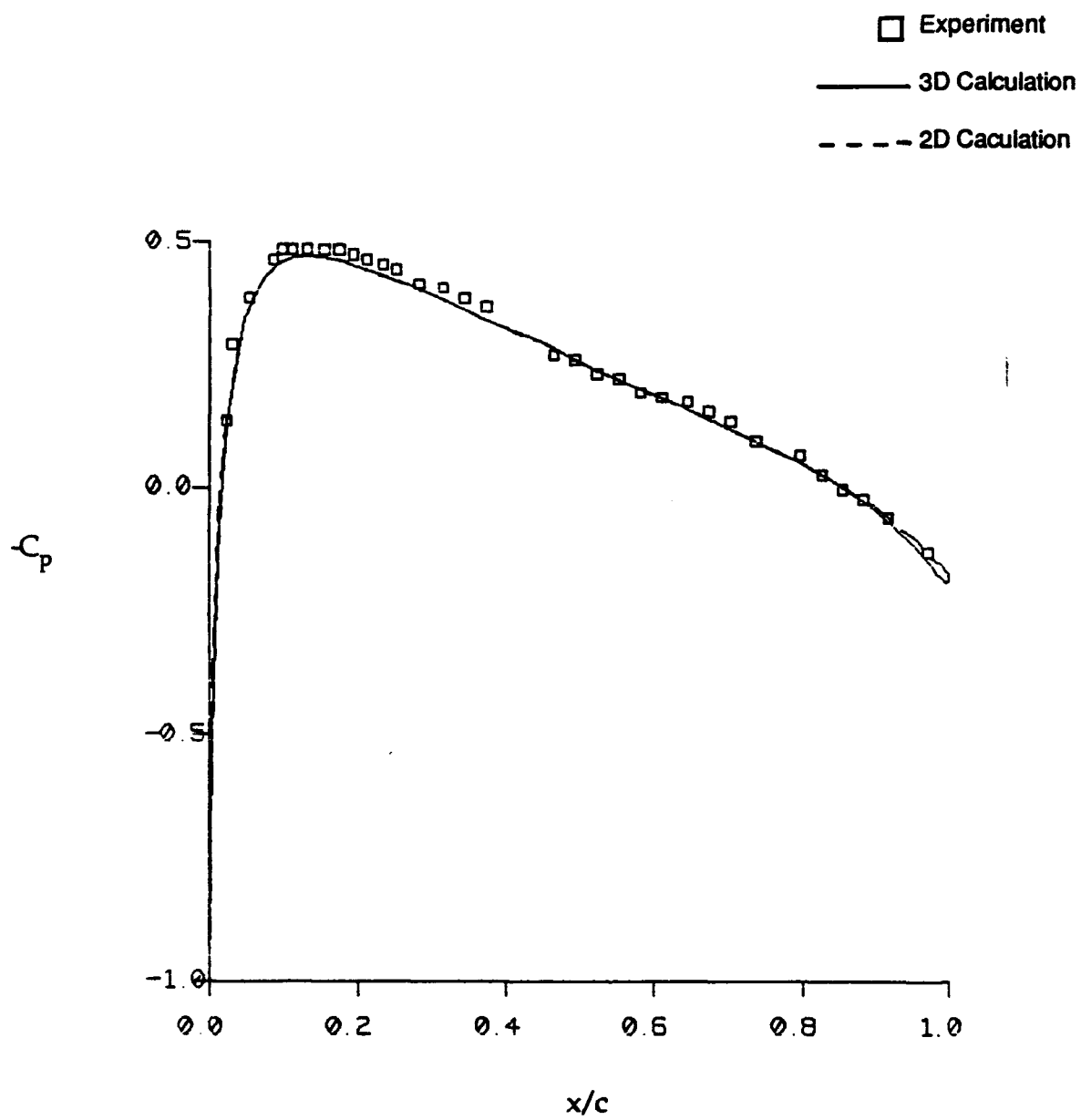


Figure 5-1. Pressure Coefficient Comparisons. NACA0012 Airfoil Section, Large-Aspect-Ratio, ($TR=1.0$, $M_\infty = 0.5$, $\alpha = 0^\circ$, and $Re = 3 \times 10^6$)

The second geometry consists of a rectangular wing with a square tip and a NACA0015 cross-section without twist or taper. The aspect ratio (AR) is 2.5. The incoming free-stream has a Mach number of $M_\infty = 0.16$, Reynolds number of $Re = 2.0 \times 10^6$, and an angle of attack of $\alpha = 11^\circ$.

A single-block O-H grid topology is used for this calculation. There are 84 points in the periodic direction, 16 in the spanwise direction, and 48 in the normal direction. The wing is represented as a solid block containing 4 radial (normal) cells and 14 spanwise cells. The surface grid and grid root wing are shown in Figure 5-2a. Its planform is given in Figure 5-2b. There are four cells extending out the wing tip to capture tip vortex.

The wing root is taken as a symmetric plane to remove the need of refining the grid in order to resolve the boundary layer. As a result, the flow features near the wing root resemble those of two-dimensional flows.

Figure 5-3 shows the computed surface pressure distributions at several spanwise stations compared with the experimental data of Spivey and Moorhouse^{112,113}. The inboard spanwise stations show good agreement with the experiment as evident in Figure 5-3b-d. However, on the suction side at the wing tip, Figure 5-3a, the pressure distribution is not as well predicted. This may be due to the details of the tip-cap, as discussed by Srinivasan *et al.*¹¹⁴

Figure 5-4 shows the surface oil-flow pattern on the upper (suction) and lower (pressure) sides of the wing. This surface oil flow picture is generated by releasing fictitious fluid particles at one grid point above the surface and by restricting these particles to that plane. The three-dimensional effect is evident near the wing tip. Figure 5-5 shows the three-dimensional perspective view of particle traces around

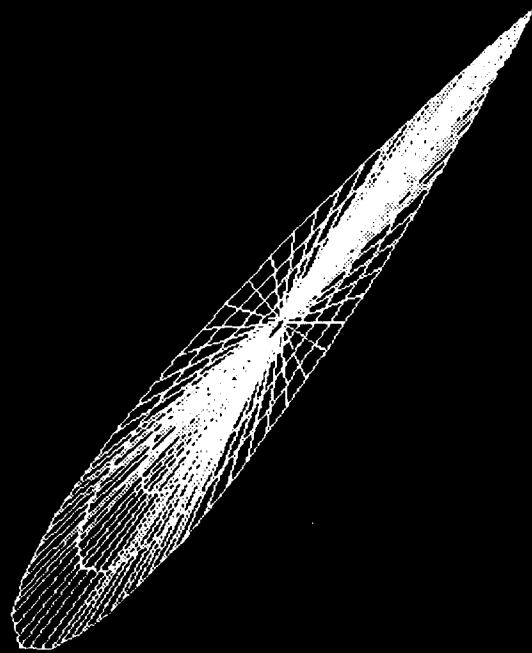
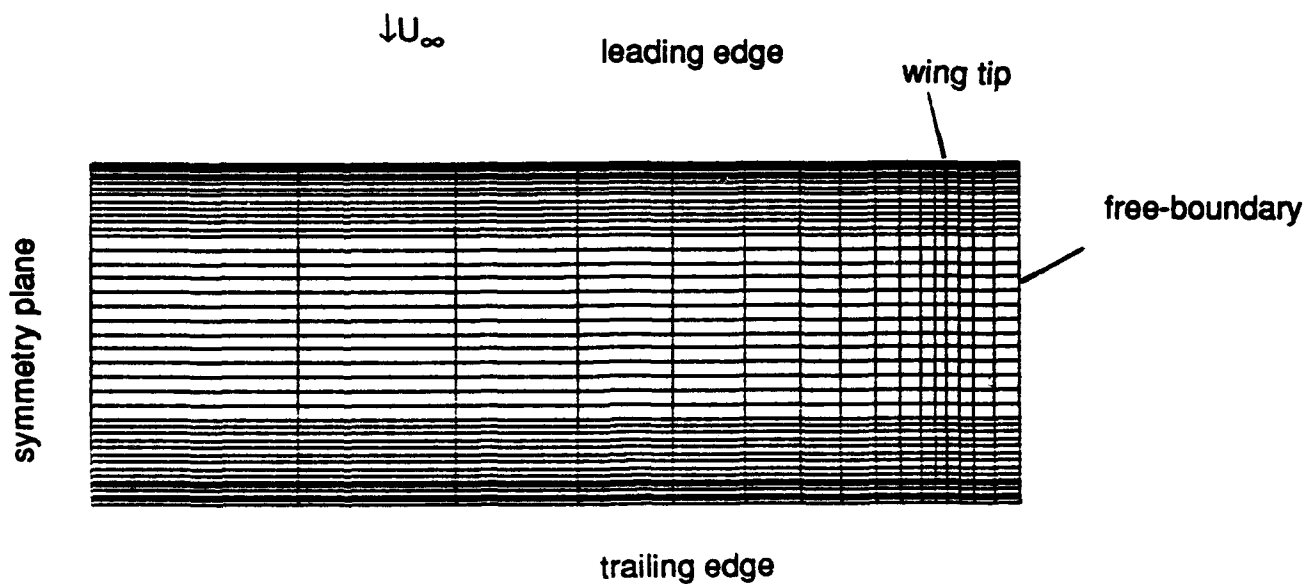


Figure 5-2a. Pictorial View of a $82^{\circ}45'16''$ 3-D Grid
around a Rectangular NACA0015 Wing



(a) Three-Dimensional Perspective View

Figure 5-2. Rectangular NACA0015 Wing and Grid Distribution.
 (a) Three-Dimensional Perspective View; (b) Planform and Surface Grid

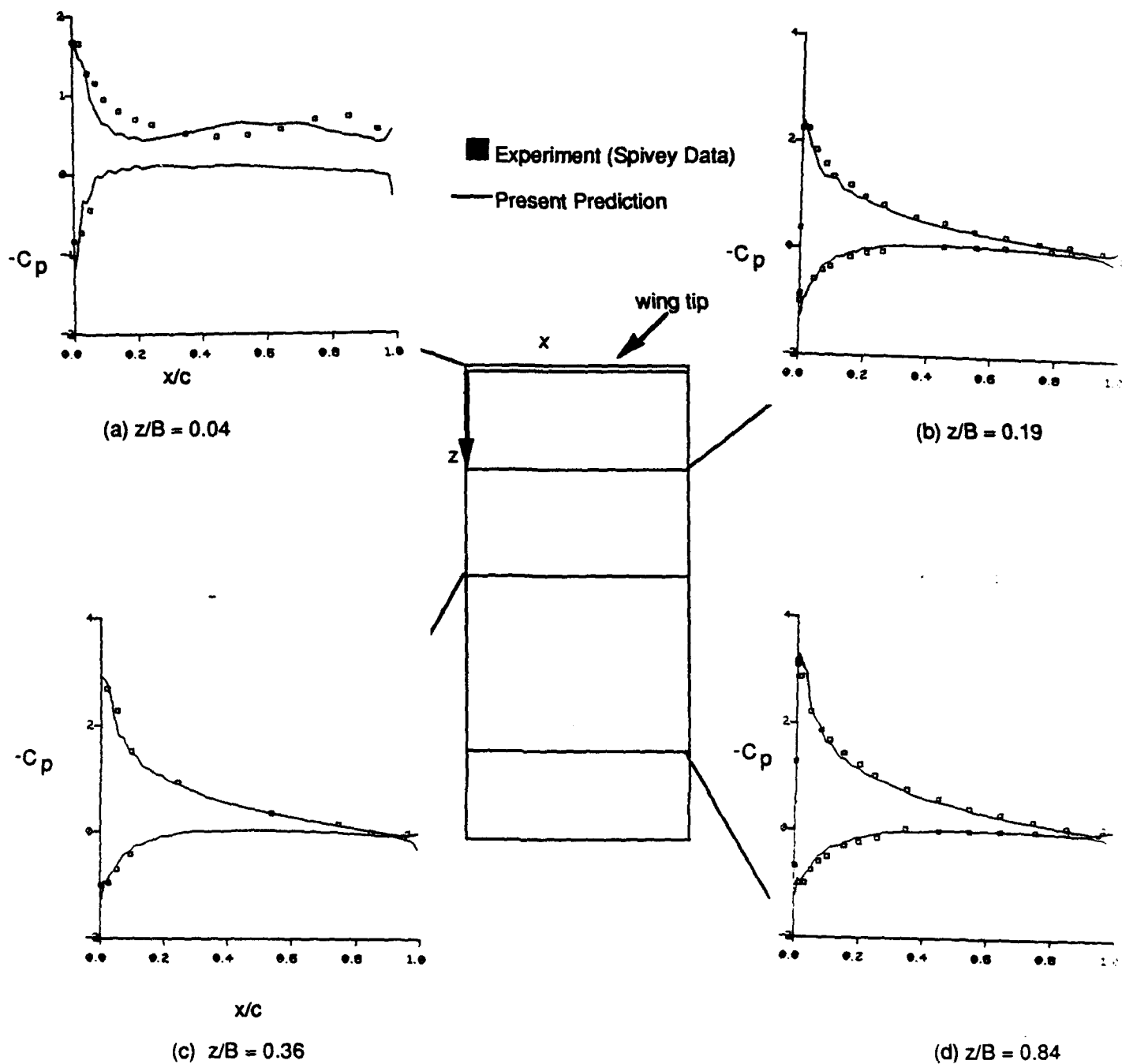


Figure 5-3. Surface Pressure Distributions for Several Spanwise Stations and Comparison with Experimental Data for NACA0015 Rectangular Wing. $M_\infty = 0.16$, $\alpha = 11^\circ$ and $Re = 2 \times 10^6$

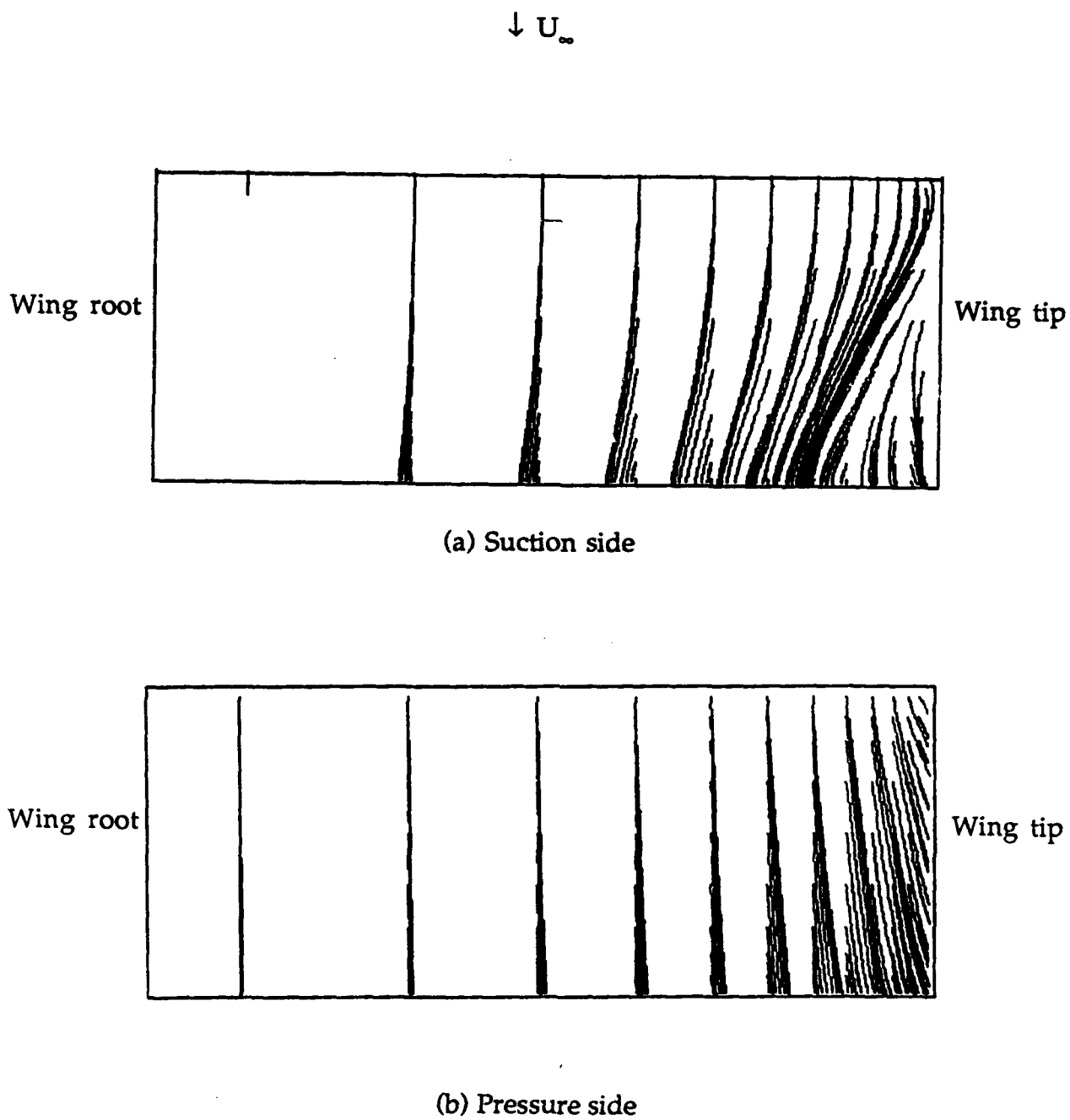
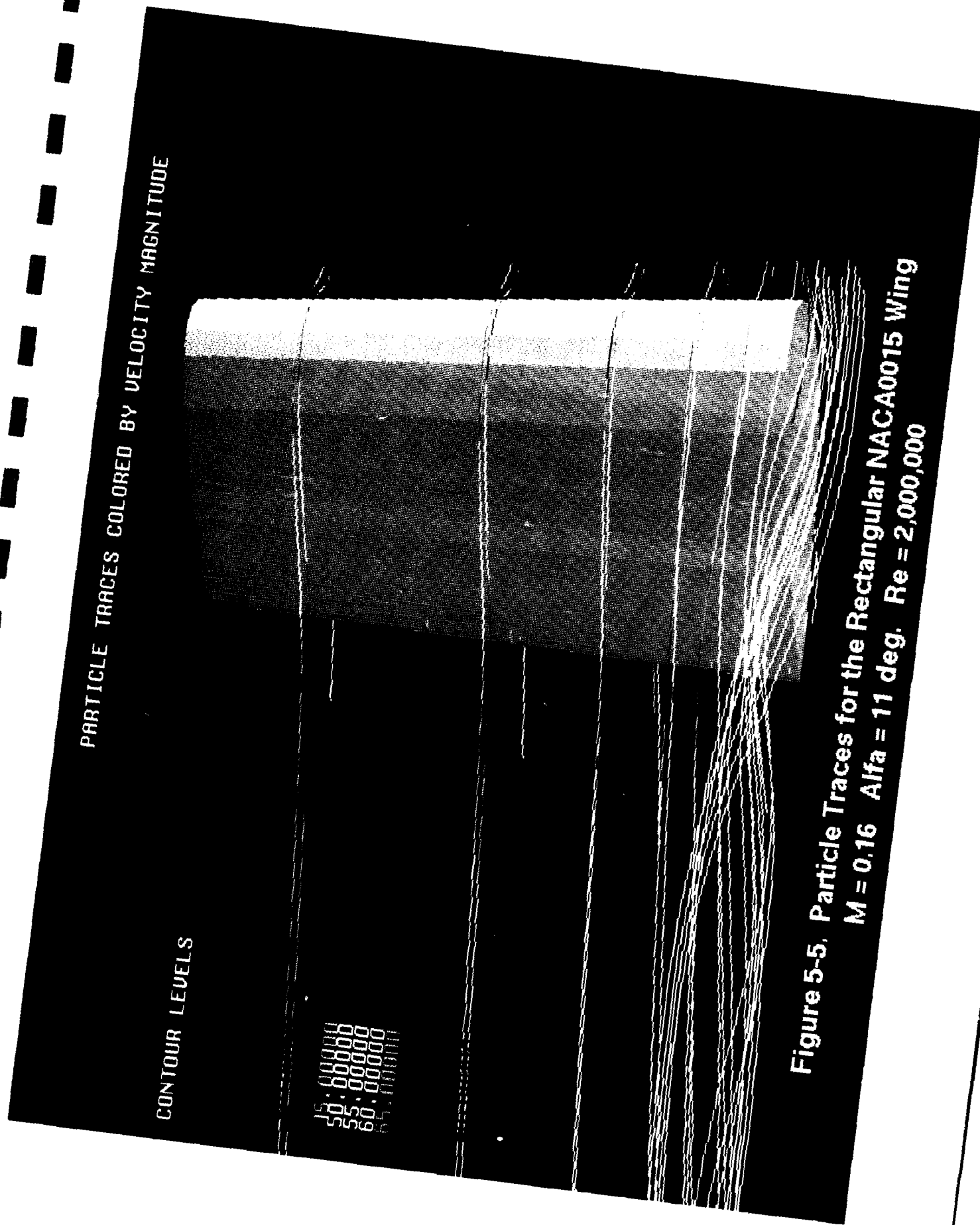


Figure 5-4. Surface Oil-Flow Pattern (Simulated) for the Rectangular NACA0015 Wing. $M_\infty=0.16$, $\alpha=11^\circ$, and $Re=2 \times 10^6$,

(a) Suction side and (b) Pressure side



the wing tip. It is seen that the tip vortex is lifting off from the upper surface of the wing at about the trailing edge position. Figures 5-4 and 5-5 reveal that the particles released in the lower surface of the wing cross over the tip region into the low-pressure region of the upper surface of the wing. These particles mix with the particles released on the upper surface and together they define a tip vortex that is distinct from the rest of the sheet.

Figure 5-6 shows the pressure contours on the wing surface. With the exception being near the tip, the pressure is almost spanwise-independent. It is evident that the tip vortex also causes a pressure gradient at the wing tip.

5.2 Static and Dynamic Stalls on a Rectangular Wing

The operational wings are three-dimensional, and are likely to encounter unsteady flow in three-dimensional conditions. This subsection studies the three-dimensionality of unsteady separated flows on a simple unswept symmetric wing. The experimental visualization of Adler and Luttges⁴⁸, and Ashworth *et al*⁵⁷ will be use as a comparison basis, since only limited experimental data are available.

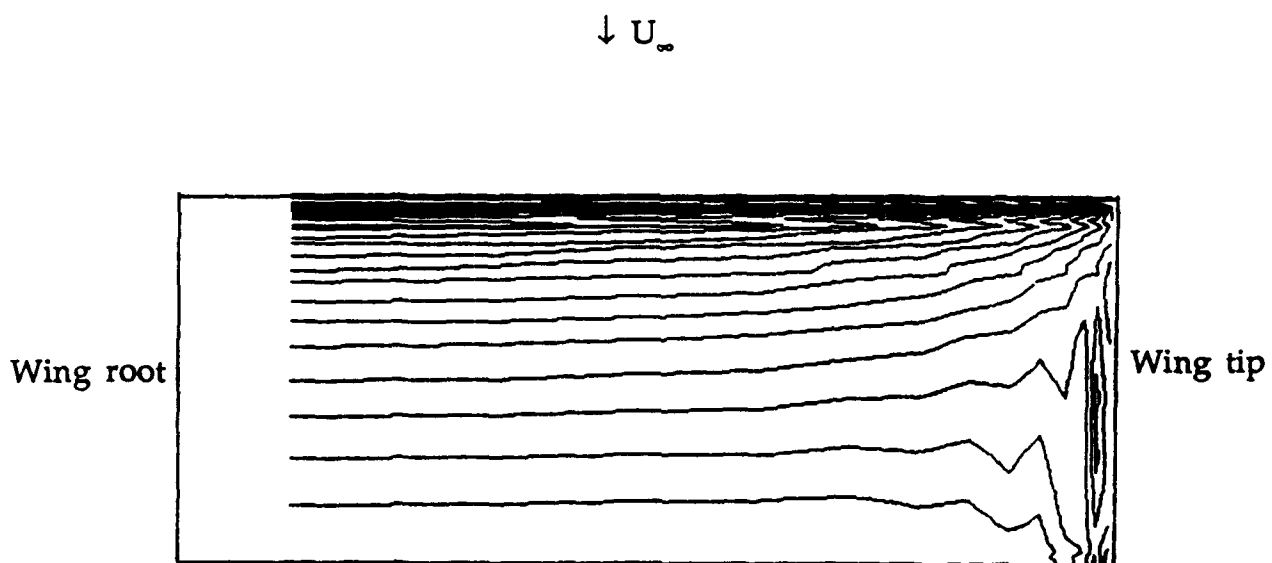
The same flow conditions are used as in the experiment⁴⁸: $Re=42,000$, $M=0.02$, and angle of attack varies harmonically with time:

$$\alpha = \alpha_m + \Delta\alpha \sin(\omega t)$$

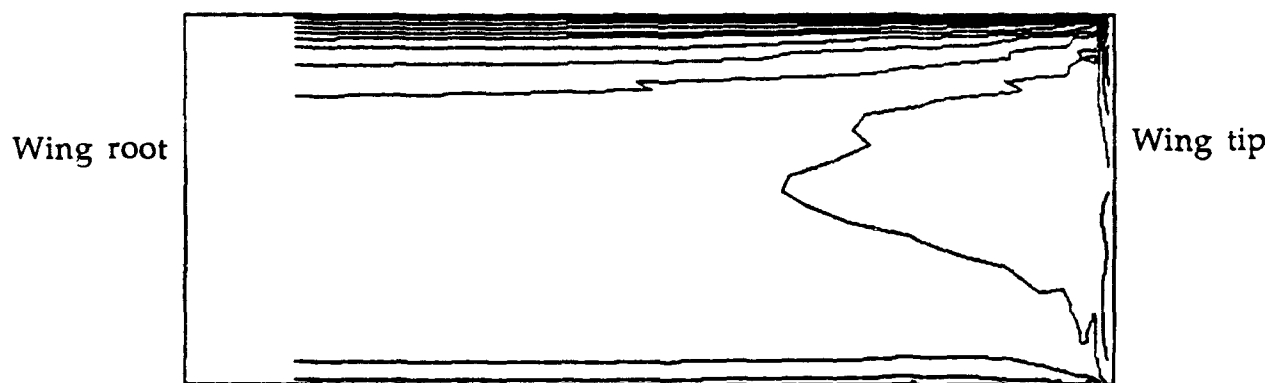
with

(5.1)

$$k = \frac{\omega c}{2U_\infty} = 0.93, \quad \alpha_m = 15^\circ, \quad \Delta\alpha = 10^\circ$$



(a) Suction side



(b) Pressure side

Figure 5-6. Surface Pressure Contours for the Rectangular NACA0015 Wing.

$M_\infty=0.16$, $\alpha=11^\circ$, and $Re=2 \times 10^6$,

(a) Suction side and (b) Pressure side

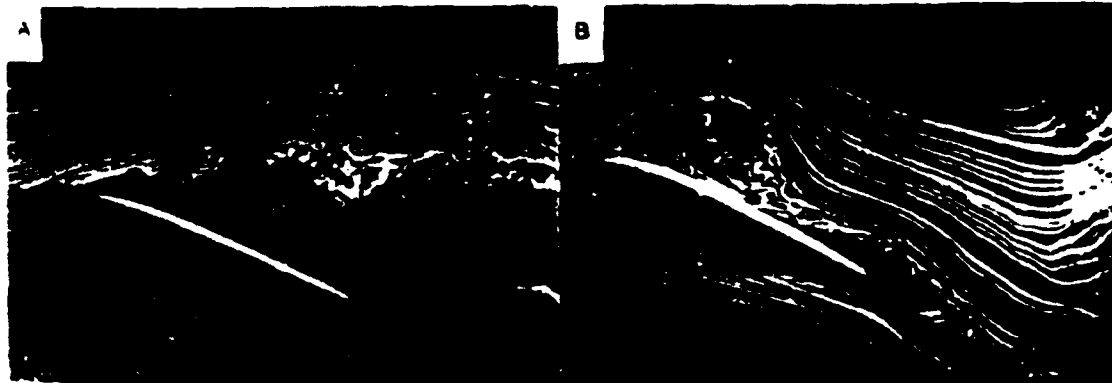
The computational domain contains $58 \times 48 \times 18$ grids in the ξ^1 , ξ^2 and ξ^3 directions, respectively. Again, there are four cells beyond the wing tip to capture the tip vortex. All the computations reported below are carried out with 3rd-order TVD in space and Crank-Nicolson schemes in time.

To gain confidence on the present code, a comparison is made first between the particle traces of the present prediction and experimental smoke visualization of Reference 48, for static stall and dynamic stall at $\alpha = 18^\circ$, as shown in Figure 5-7. For the static stall, the flow is fully separated from the upper surface of the airfoil at this spanwise location ($0.98c$ from the wing tip). This is well predicted by the present theory. The present calculation also predicts several vortices on the upper surface, which is not seen in the experiment. It should be noted that these vortices appear in the figure only if particles are released in that region. Experimental visualizations are obtained by introducing smoke traces upstream to the airfoil. The convected smoke particles may not travel through the upper wing surface so that the details of the above recirculating flows may not be detected.

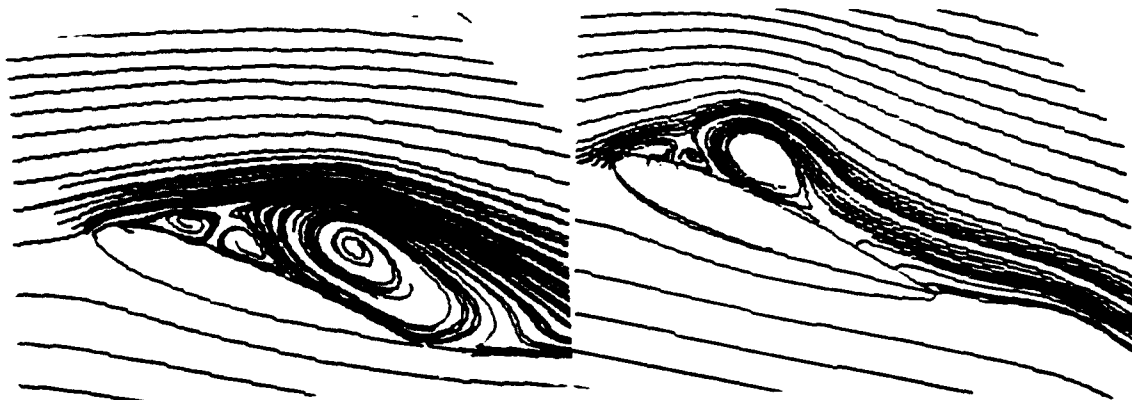
Under unsteady conditions (dynamic stall in Figure 5-7) there is a leading edge bubble (or dynamic stall vortex) on the upper surface in the experiment. The agreement of the present theory with experimental visualization is remarkable. To gain a three-dimensional understanding of the flow field, oil-flow patterns on the upper wing surface and particle traces at different spanwise locations for both static and dynamic stalls are shown in Figure 5-8 and Figure 5-9, respectively. From the oil-flow pattern of both the figures, a transition from flows dominated by the wing tip vortex to those dominated by the leading edge vortex is observed. The flow beyond $1c$ inboard is essentially two-dimensional, which is characterized by the leading edge vortex, secondary vortex and territorial vortices. Near the wing tip, however, the secondary and territorial vortices are suppressed by the tip vortex,

A
Static Stall
 $\alpha = 18^\circ$

B
Dynamic Stall
 $\alpha = 18^\circ \downarrow$
 $\alpha_m = 15^\circ, \Delta\alpha = 10^\circ, k = 0.93$



(a) Experimental Visualization



(b) Present Prediction (Particle Traces)

Figure 5-7. Static and Dynamic Stalls on a Rectangular Wing of a NACA0015
at 0.98c Inboard. $Re=42,000$ and $M=0.02$.

(a) Experimental Visualization (b) Particle Traces of the Present Prediction

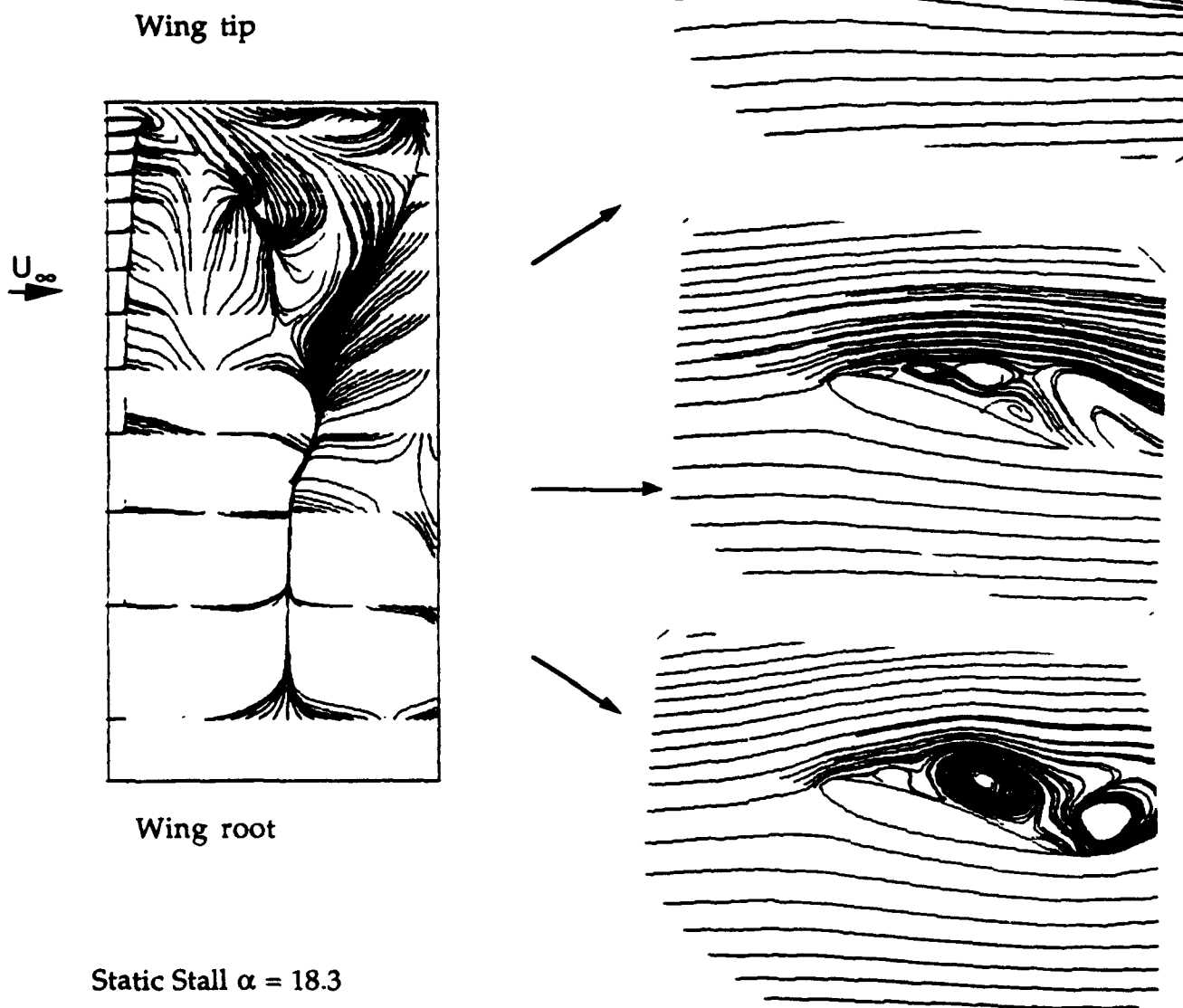


Figure 5-8. Particle Traces on the Upper Surface of NACA0015 Rectangular Wing and at Several Spanwise Locations for Static Stall.
 $Re=42,000$, $M=0.02$ and $\alpha=18.3^\circ$

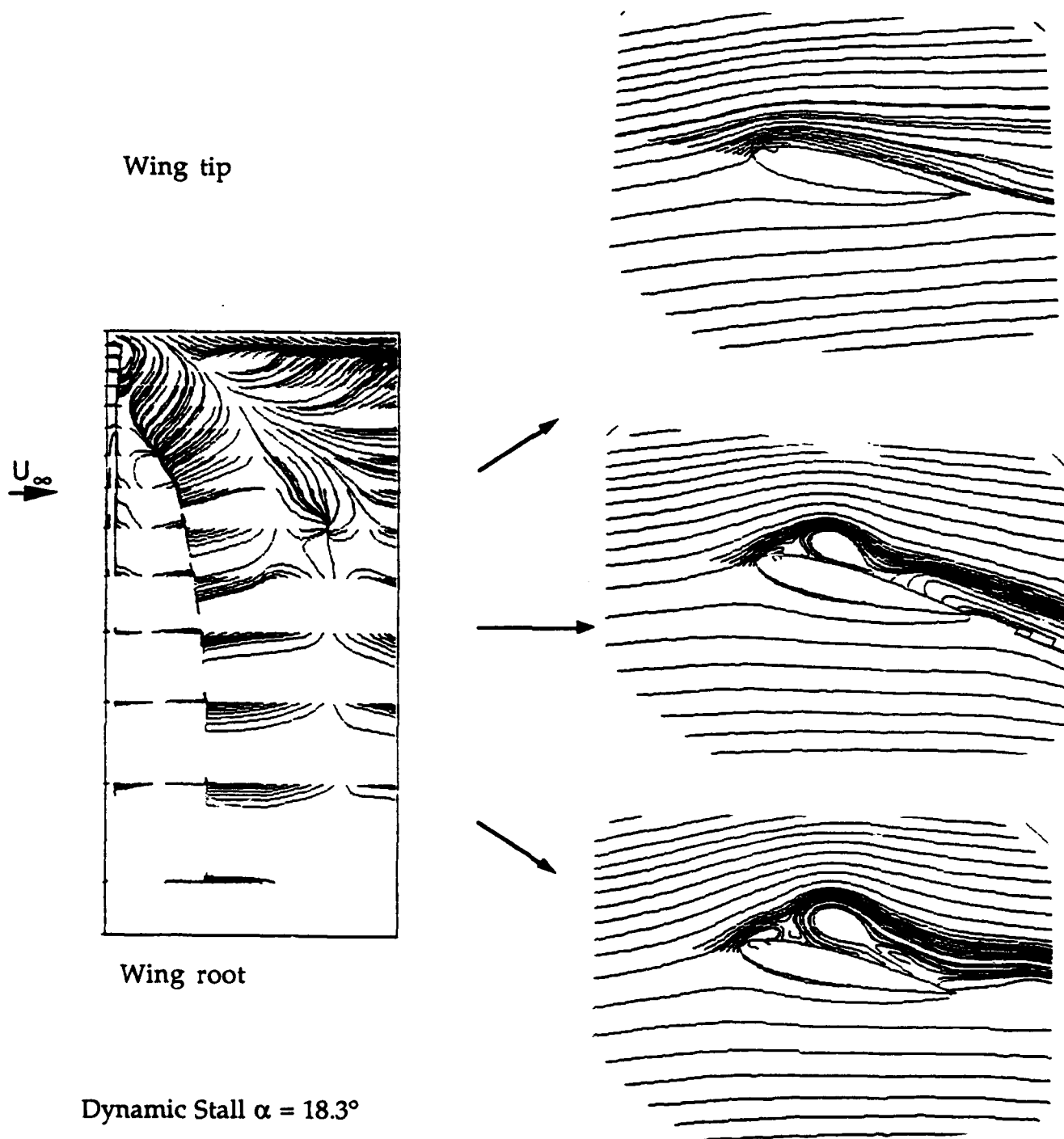


Figure 5-9. Particle Traces on the Upper Surface of a NACA0015 Rectangular Wing and at Several Spanwise Locations During Dynamic Stall.

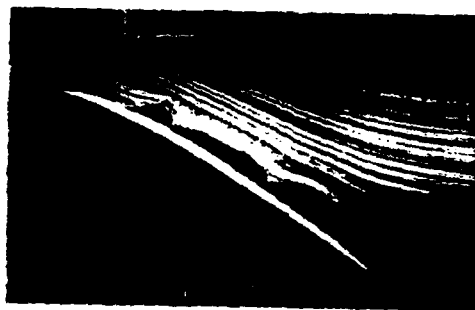
$Re=42,000$, $M_\infty=0.02$ and $\alpha=18.3^\circ$ Downstroke (\downarrow).

such that only the leading edge separation is visible from the particle traces. The size of the secondary vortex grows from the wing tip toward the wing root.

To illustrate the size and convective characteristics of the leading edge vortex, Figure 5-10 shows the particle traces at 0.67c inbound location, from the present computation ($k=0.93$). The experimental visualization⁵⁷ at $k=1.0$ are also shown for the comparison. At the maximum angle of attack, $\alpha=25^\circ$, the shear layer vorticity at the leading edge is coalescing into distinct vortex patterns. With decreasing α , (Figure 5-10b, $\alpha=18^\circ$; Figure 5-10c, $\alpha=5^\circ$), the leading edge vortex convects toward the trailing edge by the free stream flow. With the continuation of pitching motion (Figure 5-10d,e) the leading edge vortex is shed from the trailing edge to the wake and the flow reattaches to the surface of the wing.

The flow patterns at an even further inboard location of 1.5c are given in Figure 5-11 for the present computation. The leading edge separated flow at $\alpha=23.3^\circ$ (Figure 5-11j) breaks up into two bubbles (Figure 5-11a) convecting downstream along the upper surface of the wing. At $\alpha=21.0^\circ$ downstroke, (Figure 5-11b), the shear layer is separated from the leading edge. As the angle of attack decreases, the shear layer starts moving towards the airfoil upper surface (Figures 5-11b and 5-11c). The reattachment occurs when the static stall angle is reached (Figure 5-11d), and a bubble is formed. The shear layer further separates downstream. Meanwhile, the leading edge attachment progresses and the bubble grows in the size and convects to the trailing edge during the upstroke portion of the cycle (Figure 5-11f-j).

(a) $\alpha = 25^\circ$



(b) $\alpha = 18.1^\circ \downarrow$



(c) $\alpha = 5.0^\circ \downarrow$



(d) $\alpha = 11.0^\circ \uparrow$



(e) $\alpha = 23.1^\circ \uparrow$

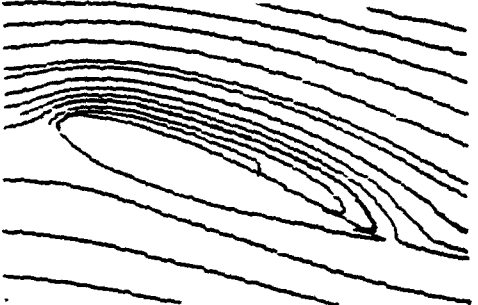
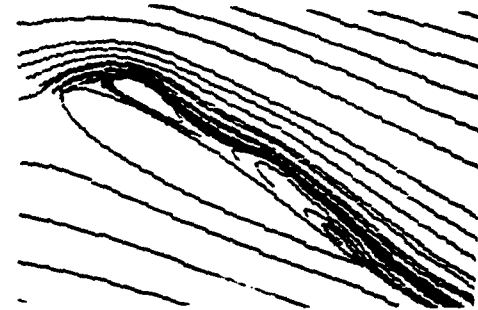


Figure 5-10. Flow Patterns over One Pitching Cycle at $0.67c$ Inboard.

$Re = 1.5 \times 10^5$ ($Re = 1.0 \times 10^5$ experimental), $K = 0.93$ (computation)

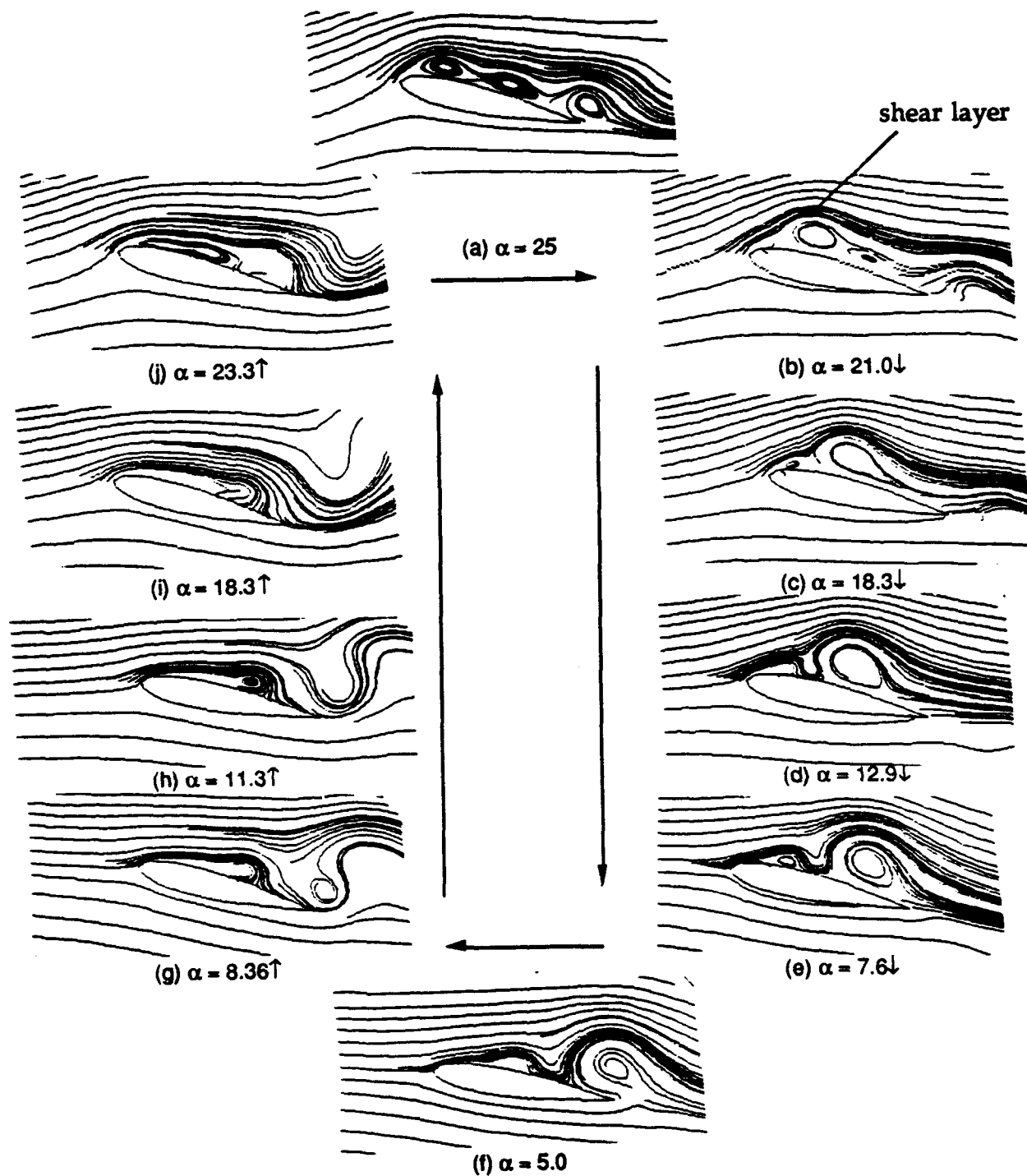
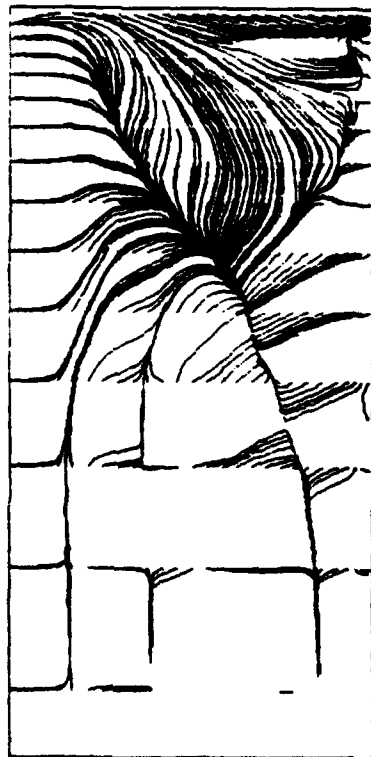


Figure 5-11. Flow Patterns over One Pitching Cycle at 1.5c Inboard,
3D Rectangular Wing, $Re = 42,000$, $k=0.93$

The difference of flow patterns between the upstroke and downstroke for the bubble development are due to the hysteresis effects that are always present in these unsteady flows. The effect of a tip vortex can be appreciated by comparing Figures 5-10 and 5-11 in the upstroke of the cycle. Near the wing tip (Figure 5-10) the flow is attached during upstroke instead of separated for the location far inboard (Figure 5-11).

Figure 5-12 shows the flow patterns and pressure contours on the upper surface over a pitching cycle. The movement of the separated flow region is clearly seen from the oil-flow pattern, while separation and reattachment are always accompanied by high pressure gradients.

Figure 5-13 shows the lift coefficient versus the angle of attack in one oscillatory cycle. The 2D counterpart is also given. It is interesting to note that the lift curve slope for the 3D wing is reduced from the 2D value. This characteristic has also been found in the experiments^{47,49}. It is noted that dynamic stall is delayed and the amplitude of the lift drop is reduced in the 3D wing in comparison to that in 2D. This delay in dynamic stall is attributed to lower effective angles of attack caused by proximity to the wing tip. During the downstroke, the suction pressure peak is usually associated with the stall vortex. This vortex interacts with the tip vortex and is suppressed near the wing tip. As a result, the pressure on the upper wing surface is relatively high compared to the 2D counterpart (see Figure 5-12). This causes a lower lift during the downstroke. The oil flow visualization in Figure 5-12 indicates that the tip vortex rolls up over the wing in a roughly 30° triangle beginning at the tip leading edge.

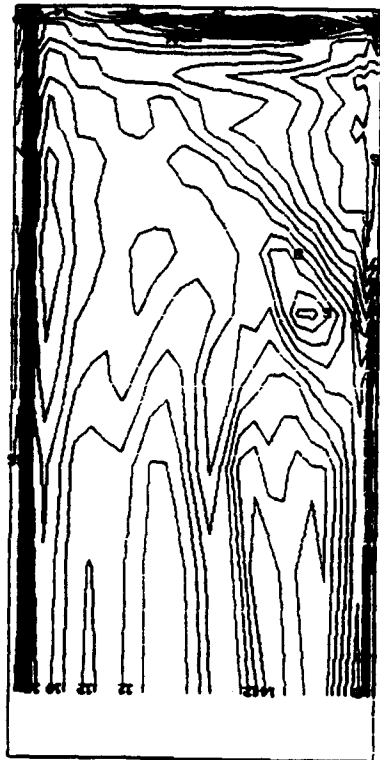


$\alpha = 5.0^\circ \uparrow$



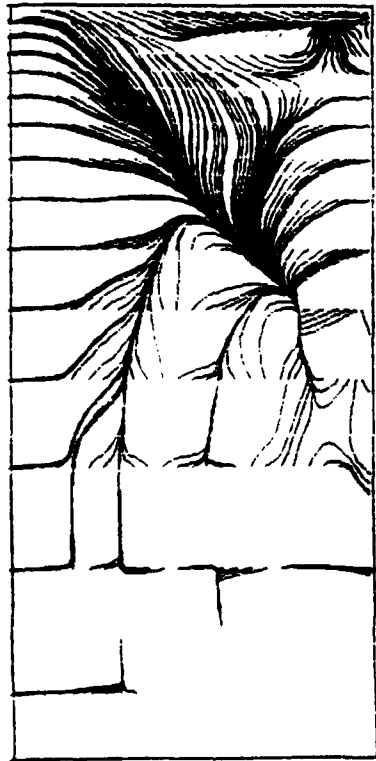
$\alpha = 8.3^\circ \uparrow$

oil flow patterns

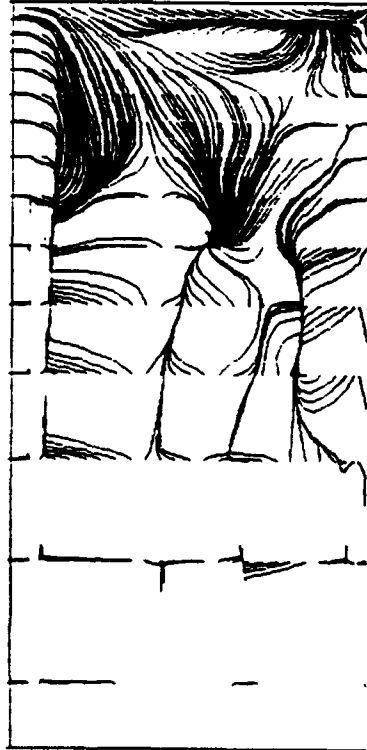


pressure contours

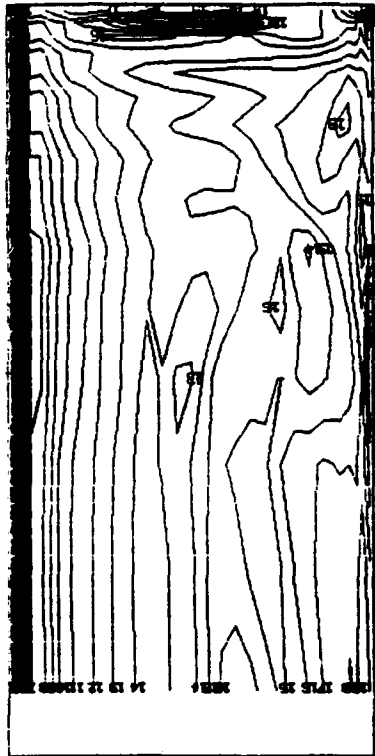
Figure 5-12. Oil Flow Patterns (Simulated) and Pressure Contours on the Upper Surface of a Rectangular NACA0015 Wing over One Pitching Cycle.
 $Re=42,000$, $k=0.93$, $\alpha_m=15^\circ$ and $\Delta\alpha = 10^\circ$



$\alpha = 11.3^\circ$



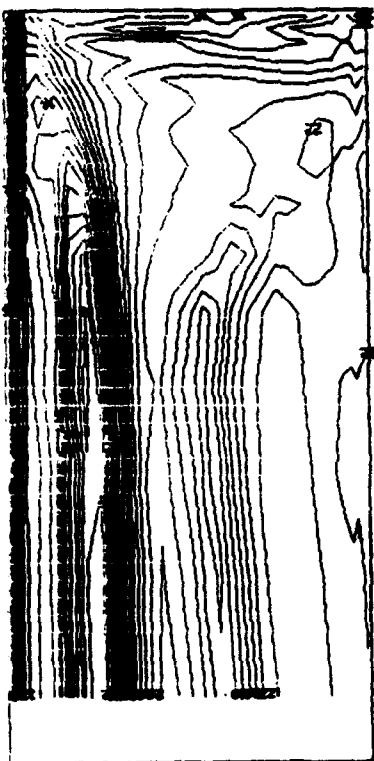
$\alpha = 18.4^\circ$



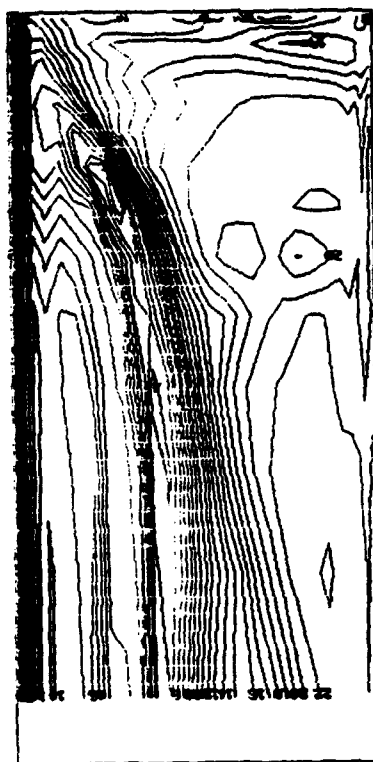
oil flow patterns

pressure contours

Figure 5-12. (Continued)

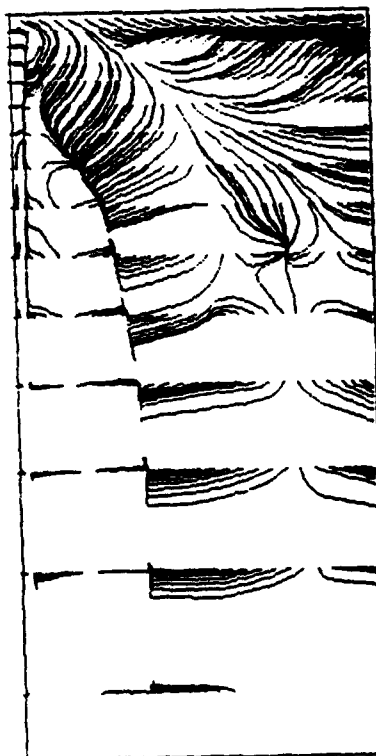


$\alpha = 25^\circ$



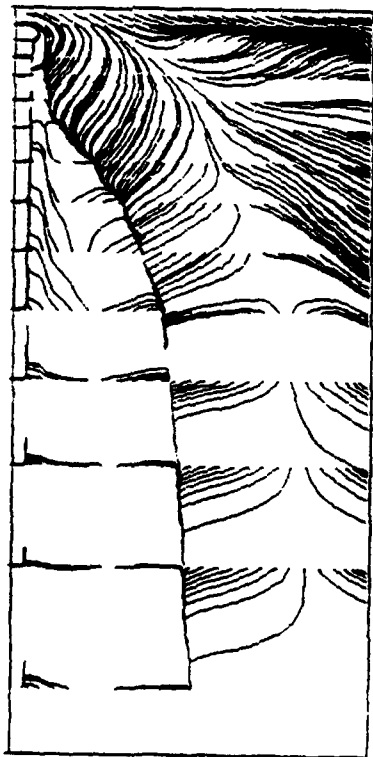
$\alpha = 18.40^\circ$

pressure contours

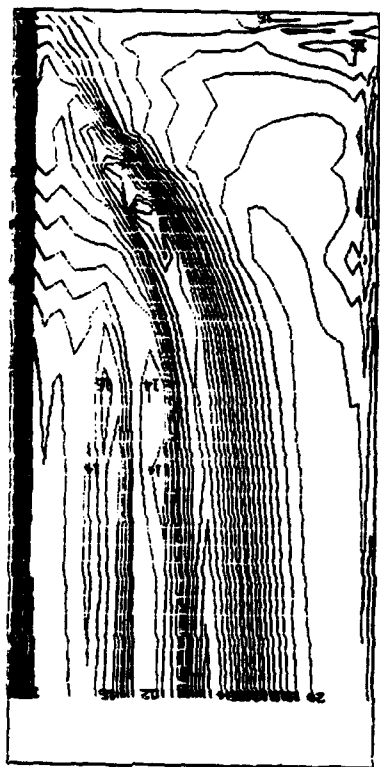


oil flow patterns

Figure 5-12. (Continued)



$\alpha = 12.9 \downarrow$



$\alpha = 7.6 \downarrow$



pressure contours

oil flow patterns

Figure 5-12. (Continued)

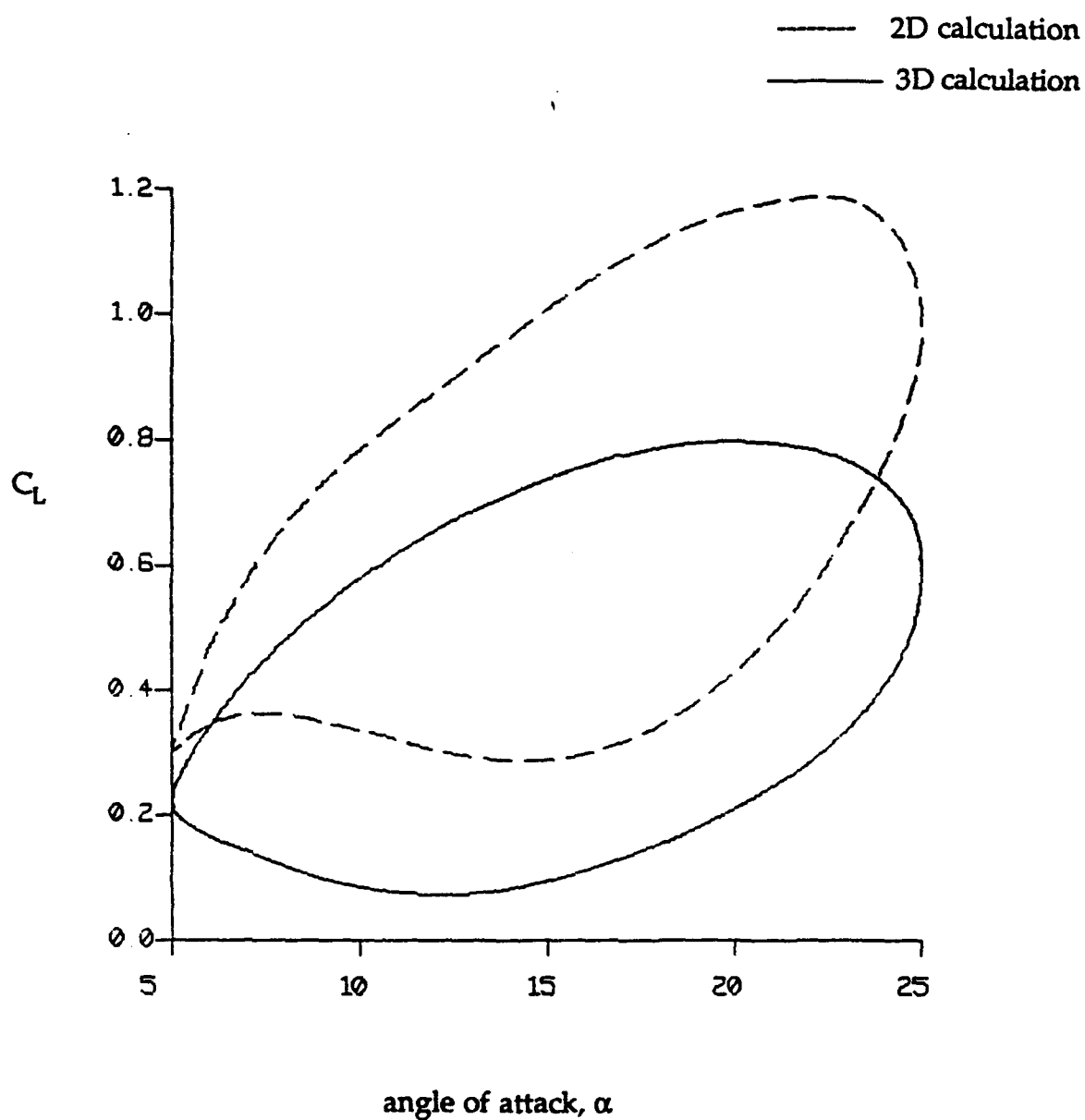


Figure 5-13. Lift Coefficient versus Angle of Attack for a Rectangular NACA0015 Wing Under Oscillating Motion. $Re = 42,000$, $M = 0.02$ and $k = 0.93$

5.3 Static and Dynamic Stalls on a Forward Swept Wing

Forward swept wings are found to perform well at high Mach numbers and have aerodynamic advantages at very low airspeeds (laminar flow)^{115,116}. They are much better suited as laminar flow wings, due to smaller effective sweep angles compared to a corresponding backward swept wing. Thus, the laminar boundary of a comparable forward swept wing is more stable against attachment line transition and crossflow instability. This section focuses on the three-dimensional characteristics of unsteady flows produced about a swept forward wing under static conditions and dynamic pitching conditions.

The flow and wing geometry are such that they simulate those in the experiment of Ashworth *et al*⁵⁶. The wing has a NACA0015 cross-section, and 30° forward sweep. The tape ratio is 1.0 and the aspect ratio is 2.0. The boundary conditions and computational grid on the wing surface are shown in Figure 5-14. The Reynolds number is $Re=40,000$ with $M=0.02$. An O-H grid topology is applied to generate the grid around the wing, as shown in Figure 5-2. There are 58 grids in the circumferential, 44 in the radial, and 18 in the spanwise directions. Four cells are located beyond the wing tip to capture the tip vortex (see Figure 5-14).

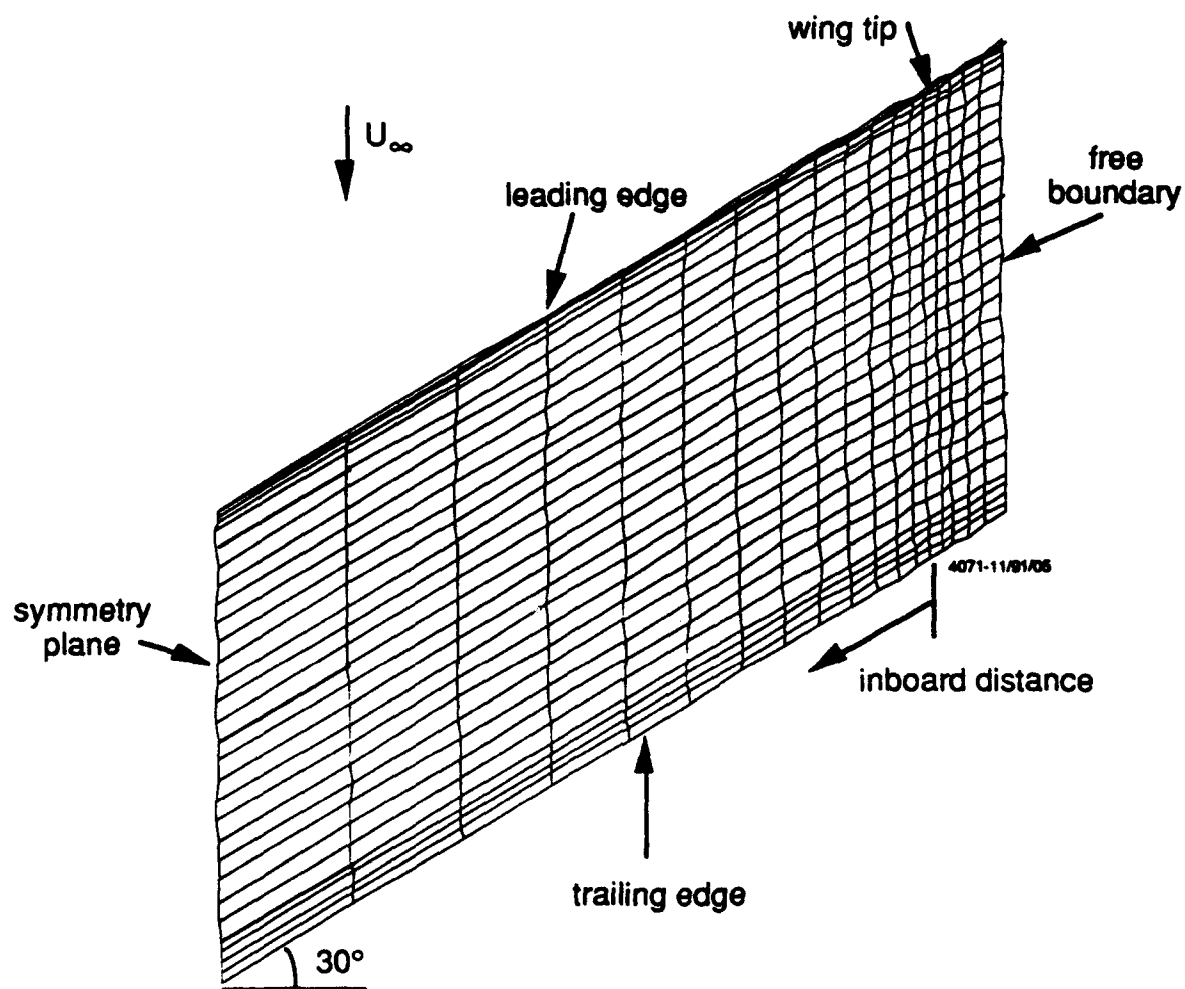


Figure 5-14. Top View of the Computational Grid and Boundary Conditions on a 30° Forward Swept Wing

5.3.1 Computations for Static Conditions

Figures 5-15 to 5-17 show the comparisons of flow visualizations⁵⁶ with the present 3D static calculations. The Reynolds number is 40,000, and the angles of attack are 3°, 15° and 27° for Figures 5-15, 5-16, and 5-17, respectively. At an angle of attack of 3°, the flow is fully attached, and there is only a slight difference in the flow characteristics at 0.58c inboard and at 1.15c inboard (Figure 5-15). At an angle of attack of 15°, leading edge separation appears in the suction side of the wing. The size of the separated flow varies with spanwise locations. For example, at 0.58c inboard (Figure 5-16a), the flow is reattached, while no reattachment is visible at 1.15c inboard (Figure 5-16b). At even higher angles of attack, ($\alpha = 27^\circ$) the flow is totally separated from the upper surface (Figure 5-17). It can be seen that the present computations predict well the experimental visualizations.

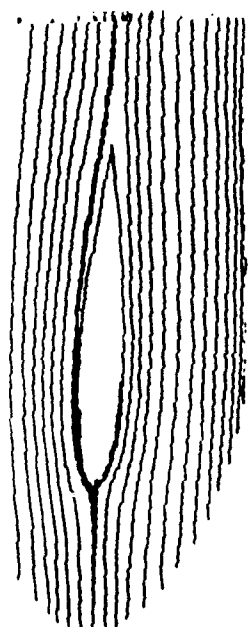
To appreciate the three-dimensionality of the present simulation, particle traces are shown in Figures 5-18 and 5-19 for $\alpha=27^\circ$ with top and side views. The top view (Figure 5-18) clearly displays the effect of tip vortex and three-dimensionality of separated flow on the suction side of the wing. From the side view (Figure 5-19) one can see the growth of the separated flow region from the wing tip toward the wing root.

Given in Figure 5-20 are the oil-flow pattern on the upper surface of the wing. There is a focus point at 1.5c inboard. In comparison to Figure 5-18 of the three-dimensional particle trace, we see that the flow particles released near the wing tip are sucked to the wing's upper surface, and take off at the focal point to form a helical flow pattern.

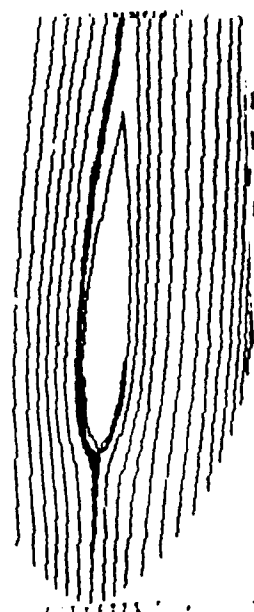
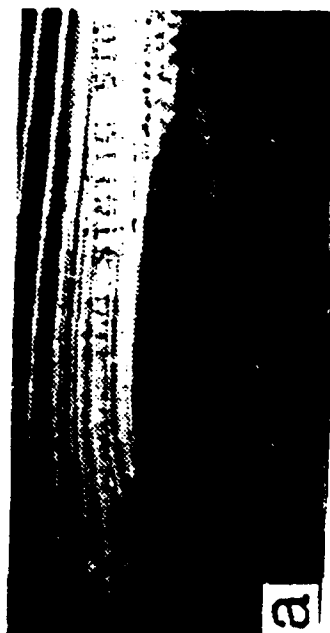
Experiment Visualizations



Particle Traces



(a) at 0.58c inboard, $\alpha = 3^\circ$



(b) at 1.15c inboard, $\alpha = 3^\circ$

Pressure Contours

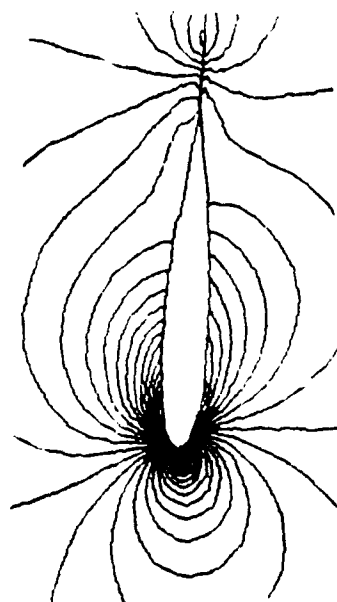
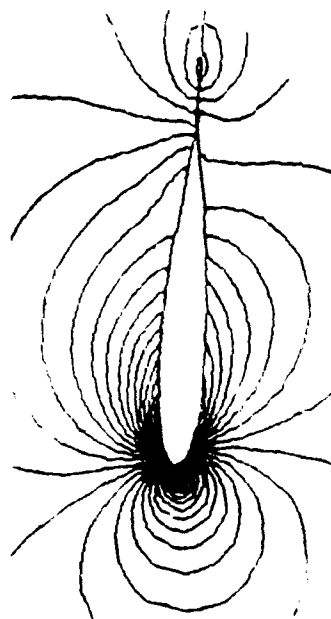
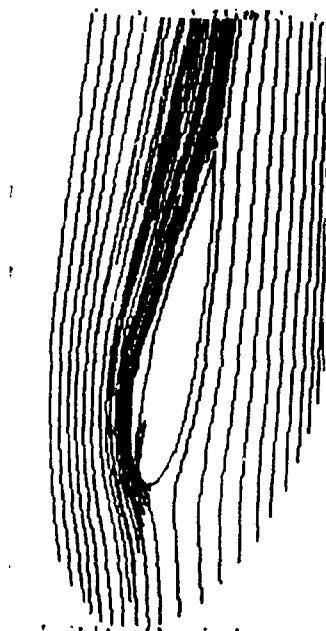
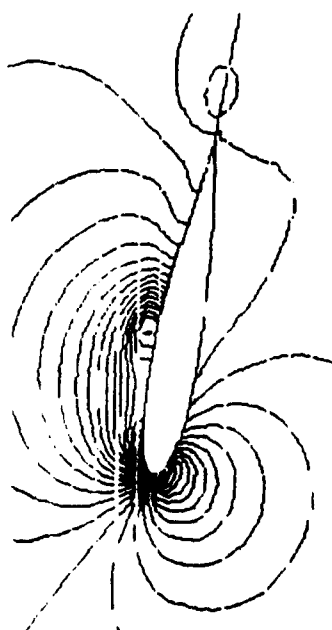


Figure 5-15. Present Calculations and Flow Visualizations for a 3D Forward Swept Wing at $\alpha = 3^\circ$, $Re = 40,000$

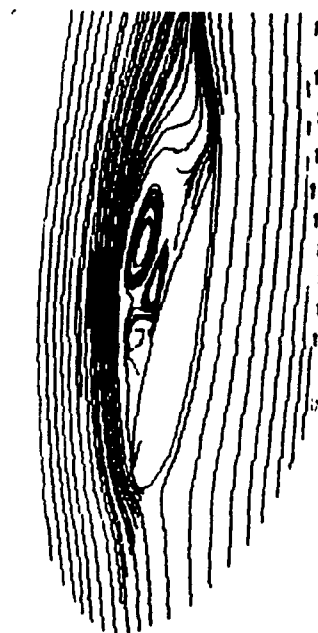
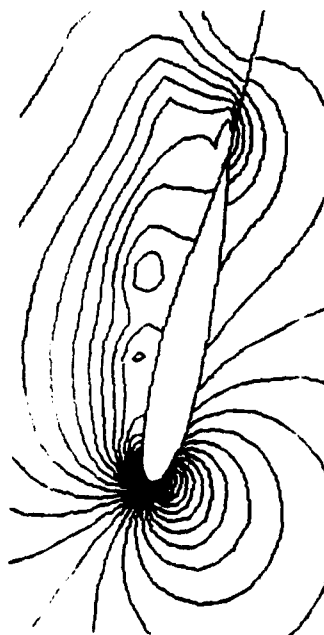
Pressure Contours

Particle Traces

Experiment Visualizations



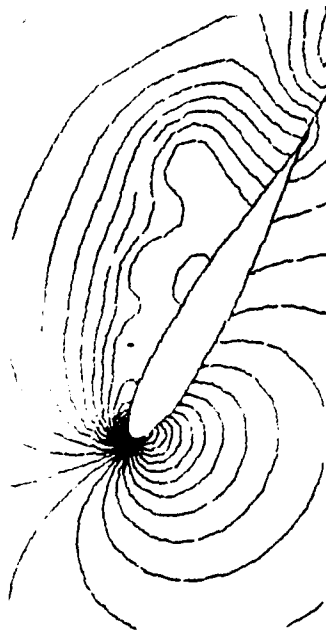
(a) at 0.58c inboard, $\alpha = 15^\circ$



(b) at 1.15c inboard, $\alpha = 15^\circ$

Figure 5-16. Present Calculations and Flow Visualizations for a 3D Forward Swept Wing at $\alpha = 15^\circ$, $Re = 40,000$

Pressure Contours

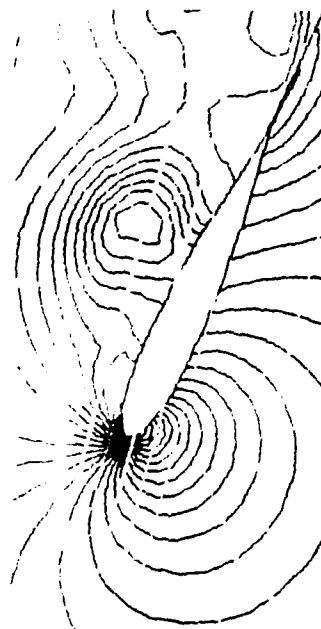


Particle Traces



(a) at 0.58c inboard, $\alpha = 27^\circ$

108



(b) at 1.15c inboard, $\alpha = 27^\circ$

Experiment Visualizations



Figure 5-17. Present Calculations and Flow Visualizations for a 3D Forward Swept Wing
at $\alpha = 27^\circ$, $Re = 40,000$

Particle Traces Colored by Velocity Magnitude

CONTOUR LEVELS

1.50000
5.00000
5.50000
6.00000

Top View



Figure 5-18. Particle Traces on Static 3-D 30 deg. Forward Swept NACA0015 Wing
Re = 40,000 M = 0.02 Alfa = 27 deg.

Particle Traces Colored by Velocity Magnitude

CONTOUR LEVELS

4.50000
5.00000
5.50000
6.00000

Side View

Figure 5-19. Separation on Static 3-D 30 deg. Forward Swept NACA0015 Wing
Re = 40,000 M = 0.02 Alfa = 27 deg.

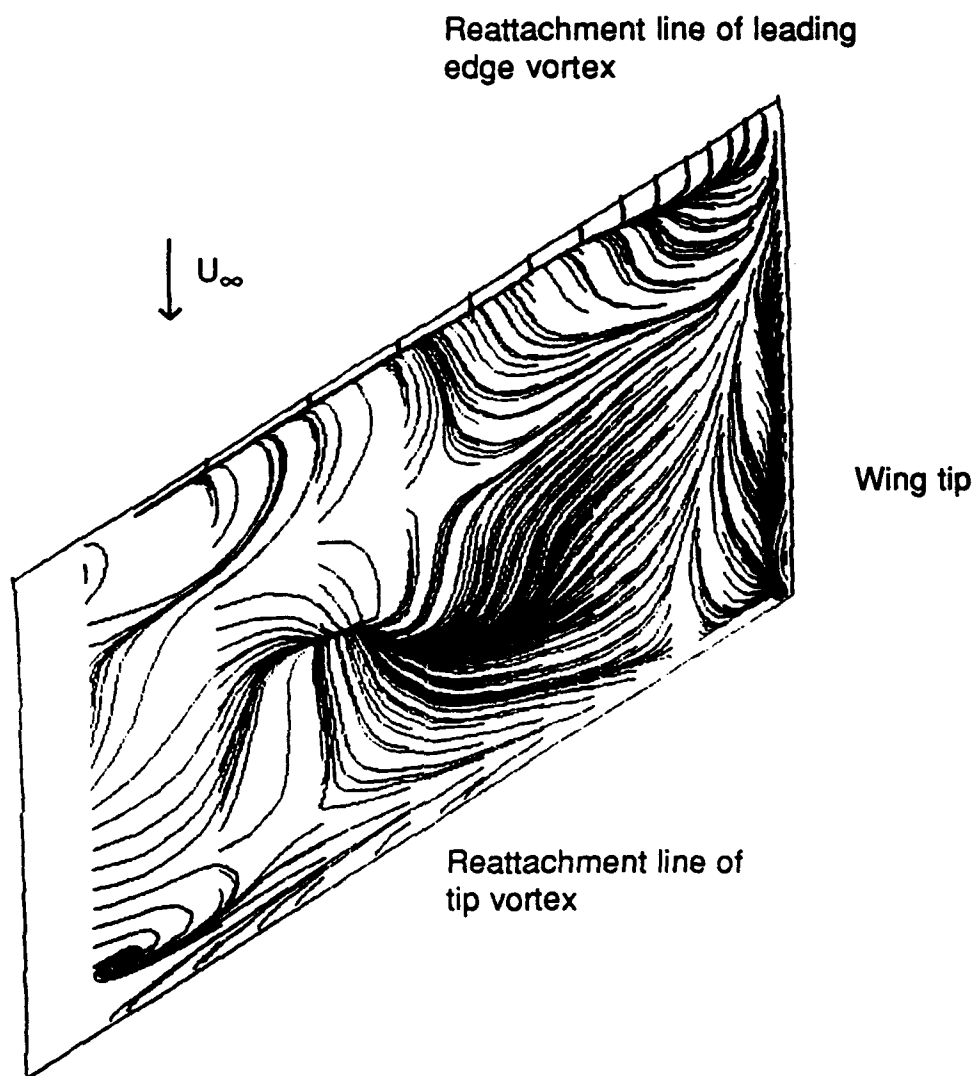


Figure 5-20. Oil Flow Pattern on a 30° Forward Swept Wing
at $Re=4 \times 10^4$, $\alpha = 27^\circ$ and $M = 0.02$

5.3.2 Computations for Dynamic Conditions

The simulations were further made for dynamic wing undergoing oscillatory pitching. The angle of attack varies as equation (5.1). The rotation axis is the line connecting the root and tip $1/4$ chord. Figure 5-21 gives the oil flow pattern on the wing surface and particle traces at several spanwise locations during an oscillatory cycle. Unlike symmetric (rectangular) wings, a forward swept wing experiences pronounced effect of tip vortex. This is evident from the large area occupied by the tip vortex at $\alpha = 25^\circ$ (Figure 5-21a) and at $\alpha = 22.3^\circ$ (Figure 5-21b). On the other hand, the leading edge vortex domain consists of a triangular wedge with base far inboard and apex near the leading edge of the wing tip. During the downstroke, the tip vortex penetrates inboard, and prevents the convection of the leading edge vortex into the wake (see Figure 5-21d). Like a rectangular wing, there is a rapid disappearance of the leading edge vortex at $\alpha = 5^\circ$. During the upstroke, the tip vortex breaks down, (Figure 5-21f). The result is massive helical flow on the wing surface (Figure 5-21g). At the mean time, the broken tip vortex grows with the angle of attack (Figure 5-21h).

It is seen that the forward swept wing produces flow fields that differ significantly from those of a straight symmetric wing. The flow near the wing tip delays the separation far below the static stall angle during the downstroke.

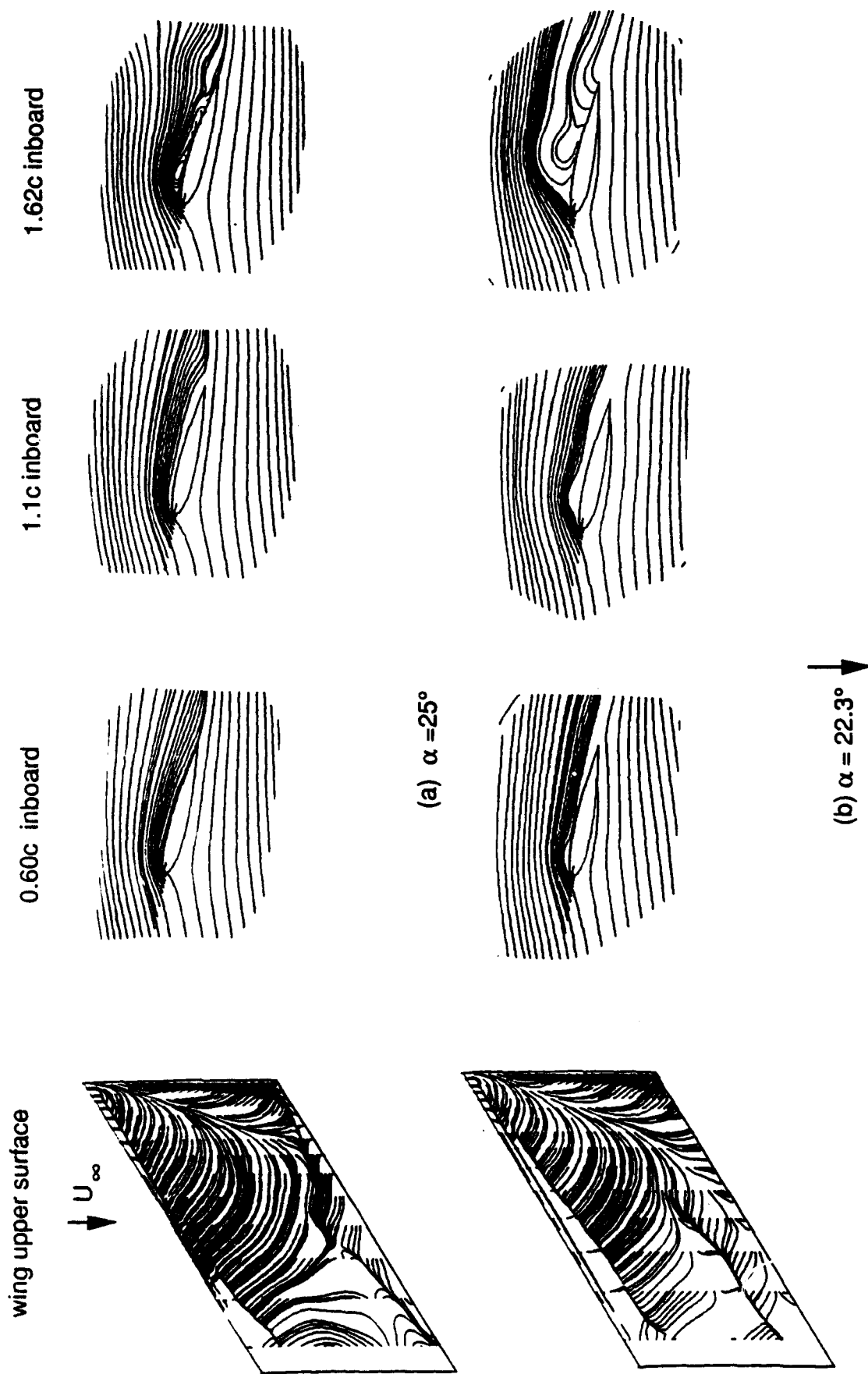


Figure 5-21. Oil-Flow Patterns (Simulated) and Particle Traces for a 30° Forward Swept Wing Undergoing Oscillatory Pitching. $Re = 4 \times 10^4$, $k = 1.0$, $\alpha_m = 15^\circ$, $\Delta\alpha = 10^\circ$, and $M=0.02$

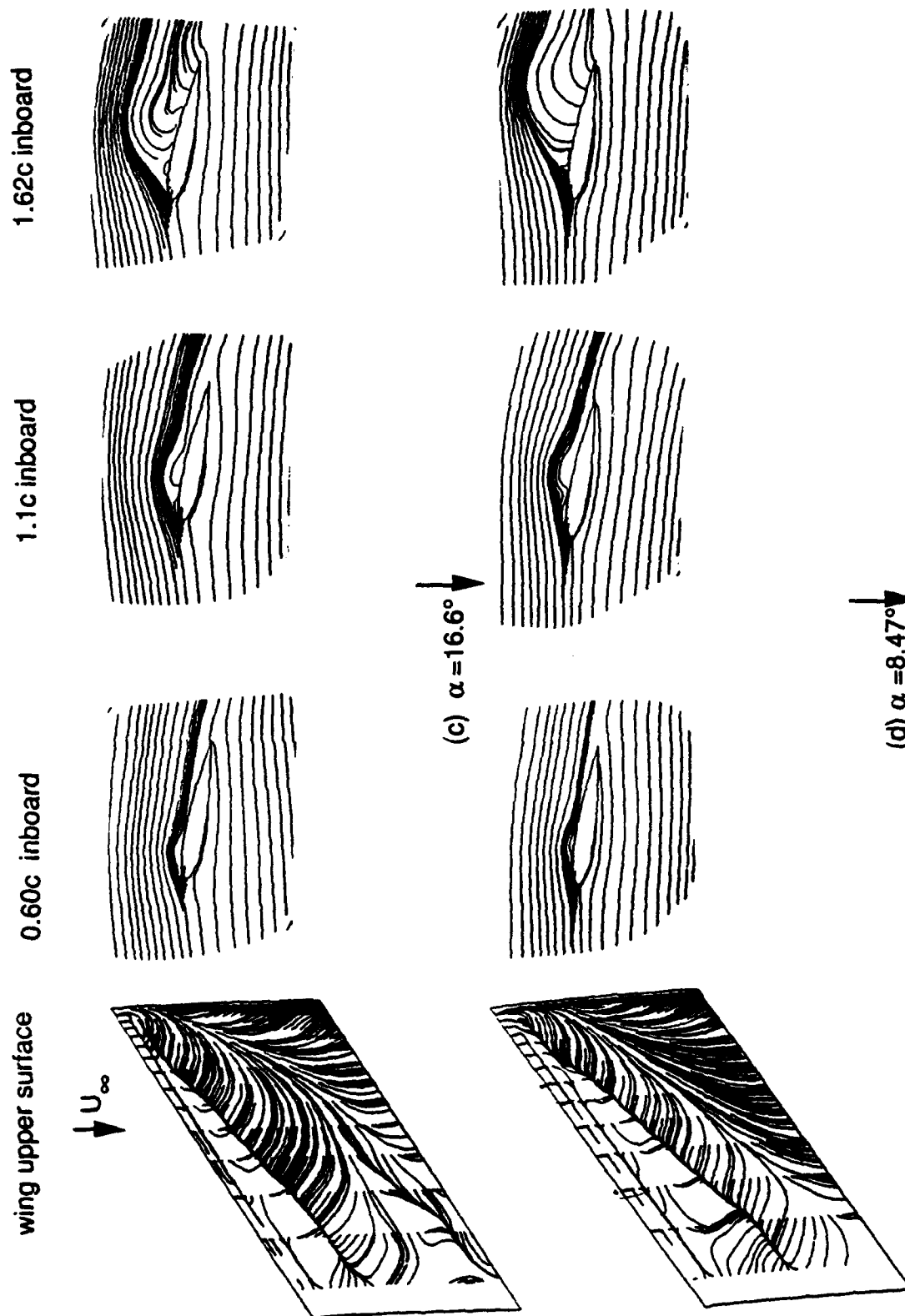


Figure 5-21. Continued

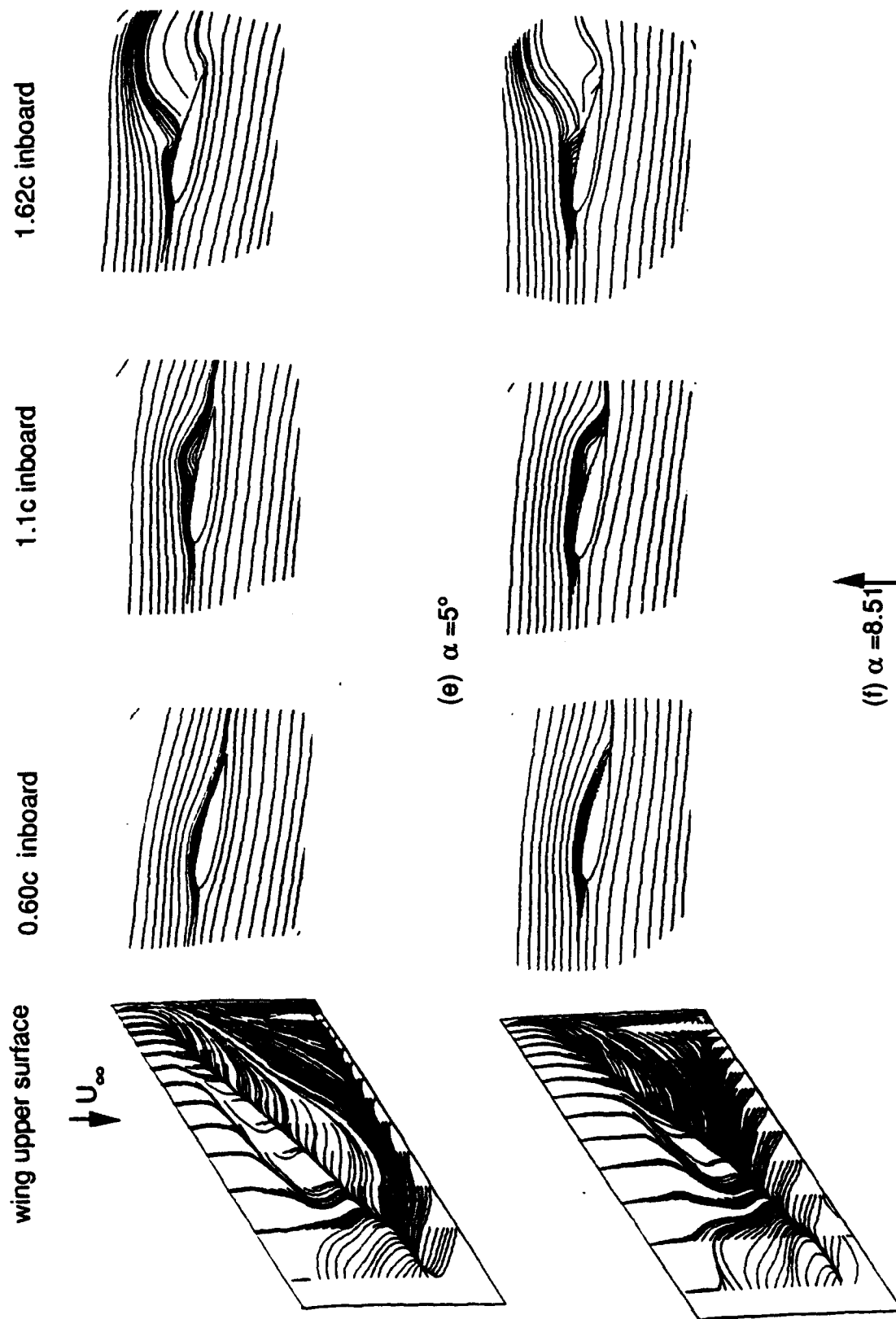


Figure 5-21. Continued

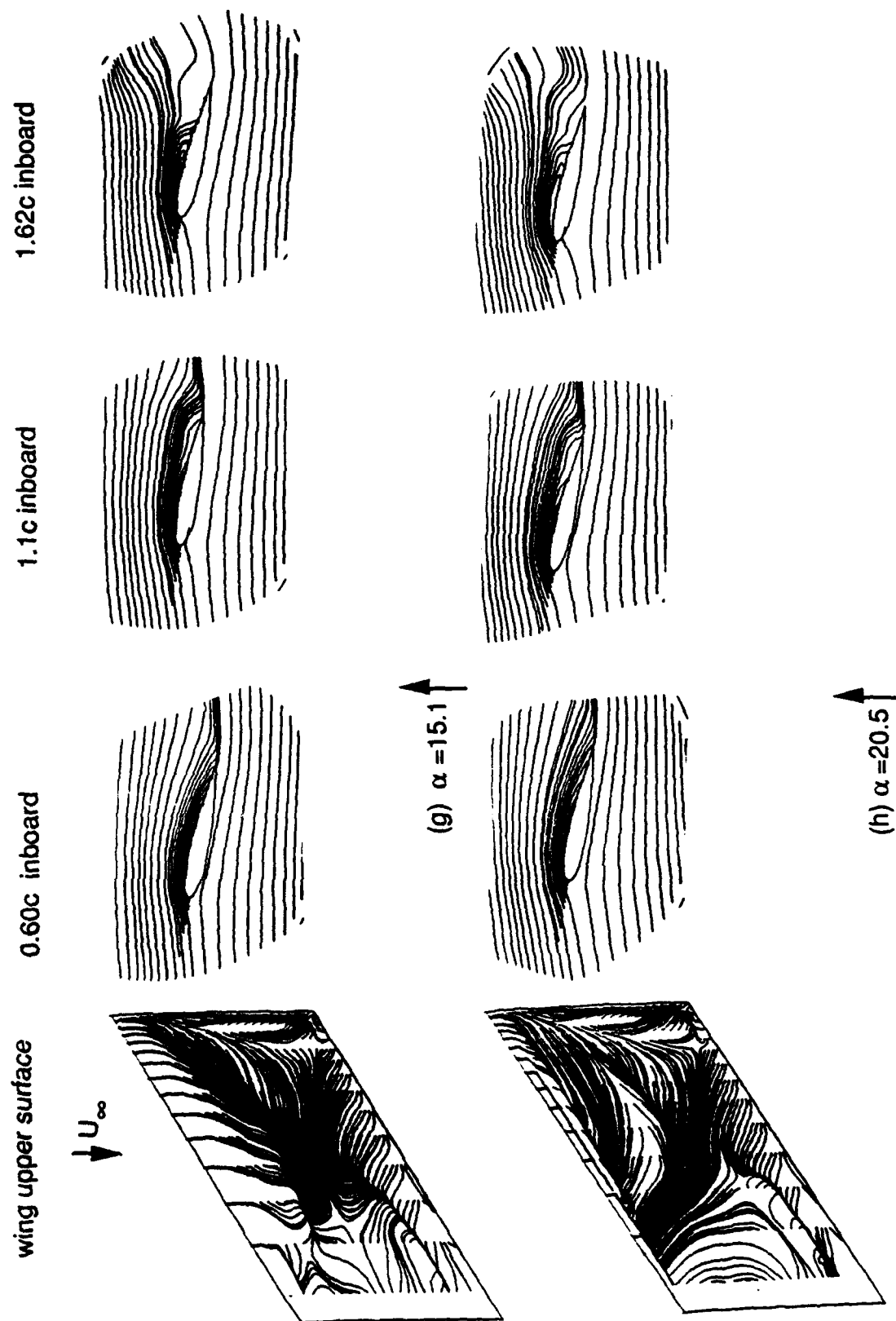


Figure 5-21. Continued

The previous studies on two-dimensional airfoils show that the upward motion generates a leading edge vortex that passes over the chord to the trailing edge. Depending on the reduced frequency k value, a trailing edge vortex is elicited with the opposite sign. This trailing edge vortex often causes a rapid separation of the flow from the airfoil surface. In the present calculation, there is little evidence of a trailing edge vortex. It appears that the tip vortex suppresses the initiation of the trailing edge vortex (see Figure 5-21); therefore, the dramatic flow separation does not coincide with the passage of the leading edge vortex into the wake. The present work is consistent with the work of Gad-el-Hak⁴⁷, Carta⁴⁹, and Ashworth *et al.*⁵⁶ in that vortices form over the upper surfaces at high angles of attack and these vortices simply increase or decrease in size as pitching is introduced.

5.4 Dynamic Stall on a Swept Back Wing

Computations were made for the same conditions as those for the forward swept wing. A 30° swept back wing was analyzed to investigate the effect of sweep. Both static and dynamic stalls were calculated, but only dynamic stall is presented below.

Given in Figure 5-22 are similar to those graphics in Figure 5-21, showing the oil-flow pattern at the upper wing surface and particle traces at several spanwise locations. In contrast to the forward swept wing, the leading edge vortex now becomes large along the spanwise direction toward the wing tip. The interaction between the leading edge vortex and the tip vortex still exists but is only limited to the proximity of the wing tip. The generation and propagation property of the leading edge vortices is similar to that in the forward swept wing. The unique aspect of a swept back wing during dynamic stall is that the swept back generates flow from the wing root toward the tip. This flow motion resists the inboard flow produced near the wing tip by the tip vortex. Vorticity is then accumulated into a

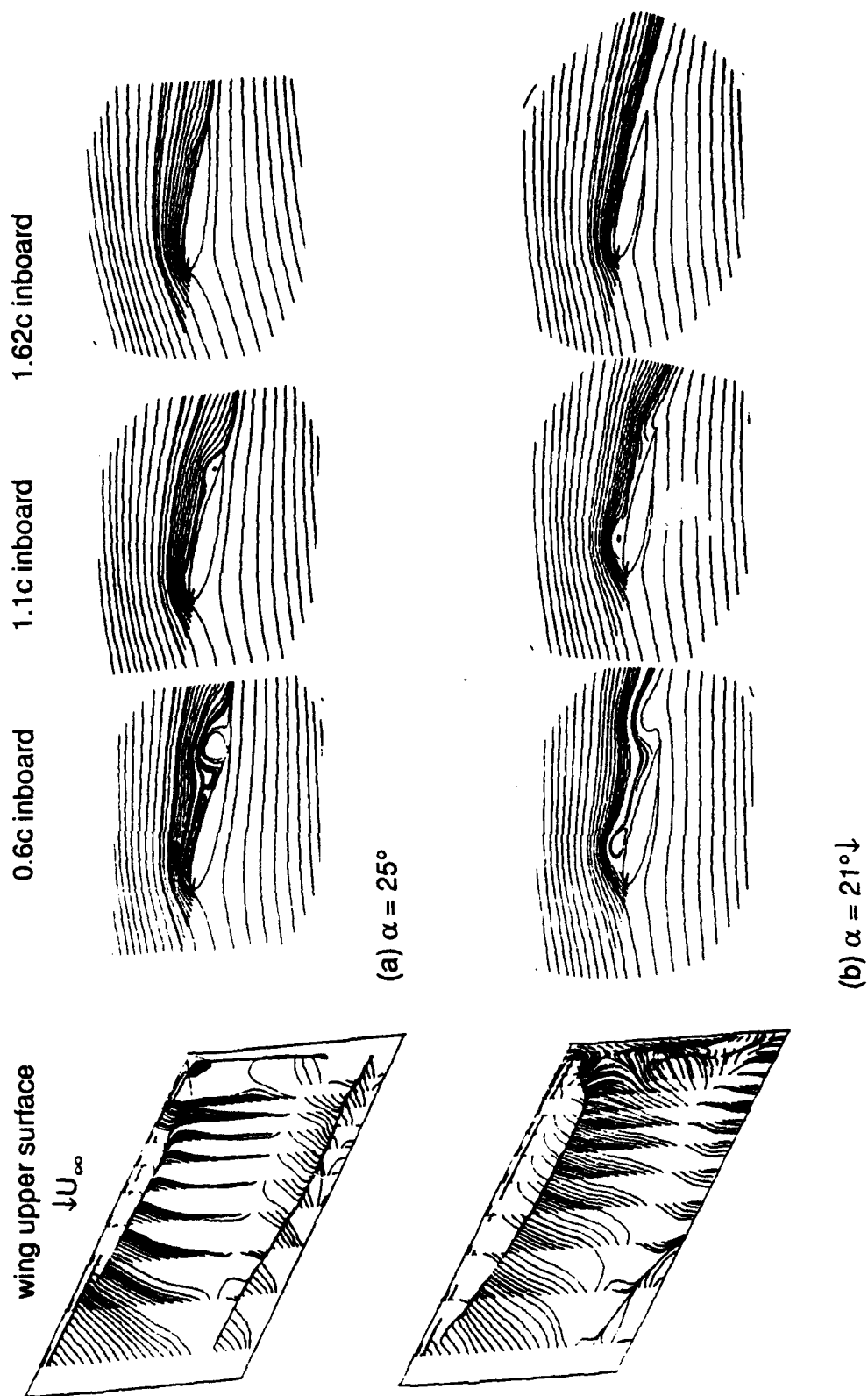


Figure 5-22. Oil-Flow Patterns (Simulated) and Particle Traces for a 30° Swept Back Wing Undergoing Oscillatory Pitching. $Re = 4 \times 10^4$, $k = 1.0$, $\alpha_m = 15^\circ$, $\Delta\alpha = 10^\circ$, and $M = 0.02$

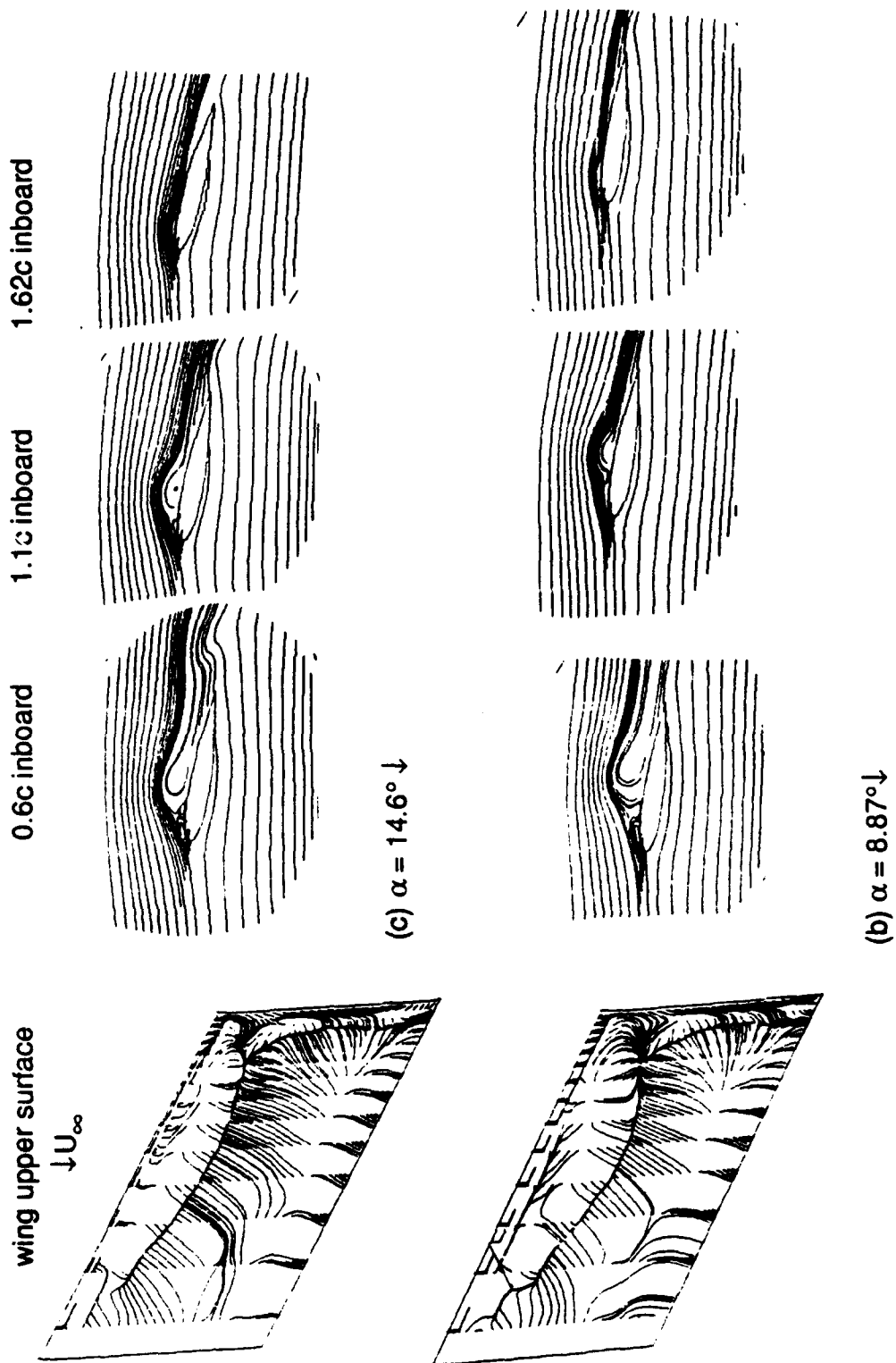


Figure 5-22. Continued

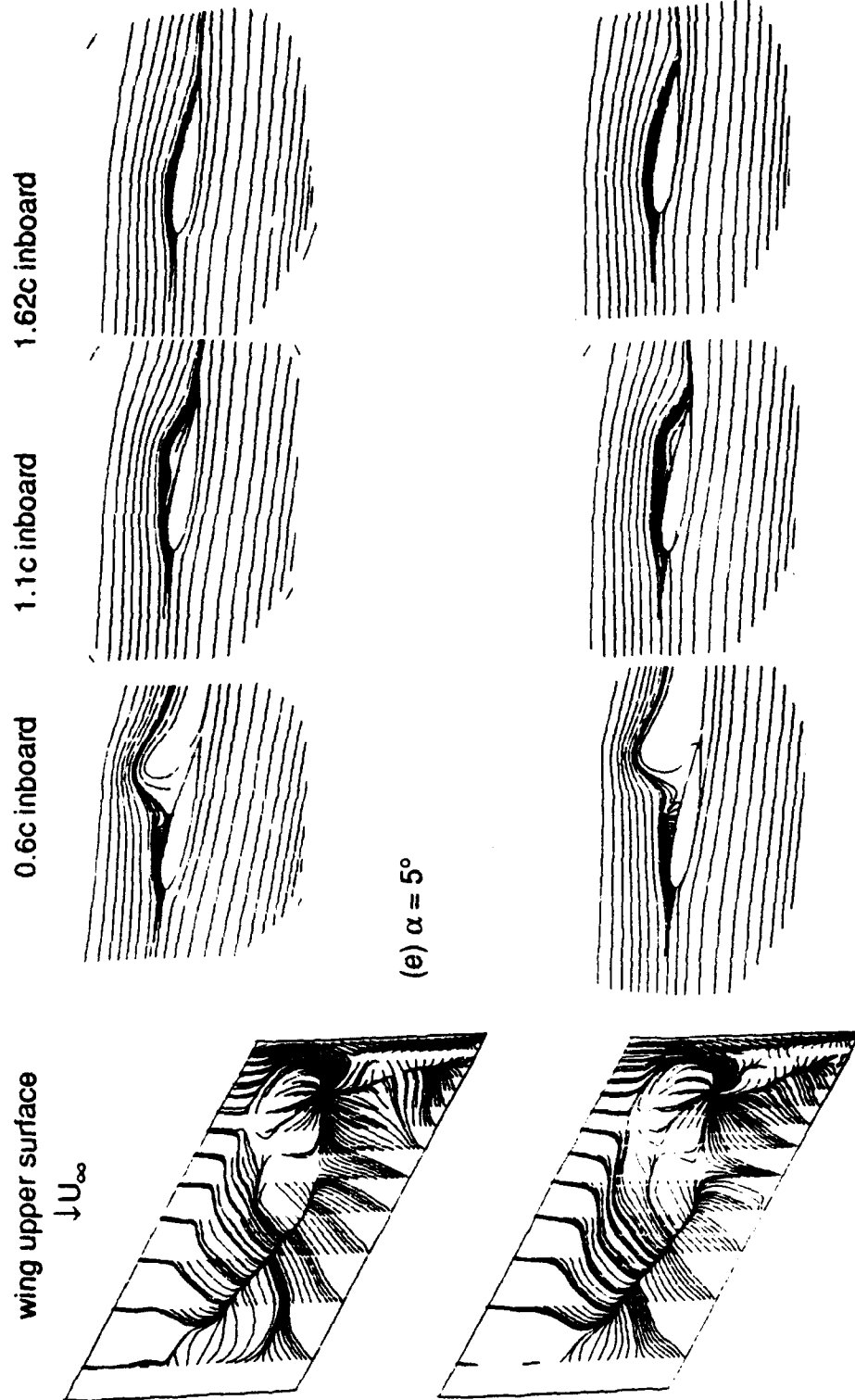
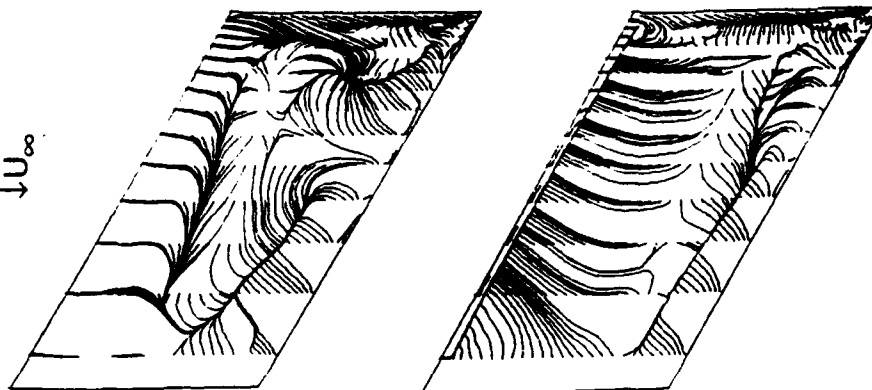
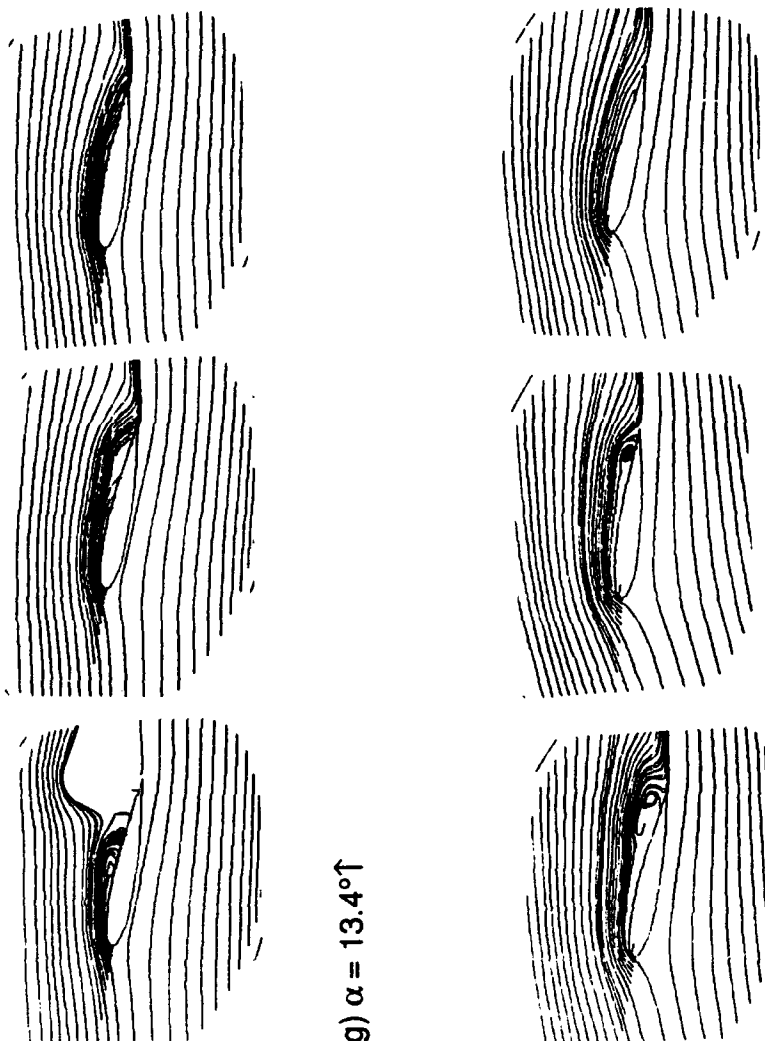


Figure 5-22. Continued

wing upper surface
 $\downarrow U_\infty$



0.6c inboard 1.1c inboard 1.62c inboard



(g) $\alpha = 13.4^\circ \uparrow$

(h) $\alpha = 23.5^\circ \uparrow$

Figure 5-22. Continued

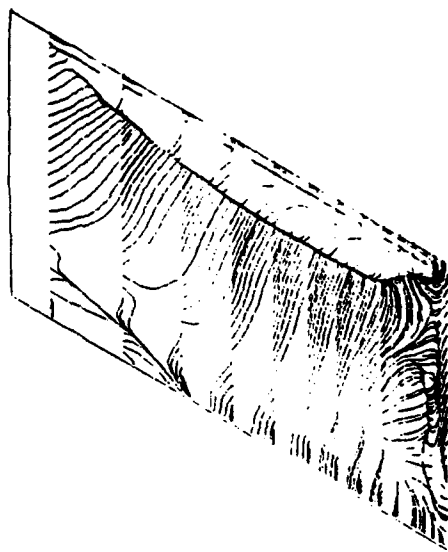
structured leading edge vortex on the swept back wing surface at spanwise points proximal to the wing tip.

To compare the characteristics of the interaction of the leading edge vortex and the tip vortex for the three different wings (30° swept back wing, rectangular wing, and 30° forward swept wing), the surface oil-flow patterns at $\alpha = 22^\circ$, and $\alpha = 8^\circ$ during the downstroke are shown in Figure 5-23 and Figure 5-24. It is seen that the forward swept wings and swept back wings produce spanwise fluid motion along the top surface. The minimum pressure line, corresponding to the leading edge vortex core line, runs roughly parallel to the wing leading edge. Since the airflow is not orthogonal to the line, the span-directional velocities are produced. The influence of tip vortex is the most pronounced and penetrates far inboard for the forward swept wing, and is limited only to the wing tip for the swept back wing.

Starting from a wing root, the leading edge vortex size increases toward the wing tip for the swept back wing, keeps constant for the rectangular wing, and decreases for a forward swept wing. A swept back wing, for which the wing surface area covered by a vortical structure is significantly larger than the forward swept wing, has the potential of providing the ideal fluid dynamic characteristics for unsteady lift enhancement. This is proven in Figure 5-25, which shows the lift coefficients for the above three wings.

(a) 30° Swept Back Wing

$\alpha = 21^\circ \downarrow$



(b) Rectangular Wing

$\alpha = 21.2^\circ \downarrow$



Wing Tip

(c) 30° Forward Swept Wing

$\alpha = 23.3^\circ \downarrow$

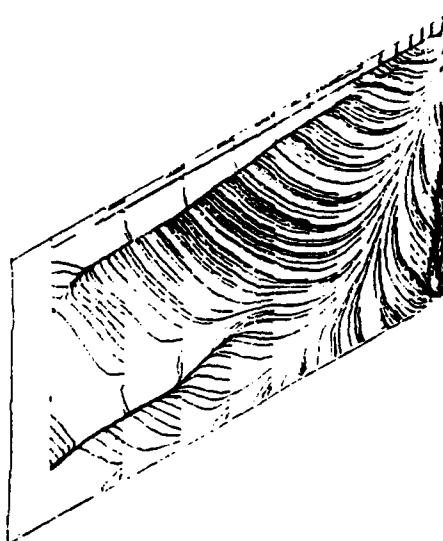
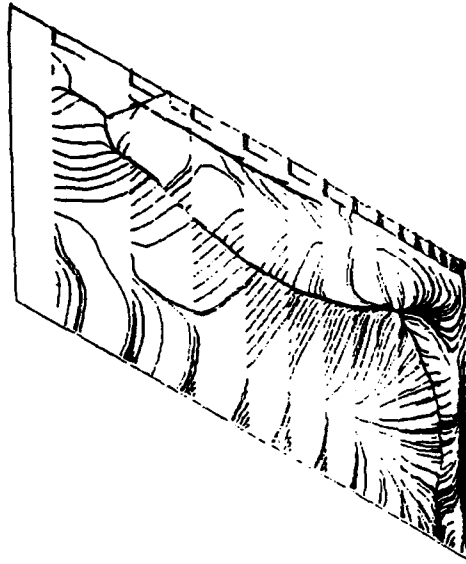


Figure 5-23. Comparison of Oil-Flow Patterns (Simulated) on the Upper Surface of a 30° Swept Back Wing, a Rectangular Wing, and a 30° Forward Swept Wing During Downstroke of an Oscillation Cycle around $\alpha = 22^\circ$

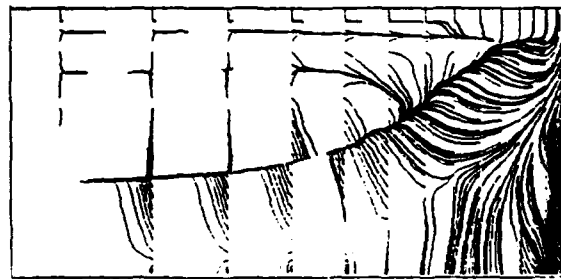
(a) 30° Swept Back Wing

$$\alpha = 8.87^\circ \downarrow$$



(b) Rectangular Wing

$$\alpha = 6.7^\circ \downarrow$$



Wing Tip

(c) 30° Forward Swept Wing

$$\alpha = 8.47^\circ \downarrow$$

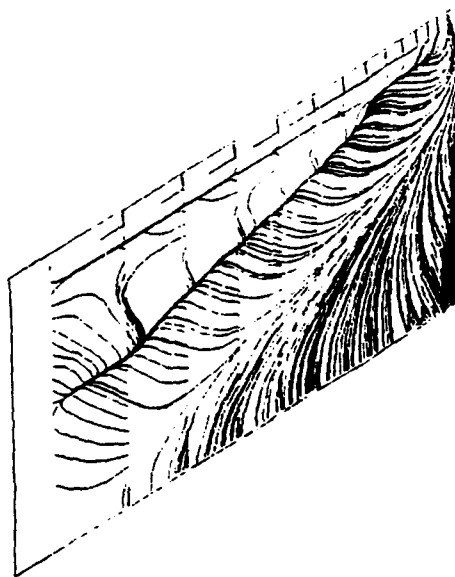


Figure 5-24. Comparison of Oil-Flow Patterns (Simulated) on the Upper Surfaces of a 30° Swept Back Wing, a Rectangular Wing and a 30° Forward Swept Wing During Downstroke of an Oscillation Cycle Around $\alpha = 8^\circ$

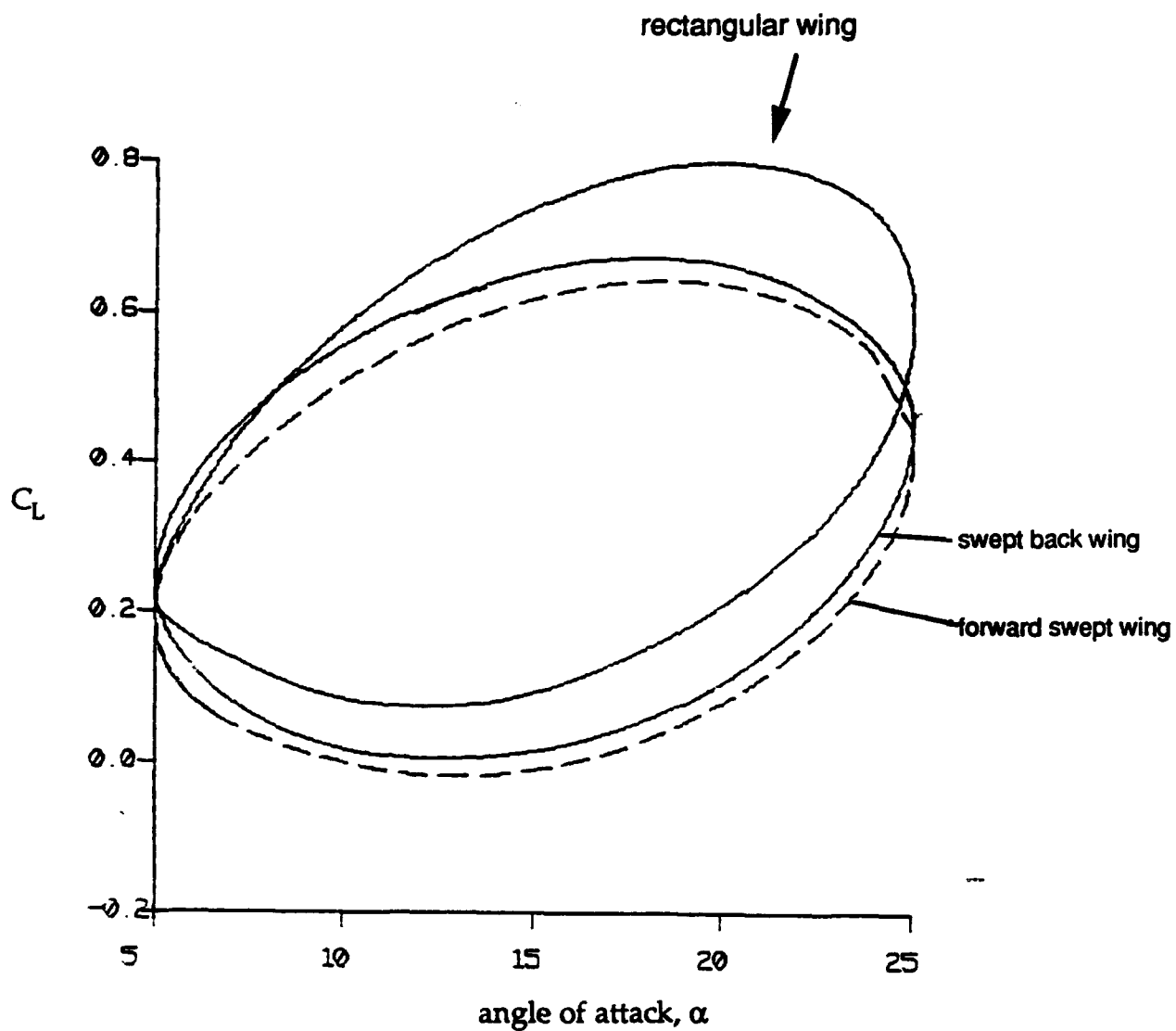
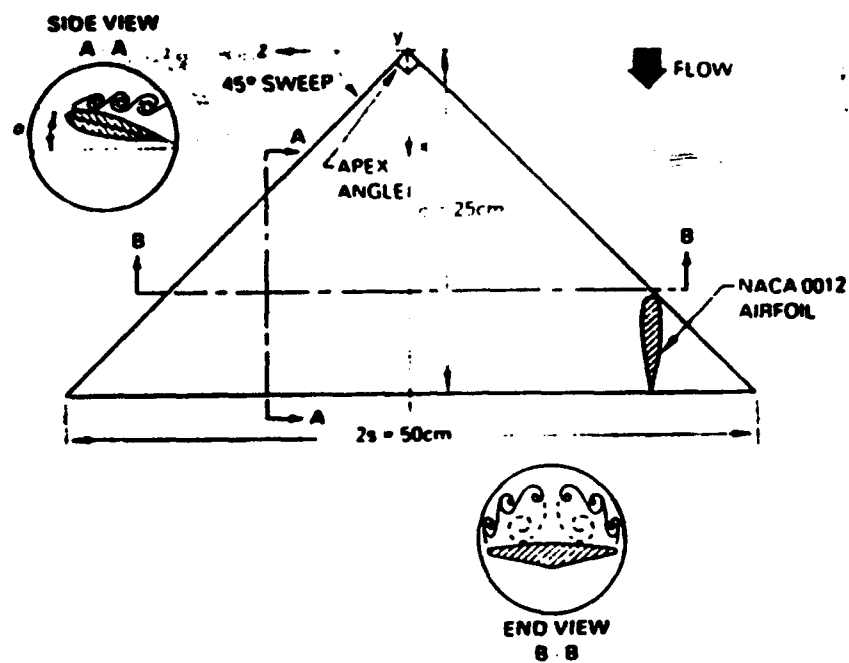


Figure 5-25. Lift Coefficients versus α for a Rectangular Wing, a 30° Swept Back Wing, and a 30° Forward Swept Wing Undergoing Oscillatory Pitching

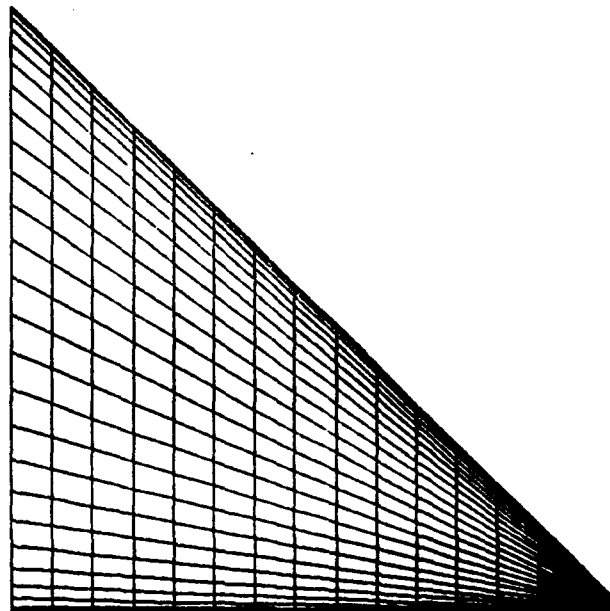
5.5 Static and Dynamic Stalls on a Delta Wing

In a steady flow, the lift of a two-dimensional airfoil is contributed mainly by the leading edge suction peak. The lift increases with increasing angle of attack until the stall angle is reached. The separation on the upper surface will then reduce the leading edge suction peak causing the lift to drop. The lift producing mechanism of a delta wing is somewhat different. There are two smooth such peaks inward of the leading edges. These peaks are produced by a pair of stationary leading-edge vortices formed by separated flow on the low-pressure side of the wing. Therefore, the lift on a delta wing is created by the separated vortical structures rather than by the attached flow over a convex surface.

In this section, the unsteady flow field around a delta wing is studied by numerical simulation. The delta wing has a 45 degree sweep. The Reynolds number based on the root chord is 1.7×10^4 . Figure 5-26a is a sketch of the 45° delta wing, which has a NACA0012 profile at each spanwise section. The wing is pitched around the quarter-chord position. The angle of attack varies with time in the same way as shown in Equation (5.1). The reduced frequency is 0.24. The computational grid is $50 \times 39 \times 18$ (circumferential \times radial \times spanwise). The upper surface grid is shown in Figure 5-26b.



(a) Schematic of a 45° Swept Delta Wing and Definition Sketch



(b) Computational Surface Grid

Figure 5-26. Configuration of a 45° Delta Wing

The oil-flow patterns for static delta wing are shown in Figure 5-27. At an angle of attack of 5° , the flow is attacked, and the leading edge vortex roll-up can be identified from the separation line. This roll up vortex is a spiral vortex sheet shed from the leading edge as shown in Figure 5-28. At a high angle of attack, the separation on the delta wing starts from the leading edge corner. This is different from a rectangular wing which initiates a separation at the trailing edge. The separation zone propagates to the wing root with increasing α (see Figure 5-27c-d). There is a focal point on the wing surface at $\alpha = 15^\circ$. This in turn generates a helical flow leaving the wing surface. The three-dimensional particle traces for this angle ($\alpha = 15^\circ$) are shown in Figures 5-29 and 5-30.

Figure 5-31 shows the surface oil-flow patterns for the delta wing at several angles of attack during an oscillatory cycle. At the early stage of the upstroke, Figure 5-31a-b, there is a tip roll-up characterized by the separation along the leading edge. This tip roll-up forms a spiral vortex sheet as shown in Figure 5-28. With an increase in the angle of attack, Figure 5-31c, the separation of the leading vortex starts from the trailing edge corner, and propagates upstream and inward (see Figure 5-31c-e). During the downstroke, the flow starts to reattach. For example, at $\alpha = 16.5^\circ \downarrow$, the flow near the whole leading edge (from the apex to the corner of the trailing edge) becomes reattached. It is interesting to note that the leading edge vortex does not convect, rather it experiences a grow-decay cycle.

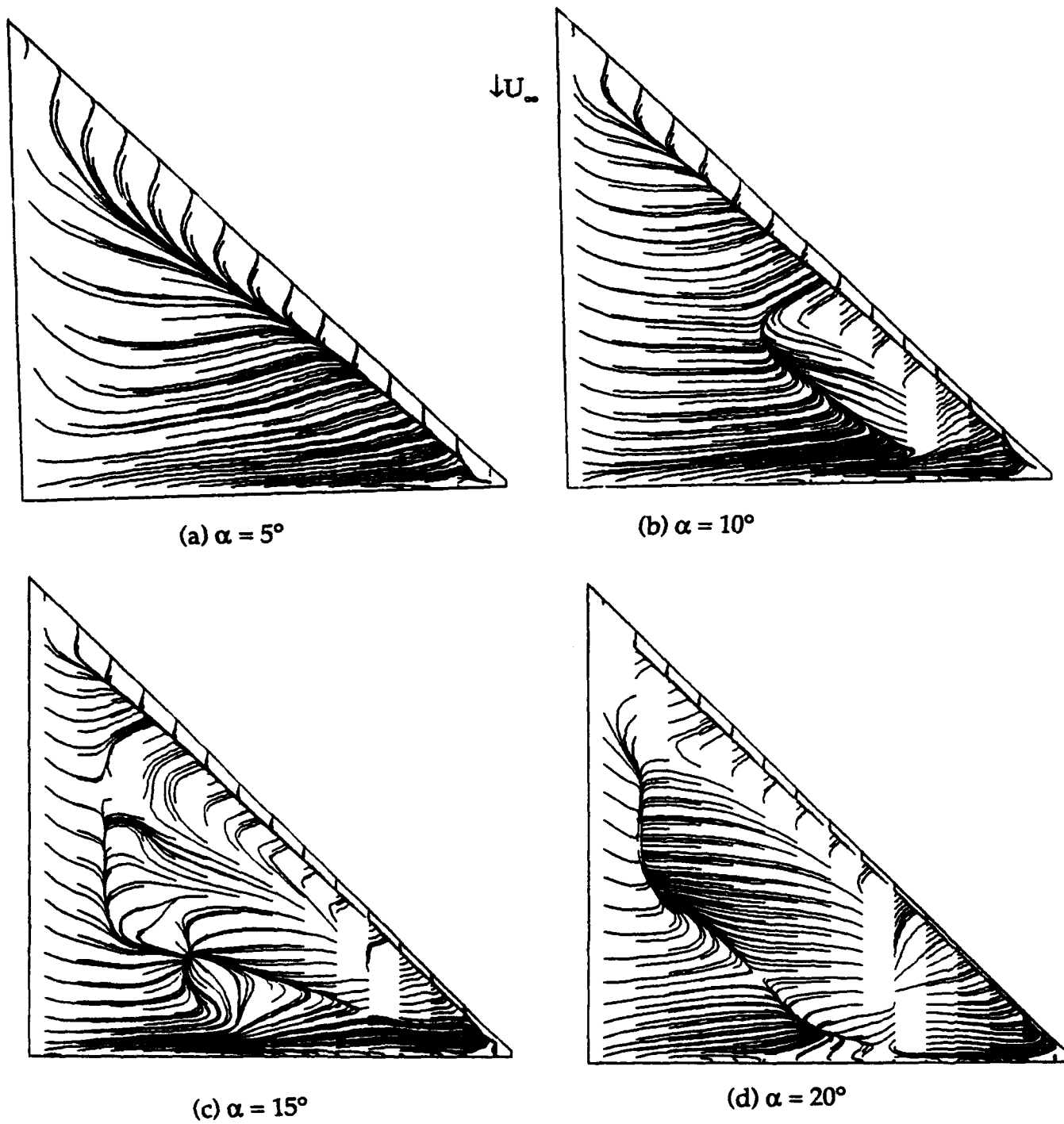


Figure 5-27. Surface Oil-Flow Patterns (Simulated) for a Static Delta Wing
at $\alpha = 5^\circ, 10^\circ, 15^\circ$ and 20° , $Re = 17,000$, and $M_\infty = 0.02$

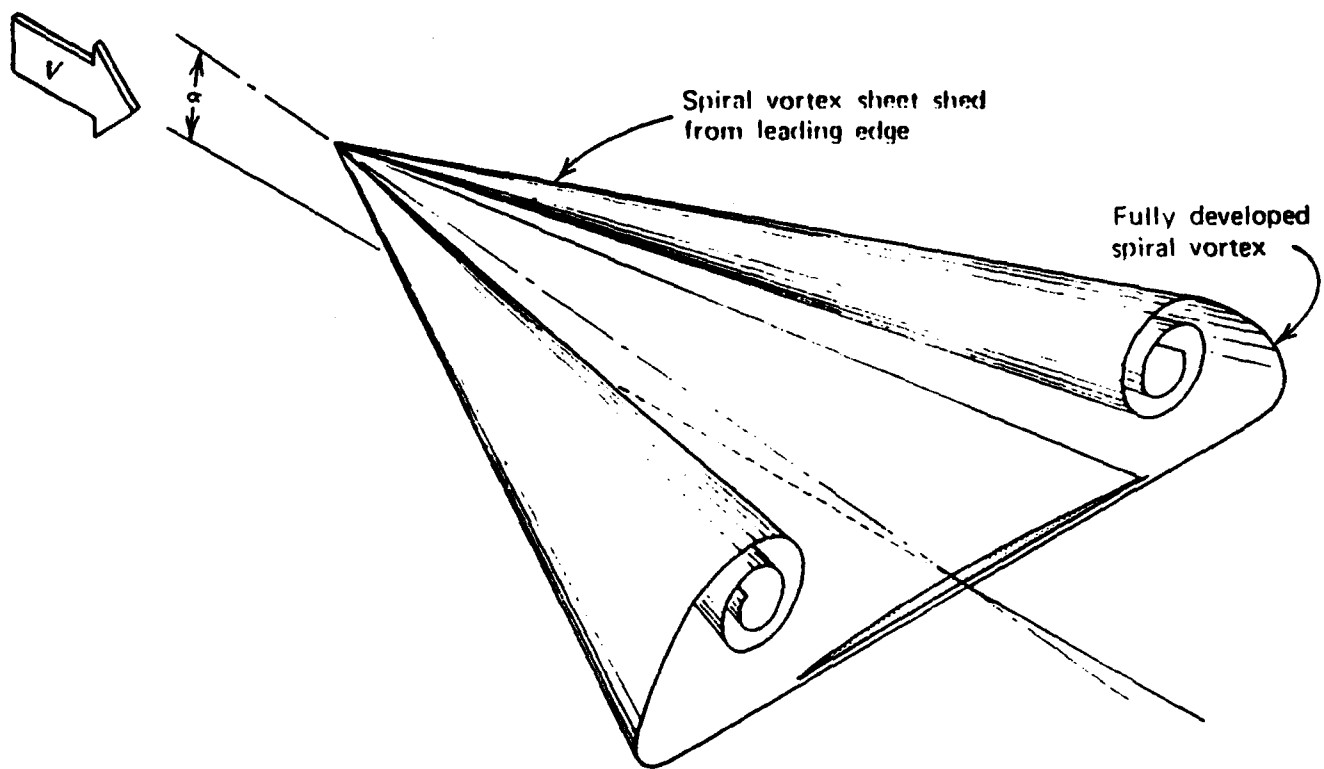


Figure 5-28. Leading Edge Vortices Formed Above a Delta Wing

PARTICLE TRACES COLORED BY VELOCITY MAGNITUDE

CONTOUR LEVELS

3.50000
1.00000



Side View

Figure 5-29. Particle Traces around a Static Delta Wing
 $M = 0.02$ $\text{Alfa} = 15 \text{ deg.}$ $\text{Re} = 17,000$

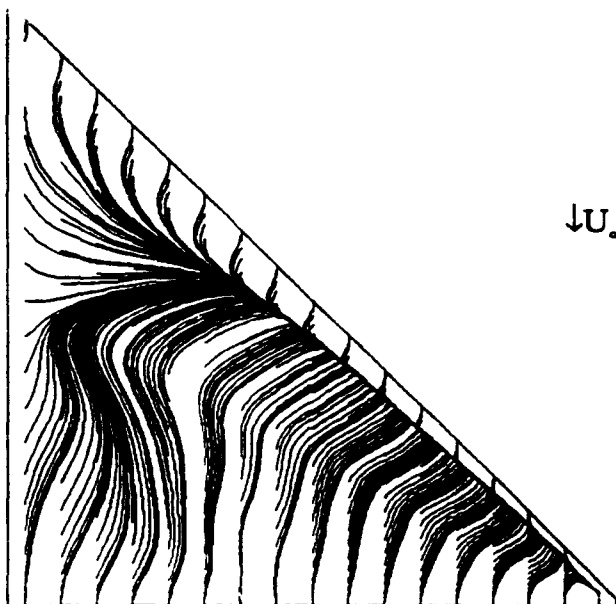
PARTICLE TRACES COLORED BY VELOCITY MAGNITUDE

CONTOUR LEVELS

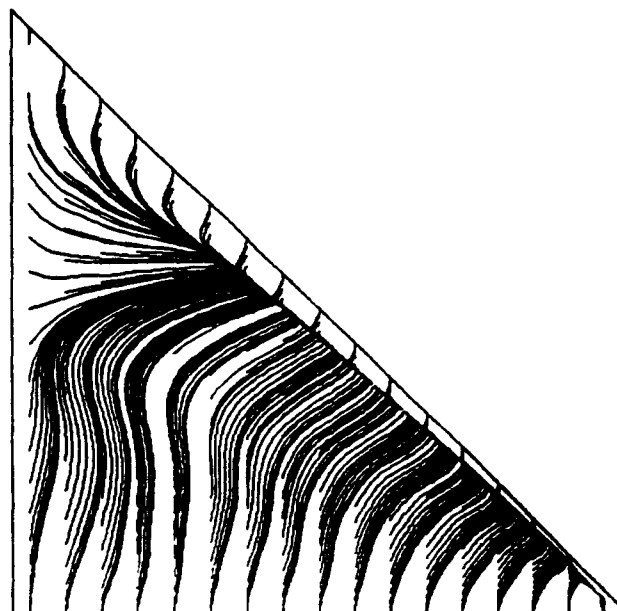
3.00000
3.50000
4.00000

Top View

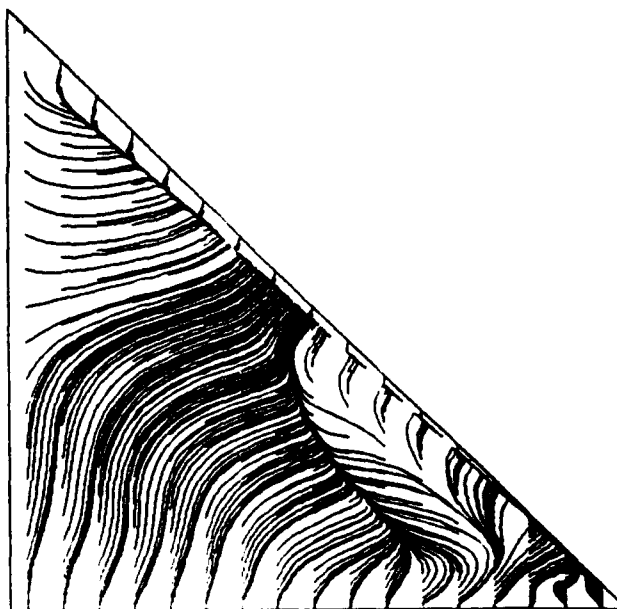
Figure 5-30. Particle Traces around a Static Delta Wing
 $M = 0.02$ $\text{Alfa} = 15 \text{ deg.}$ $\text{Re} = 17,000$



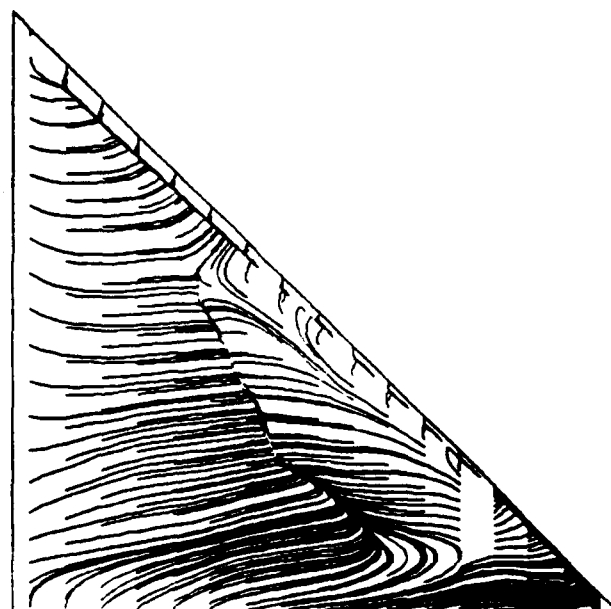
(a) $\alpha = 7.7^\circ \uparrow$



(b) $\alpha = 10.2^\circ \uparrow$



(c) $\alpha = 19.2^\circ \uparrow$

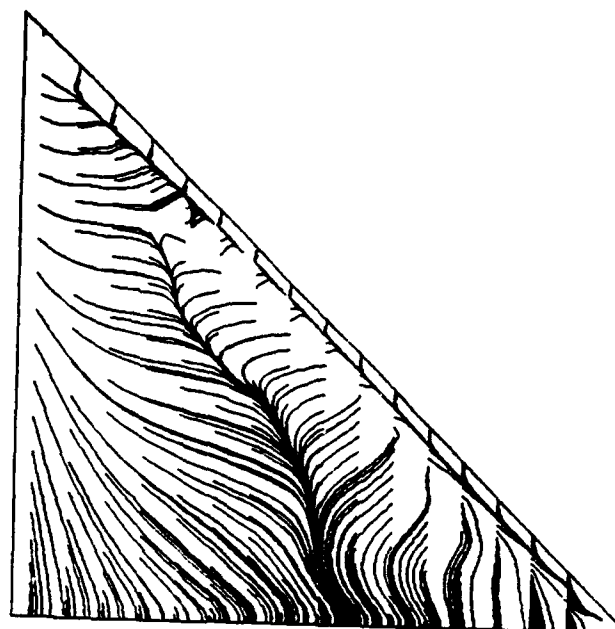


(d) $\alpha = 25^\circ \uparrow$

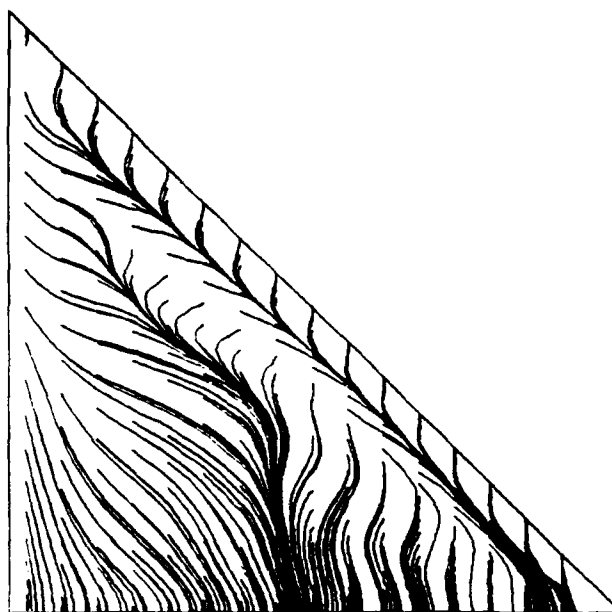
Figure 5-31. Oil-Flow Pattern (Simulation) on a 45° Swept Delta Wing Undergoing Oscillatory Pitching. $Re = 1.7 \times 10^4$, $k = 0.24$, $M = 0.02$, $\alpha_m = 15^\circ$, and $\Delta\alpha = 10^\circ$



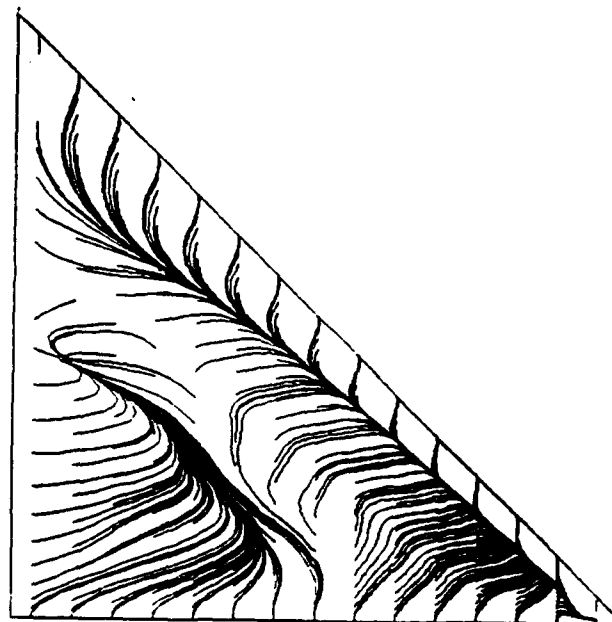
(e) $\alpha = 22.0^\circ \downarrow$



(f) $\alpha = 16.5^\circ \downarrow$



(g) $\alpha = 8.0^\circ \downarrow$



(h) $\alpha = 5^\circ$

Figure 5-31. (Continued)

6. CONCLUSIONS AND RECOMMENDATIONS

6.1 Conclusions

The design of future generation combat aircraft for increasing level of performance requires good control capability at the high pitch rates at angles of attack beyond maximum static lift. This, in turn, requires detailed knowledge and exploitation of the highly unsteady vortical flow field in the vicinity of the vehicle. The present six-month SBIR Phase I study developed several new methodologies for pressure-based Navier-Stokes equation solvers. With the developed techniques, both steady and unsteady separating flows are analyzed for 2-D airfoil and 3-D rectangular, forward swept, swept back and delta wings. Based on the present investigation, the following concluding remarks can be made.

1. The pressure-based method was demonstrated to be efficient (both in terms of storage and computation time requirements) for flows ranging from subsonic, transonic to supersonic, and from incompressible to compressible flows.
2. The presently developed TVD scheme for convective term discretization requires no artificial dissipation and can properly resolve the concentrated vortices with minimum numerical diffusion. When applied to transonic flows, the TVD scheme can capture shock with a single transition point. The property was demonstrated for the density-based methods but it has never been shown before for the pressure-based methods.
3. For inviscid supersonic flow over a NACA0012, the pressure-based TVD method is as accurate as density-based TVD, and performs better than the density-based method with artificial dissipation.

4. For steady viscous transonic flow, the present analysis well captures transition points and recirculating flows. It is very competitive relative to previous density-based analyses.
5. Comparisons with experimental visualization and measurement of the present solutions for 2D airfoil undergoing both constant pitch rate and oscillating motion are very good. All the essential physics are well preserved.
6. Validation study for 3D steady flow proves the accuracy of the present code.
7. The interaction between leading edge vortex and tip vortex for 3D forward swept wing, rectangular wing, swept back wing, and delta wing have been studied.

For a rectangular wing, the wing tip vortex dominates the outboard stations and interacts with the leading edge vortex at nearly right angle.

For a forward swept wing, due to the induction of spanwise flow toward the wing root, the effect of wing tip vortex penetrates deep into the wing surface, and suppresses the convection of leading edge vortex. In addition, the size of the leading edge vortex grows from the wing root.

For a swept back wing, the tip vortex effect is only limited to the proximity of the tip.

For the delta wing, the separation of the leading edge vortex starts from the corner and shifts inboard with pitch, but never truly convects downstream as in two dimensions.

6.2 Recommendations for Future Work

The current (Phase I) study has successfully verified the capability of pressure-based method in predicting steady and unsteady flows on 3D aerospace vehicles. Further studies are recommended to refine the computational model and to investigate several dynamic stall control schemes.

1. **Refinement of the Present Code.** In Phase I, due to limited availability of experimental data and limited project time, only static lift, pressure coefficients and dynamic visualizations have been compared and validated against experiments. In Phase II, systematic comparisons of predicted drag, lift and moment coefficients will be made with benchmark experimental measurements which are now undertaken at NASA Ames Research Center for 3D rectangular wing with NACA0015 cross-section. Since turbulence modeling is an essential part of the simulation, the assessment of Low Reynolds number turbulence model of J.Y. Chien, and Standard k- ϵ model will also be carried out.

2. **Dynamic Stall on Double-Delta Wing.** For a double-delta wing under static condition, there exists many interesting phenomena as shown in Figure 6-1. These include the interaction of strake vortices and wing vortices, asymmetry of vortical patterns, vortex bursting, and vortex sheet tearing¹¹⁷⁻¹¹⁹. Further study into dynamic condition during maneuvering will shed light on the fluid physics and will provide better controlling techniques.

3. Study of Dynamic Stall Control Schemes. With an understanding of basic fluid physics, and the well validated code, the various controlling concepts will be investigated by computer simulations. Several novel schemes proposed by Young are shown in Figure 6-2¹²⁰.

In Phase II, some of the recently proposed concepts will be considered:

- a. Vortex flap concept, Figure 6-3a.¹²¹
- b. Apex fence flaps, Figure 6-3b¹²¹. These devices are deployed at an angle to slender delta wing. They alter the vortical flow field and produce an intense suction at the apex which enhances the lift and gives a nose up pitching moment. At high angles of attack, they reduce apex lift and produce a desirable nose-down pitching momentum.
- c. Forebody strake, Figure 6-3d¹²². These strakes are conformally stored in the forebody, and when deployed, force asymmetric vortex shedding from the forebody, generating a controlled yawing moment.
- d. Spanwise blowing¹²³, Figure 6-3e. With realistic blowing rates, the jet momentum can stabilize the leading edge vortices and produce significant lift increments at high angles of attack.

4. Computational Flow Visualization. Dynamic stall numerical simulation creates large data sets which are difficult to analyze with existing graphic postprocessing tools such as PLOT3D, FAST, EXPLOT, FIELD-VIEW *etc.* Two types of graphic tools need to be developed to process and validate the computational results:

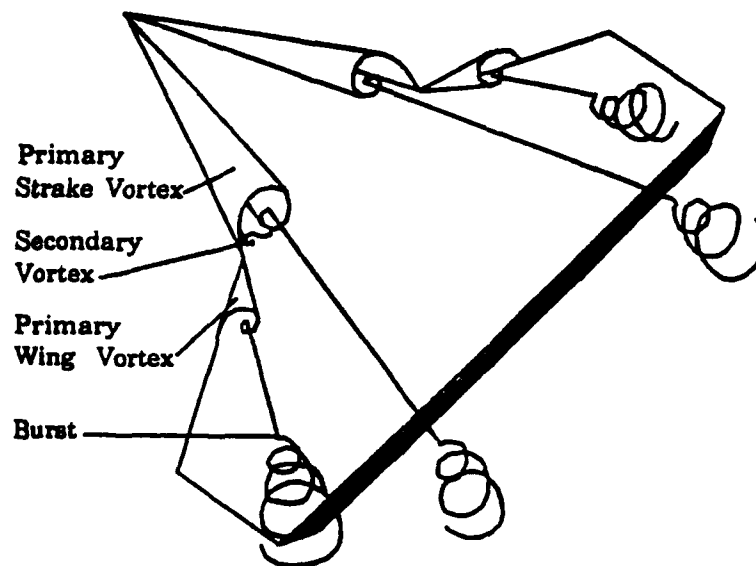


Figure 6-1. Typical Vortical Structure over a Double-Delta Wing at High Angle of Attack

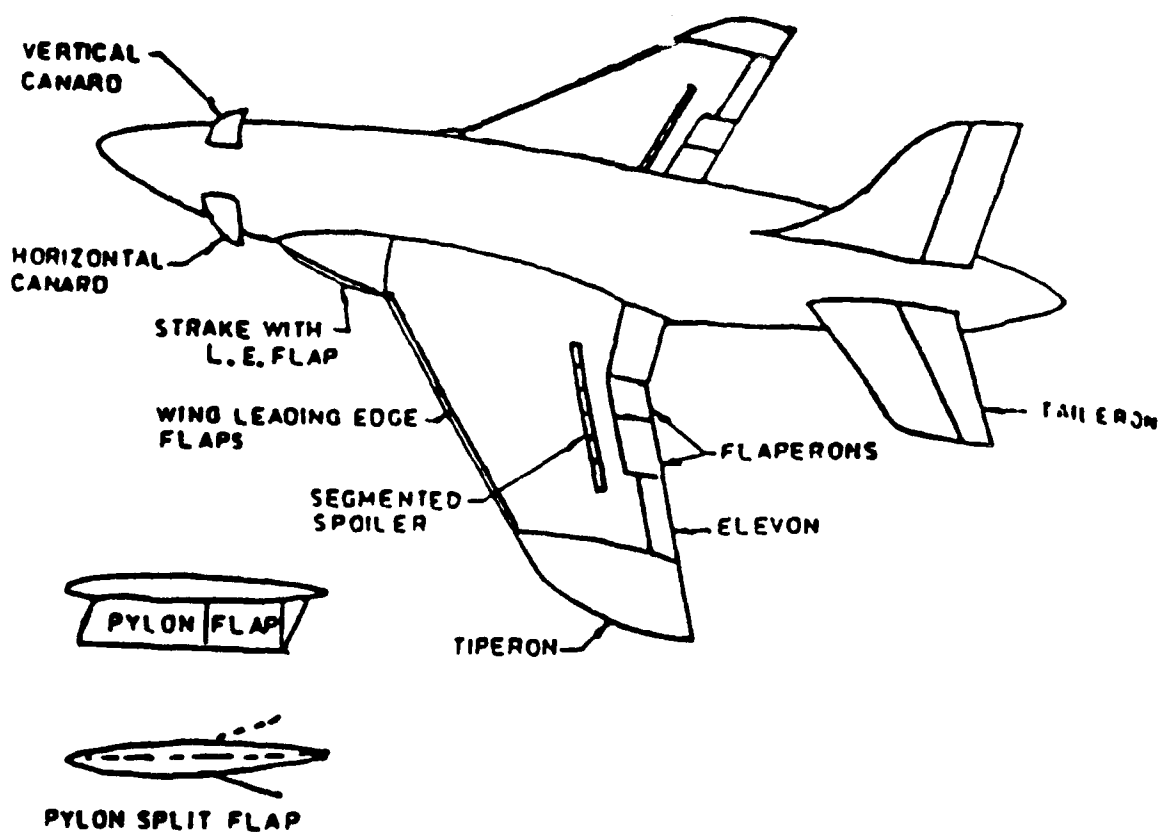


Figure 6-2. Some Novel Control Concepts

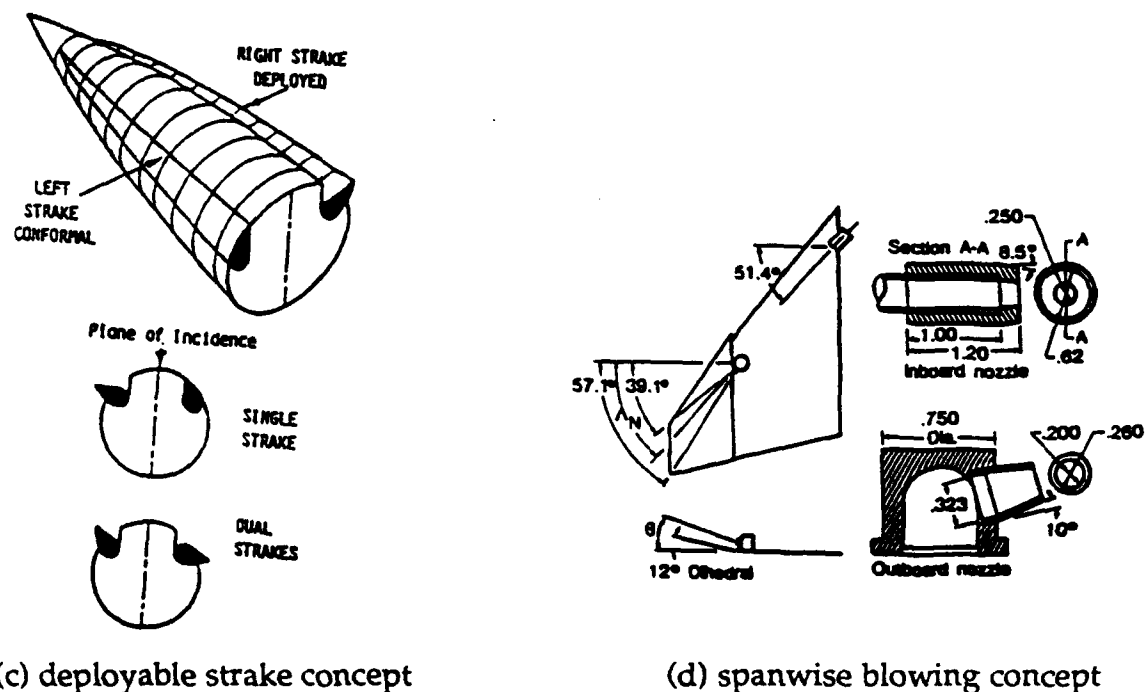
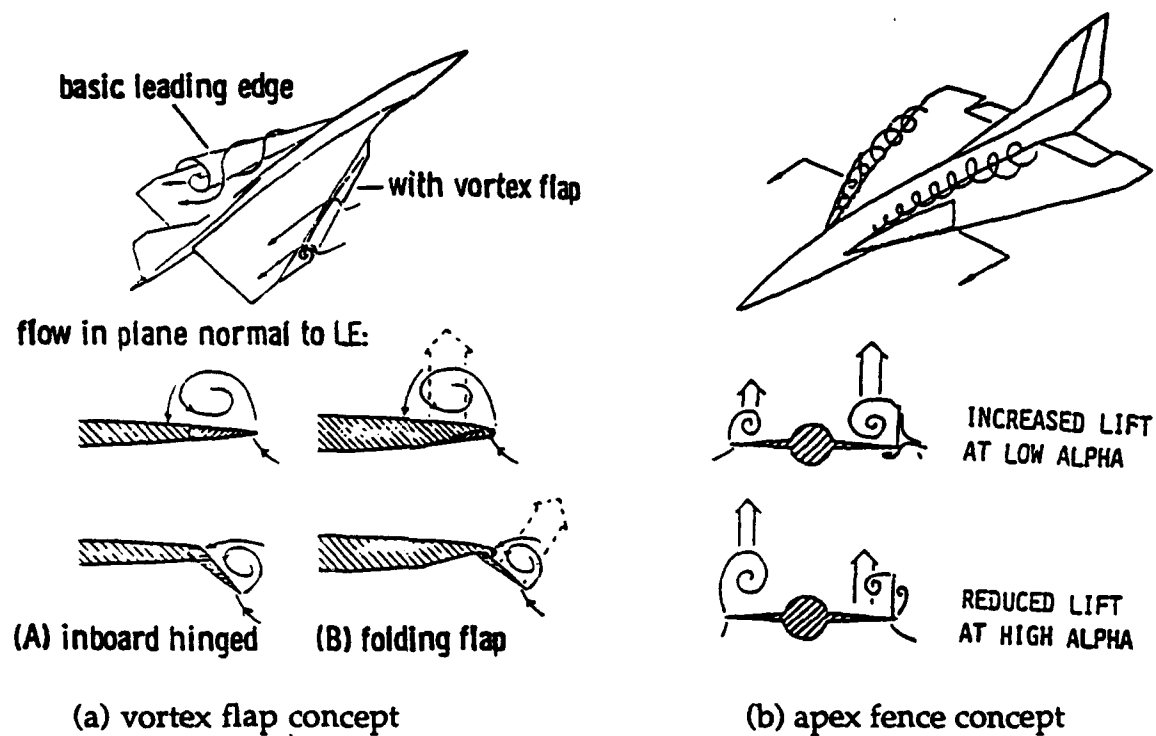


Figure 6-3. Potential Vortex Control Concepts for Phase II Study

- a. Dynamic image generation with animation capabilities, capable of generating shadowgraphs, Schlierens, and interferometry images, smoke traces, *etc.* Automatic detection and display of critical point lines and surfaces (separation lines, recirculation bubbles, *etc.*) are also essential.
- b. Graphical image examiner for alignment and comparison of computational versus experimental and computational versus computational flow images.

Both of the above packages, CFD-VIEW and CFD-Image are currently being developed at CFDRC on SGI graphic stations and will be adapted for the proposed dynamic stall flow analysis study.

The Phase II study will produce a validated 3D CFD code which will be of significant value to the U.S. Air Force, Federal Aviation Agency and aircraft manufacturers. This will also provide a strong foundation for further research and development of various dynamic stall control schemes for advanced combat aircraft.

7. REFERENCES

1. W.J. McCroskey, "The Phenomenon of Dynamic Stall," NASA TM-81264, 1981.
2. W.J. McCroskey, "Unsteady Airfoils," *Ann. Rev. Fluid Mech.*, Vol. 14, pp. 285-331, 1982.
3. L.W. Carr, "Progress in Analysis and Prediction of Dynamic Stall," *J. Aircraft*, Vol. 25, no. 1, pp.6-17, 1988.
4. M.C. Robinson and M.W. Luttges, "Vortex Generation Induced by Oscillating Airfoils: Maximizing Flow Attachment," 8th Biennial Symposium on Turbulence, Rolla, MD, pp. 13.1-13.10, September 26-28, 1983.
5. M.C. Robinson and M.W. Luttges, "Unsteady Flow Separation and Reattachment Induced by Pitching Airfoils," AIAA Paper AIAA-83-0131, 1983.
6. U.B. Mehta, "Starting Vortex, Separation Bubbles and Stall - A Numerical Study of Laminar Unsteady Flow Around an Airfoil," Ph.D. Thesis, Illinois Institute of Technology, Chicago, IL, 1972.
7. U. Gulcat, "Separate Numerical Treatment of Attached And Detached Flow Regions in General Viscous Flows," Ph.D. Thesis, Georgia Institute of Technology, Atlanta, GA, 1981.
8. Y. Tassa and L.N. Sankar, "Dynamic Stall of NACA0012 Airfoil in Turbulent Flow-Numerical Study," AIAA Paper, AIAA-81-1289, 1981.
9. L.N. Sankar and Y. Tassa, "An Algorithm for Unsteady Transonic Flow Past Airfoils," *Proceedings of the Seventh International Conference on Numerical Methods in Fluid Dynamics*, June, 1980.
10. L.N. Sankar and W. Tang, "Numerical Solution of Unsteady Viscous Flow Past Rotor Sections," AIAA Paper 85-0129, 1985.
11. J.C. Wu, "Zonal Solution of Unsteady Viscous Flow Problems," AIAA Paper 84-1637, 1984.
12. J.C. Wu, C.M. Wang and I.H. Tuncer, "Unsteady Aerodynamics of Rapidly Pitched Airfoil," AIAA Paper 86-1105, 1986.

13. J.C. Wu, C.M. Wang and U. Gulcat, "Zonal Solution of Unsteady Viscous Flow Problems," AIAA Paper 85-0034, 1985.
14. T. Cebeci, R.W. Clark, K.C. Chang, N.D. Halsey and K. Lee, "Airfoils with Separation and the Resulting Wakes," *J. of Fluid Mechanics*, vol. 173, pp.323-347, 1986.
15. T. Cebeci, L.W. Carr and H.M. Jang, "An Interactive Boundary-Layer Procedure for Oscillating Airfoils Including Transition Effects," AIAA Paper 89-0020, 1989.
16. M.R. Visbal, "Evaluation of an Implicit Navier-Stokes Solver for Some Unsteady Separated Flows," AIAA Paper 86-1083, 1986.
17. M.R. Visbal and J.S. Shang, "Comparative Study between Two Navier-Stokes Algorithms for Transonic Airfoils," *AIAA Journal*, vol. 24, pp. 596-606, 1986.
18. M.R. Visbal and J.S. Shang, "Investigation of the Flow Structure Around a Rapidly Pitching Airfoil," *AIAA Journal*, vol. 27, pp. 1044-1051, 1989.
19. M.R. Visbal, "Effect of Compressibility on Dynamic Stall of a Pitching Airfoil," AIAA Paper, 88-0132, 1988.
20. C.L. Ramsey and W.K. Anderson, "Some Numerical and Physical Aspects of Unsteady Navier-Stokes Computations Over Airfoils Using Dynamic Meshes," AIAA Paper 88-0329, 1988.
21. Y. Shida and K. Kuwahara, "Computational Study of Unsteady Compressible Flow Around an Airfoil by a Block Pentadiagonal Matrix Scheme," AIAA Paper 85-1692, 1985.
22. Y. Shida, K. Kuwahara, O. Kioaki, and W.J. Ohyu, "Computation of the Dynamic Stall of a NACA0012 Airfoil by Block Pentadiagonal Matrix Scheme," AIAA Paper 86-0116, 1986.
23. K. Ono, "Numerical Study on the Dynamic Stall Process of an NACA0012 Airfoil," AIAA Paper 85-0128, 1985.
24. J. Currier and K.Y. Fung, "An Analysis of the Onset of Dynamic Stall," AIAA Paper 91-0003, 1991.

25. H.M. Jang, J.A. Ekaterinaris, M.F. Platzer and T.Cebeci, "Essential Ingredients for the Computation of Steady and Unsteady Boundary Layers," ASME Paper 90-GT-160, 1990.
26. R. Beam and R.F. Warming, "An Implicit Factored Scheme for Compressible Navier-Stokes Equations," *AIAA Journal*, vol. 16, pp. 393-402, 1978.
27. R.H. Landon, "NACA0012 Oscillatory and Transient Pitching," AGARD Report No. 702, 1981.
28. G. Shrewsbury and L.N. Sankar, "Dynamic Stall of Circulation Control Airfoils," AIAA Paper 90-0573, 1990.
29. S.P. Grohsmyer, J.A. Ekaterinaris, and M.F. Platzer, "Numerical Investigation of the Effect of Leading Edge Geometry on Dynamic Stall of Airfoils," AIAA Paper 91-1798, 1991.
30. K. Ghia, J. Yang, G. Osswald and U. Ghia, "Study of the Role of Unsteady Separation in the Formation of Dynamic Stall Vortex," AIAA Paper 92-0196, 1992.
31. W.J. McCroskey and J.J. Philippe, "Unsteady Viscous Flow on Oscillating Airfoils," *AIAA Journal*, vol 13, pp. 71-79, 1975.
32. K.W. McAlister and L.W. Carr, "Water Tunnel Visualization of Dynamic Stall," *Journal of Fluids Engineering*, vol. 101, pp. 376-380, 1978.
33. J.M. Martin, R.W. Empey, W.J. McCroskey and F.X. Caradonna, "An Experimental Analysis of Dynamic Stall on an Oscillatory Airfoil," *Journal of the American Helicopter Society*, vol. 19, pp. 26-32, 1973.
34. P.W. Harper and R.E. Flanagan, "The Effect of Rate Change of Angle of Attack on the Maximum Lift of a Small Model," NACA TN-2061, 1950.
35. N.D. Ham and M.S. Garelick, "Dynamic Stall Considerations in Helicopter Rotors," *Journal of the American Helicopter Society*, pp. 40-50, July 1981.
36. M.S. Francis, J.E. Keesee and J.P. Retelle, "An Investigation of Airfoil Dynamic Stall with Large Amplitude Motion," U.S. Airforce Academy, Colorado Springs, CO, FJSRL-TR-83-0010, 1983.

37. A.C. Deekens and W.R. Kuebler, "A Smoke Tunnel Investigation of Dynamic Separation," *Aeronautics Digest*, USAF A-TR-79-1, pp. 2-16, 1979.
38. D.C. Daley, "The Experimental Investigation of Dynamic Stall," Thesis, Air Force Institute of Technology, Wright-Patterson Air Force Base, OH, AFIT/GAF/AA/820-6, 1983.
39. J.M. Walker, H.E. Helin and J.H. Strickland, "An Experimental Investigation of an Airfoil Undergoing Large Amplitude Pitching Motions," *AIAA Journal*, vol. 23, pp. 1141-1142, 1985.
40. M.S. Chandrasekhara and L.W. Carr, "Flow Visualization Studies of the Mach Number Effects on the Dynamic Stall of Oscillatory Airfoils, *Journal of Aircraft*, vol. 27, pp. 516-522, 1990.
41. M.S. Chandrasekhara, S. Ahmed, "Laser Velocimetry Measurements of Oscillatory Airfoild Dynamic Stall Flow Field," AIAA Paper 91-1799, 1991.
42. L.W. Carr, M.S. Chandrasekhara, S. Ahmed and N.J. Brock, "A Study of Dynamic Stall Using Real Time Interferometry," AIAA Paper 91-0007, 1991.
43. L.W. Carr and M.S. Chandrasekhara, "Design and Development of a Compressible Dynamic Stall Facility," AIAA Paper 89-0647, 1989.
44. S. Ahmed and M.S. Chandrasekhara, "Reattachment Studies of an Oscillating Airfoil Dynamic Stall Flow Field," AIAA Paper 91-3325, 1991.
45. M.S. Chandrasekhara and B.E. Brydges, "Amplitude Effect on Dynamic Stall of an Oscillatory Airfoil," AIAA Paper 90-0575, 1990.
46. M. Gad-el-Hak and C.-M. Ho, "Three-Dimensional Effects on a Pitching Lifting Surface," AIAA Paper 85-0041, 1985.
47. M. Gad-el-Hak and C.-M. Ho, "The Pitching Delta Wing," *AIAA Journal*, vol. 23, pp. 1660-1665, 1985.
48. J.N. Adler and M.W. Luttges, "Three-Dimensionality in Unsteady Flow about a Wing," AIAA Paper 85-0132, 1985.

49. F.O. Carta, "Unsteady Stall Penetration of an Oscillatory Swept Wing," presented at AFOSR/FJSRL/University of Colorado Workshop on Unsteady Separated Flow, U.S. Air Force Academy, Colorado Springs, CO, 1983.
50. W.J. Wagner, "Comparative Measurements of the Unsteady Pressures and the Tip-Vortex Parameters on Four Oscillatory Wing Tip Models," 10th European Rotorcraft Forum, The Hague, Netherlands, 1984.
51. M.C. Robinson and J.B. Wissler, "Unsteady Surface Pressure on a Pitching Rectangular Wing," AIAA Paper 88-0328, 1988.
52. J.B. Wissler, F.T. Gilliam, M.C. Robinson and J.M. Walker, "Visualization of the Three-Dimensional Flow Structure About a Pitching Forward Swept Wing," AIAA Paper 87-1322, 1987.
53. A.O. St. Hilaire, F.O. Carta and W.D. Jepson, "The Influence of Sweep on the Aerodynamic Loading of an Oscillatory NACA0012 Airfoil," Volume 1 - Technical Report, NASA CR-3092, 1979.
54. A.O. St. Hilaire, F.O. Carta, "Analysis of Unswept and Swept Wing Chordwise Pressure Data from an Oscillating NACA0012 Airfoil," Volume 1 - Technical Report, NASA CR-3567, 1983.
55. A.O. St. Hilaire, F.O. Carta, "Analysis of Unswept and Swept Wing Chordwise Pressure Data from an Oscillating NACA0012 Airfoil," Volume 2 - Data Report, NASA CR-165927, 1983.
56. J. Ashworth, M. Waltrip and M.W. Luttges, "Three-Dimensional Unsteady Flow Fields Elicited by a Pitching Forward Swept Wing," AIAA Paper 86-1104, 1986.
57. J. Ashworth, W. Crisler and M. Luttges, "Vortex Flows Created by Sinusoidal Oscillation of Three-Dimensional Wings," AIAA Paper 89-227-cp, 1989.
58. M.W. Luttges and M.C. Robinson, "Control of Unsteady Separated Flow Structures on Airfoils," AIAA Paper 85-0537, 1985.
59. J.N. Adler and M.W. Luttges, "Three-Dimensionality in Unsteady Flow about a Wing," AIAA Paper 85-0132, 1985.

60. K. Salari and P.J. Roache, "The Influence of Sweep on Dynamic Stall Produced by a Rapidly Pitching Wing," AIAA Paper 90-0581, 1990.
61. N.M. Chaderijan and G.P. Guruswamy, "Unsteady Transonic Navier-Stokes Computations for an Oscillating Wing Using Single and Multiple Zones," AIAA Paper 90-0313, 1990.
62. P.L. Roe, "Characteristic-Based Schemes for the Euler Equations," *Annual Review of Fluid Mechanics*, pp. 337-356, 1986.
63. P.L. Roe, "Some Contributions to the Modeling of Discontinuous Flows," *Lecture in Applied Mathematics*, vol. 22, 1985.
64. A. Harten, "High Resolution Schemes for Hyperbolic Conservation Laws," *Journal of Computational Physics*, vol. 49, pp. 357-393, 1983.
65. S.R. Chakravarthy and S. Osher, "A New Class of High Accuracy TVD Schemes for Hyperbolic Conservation Laws," AIAA Paper 85-0363, 1985.
66. H.C. Yee, "Construction of Explicit and Implicit Symmetric TVD Schemes and Their Applications," *Journal of Computational Physics*, vol. 68, pp. 151-179, 1987.
67. A. Harten, and S. Osher, "Uniformly High-Order Accurate Non-Oscillatory Schemes I," *SIAM Journal of Numerical Analysis*, vol. 24, no. 2, pp. 297-309, 1987.
68. A. Harten, B. Engquist, S. Osher, and S. Chakravarthy, "Uniformly High Order Accurate Non-Oscillatory Schemes, 3," NASA CR-178101, 1986.
69. B. van Leer, "Toward the Ultimate Conservation Difference Scheme V, a Second-Order Sequel to Godunov's Method," *Journal of Computational Physics*, vol. 32, pp. 101-135, 1979.
70. P. Colella and P.R. Woodward, "The Piecewise Parabolic Method (PPM) for Gas Dynamic Simulations," *Journal of Computational Physics*, vol. 54, pp. 174-201, 1984.
71. A.J. Przekwas and H.Q. Yang, "Advanced CFD Methodology for Fast Transients Encountered in Non-Linear Combustion Instability Problems," SBIR Phase I

- Final Report for NASA Marshall Space Flight Center, CFDRC Report 4065/1, 1989.
72. H.Q. Yang, M.Z. Pindera, A.J. Przekwas and K. Tucker, "A Study of Pressure-Based Methodology for Resonant Flows in Non-Linear Combustion Instabilities," AIAA Paper 92-0709, 1992.
 73. S.D. Habchi, A.J. Przekwas, H.Q. Yang, ..., "REFLEQS-2D: A Computer Program for Turbulent Flows With and Without Chemical Reaction," Vol. 1, User's Manual CFDRC Report GR-88-4, 1989.
 74. M.L. Ratcliffe and C.E. Smith, "REFLEQS-2D: A Computer Program for Turbulent Flows With and Without Chemical Reaction," Vol. 2, Validation Manual, CFDRC Report GR-88-4, 1989.
 75. C.E. Smith, "Development of Scramjet Performance Correlations Using an Advanced CFD Code," CFDRC Report 4056/1, 1989.
 76. H.Q. Yang, S.D. Habchi and A.J. Przekwas, "A General Strong Conservation Formulation of Navier-Stokes Equations in Non-Orthogonal Curvilinear Coordinates," AIAA Paper 92-0187, 1992.
 77. S.W. Kim and C.P. Chen, "A Multiple Time-Scale Turbulence Model Based on Variable Partitioning of Turbulent Kinetic Energy Spectrum," AIAA Paper 88-1771, 1988.
 78. S.V. Patankar and D.B. Spalding, "A Calculation Procedure for Heat, Mass and Momentum Transfer in Three-Dimensional Parabolic Flows," *Int. J. Heat Mass Transfer*, vol. 15, pp. 1787-1806, 1972.
 79. J.P. Van Doormal and G.D. Raithby, "Enhancements of the SIMPLE Method for Predicting Incompressible Fluid Flows," *Numerical Heat Transfer*, vol. 7, pp. 147-163, 1984.
 80. R.I. Issa, "Solution of the Implicitly Discretized Fluid Flow Equations by Operator-Splitting," *J. of Computational Physics*, vol. 62, pp. 40-65, 1986.

81. C.M. Rhie and W.L. Chow, "Numerical Study of the Turbulent Flow Past an Isolated Airfoil with Trailing Edge Separation," *AIAA Journal*, vol. 21, pp. 1515-1532, 1983.
82. M. Peric, R. Kessler and G. Scheuerer, "Comparison of Finite-Volume Numerical Methods with Staggered and Colocated Grids," *Computers of Fluids*, vol. 16, pp. 389-403, 1988.
83. H.L. Stone, "Iterative Solution of Implicit Approximates of Multi-Dimensional Partial Differential Equations," *SIAM J. Num. Anal.*, vol. 5, pp. 530-558, 1968.
84. J. Wu, L.N. Sankar and D. Huff, "Evaluation of Three Turbulence Models for the Prediction of Steady and Unsteady Airloads," AIAA Paper 89-0609, 1989.
85. B.S. Baldwin and H. Lomax, "Thin Layer Approximation and Algebraic Model for Separated Turbulent Flows," AIAA Paper 78-257, 1978.
86. J.F. Thompson, Z.U.A. Warsi and C.W. Mastin, Numerical Grid Generation Foundation and Applications, North-Holland, 1985.
87. T.H. Pulliam, "Euler and Thin-Layer Navier-Stokes Codes: ARC2D and ARC3D," Notes for the Computational Fluid Dynamics User's Workshop, University of Tennessee Space Institute, Tullahoma, TN, 1984.
88. T.H. Pulliam and J.L Steger, "Implicit Finite-Difference Simulations of Three-Dimensional Compressible Flow," *AIAA Journal*, vol. 18, pp. 159-167, 1980.
89. T.H. Pulliam and D.S. Chaussee, "A Diagonal Form of an Implicit Approximate Factorization Algorithm," *Journal of Computational Physics*, vol. 39, pp. 347-383, 1981.
90. H.C. Yee, "A Class of High-Resolution Explicit And Implicit Shock-Capturing Methods," NASA TM-101088, 1989.
91. J.L. Thomas, S.L. Taylor and K.A. Anderson, "Navier-Stokes Computations of Vortical Flow over Low Aspect Ratio Wing," AIAA Paper 87-0207, 1987.
92. S. Ogawa, T. Ishiguro and Y. Takakura, "Numerical Simulations of Flow Filed around Three-Dimensional Complex Configurations," Proceedings of 27th

GAMM Workshop on Numerical Method in Fluid Mechanics, Vieweg, FRG, 1987.

93. G.H. Klopfer and H.C. Yee, "Viscous Hypersonic Shock-on-Shock Interaction on Blunt Cowl Tips," AIAA Paper 87-2033, 1987.
94. B. van Leer, J.L. Thomas, P.L. Roe and R.W. Newsome, "A Comparison of Numerical Flux Formulas for the Euler and Navier-Stokes Equations," AIAA Paper 87-1104CP, 1987.
95. P.L. Roe, "Finite-Volume Methods for the Compressible Navier-Stokes Equations," Proceedings of the International Conference on Numerical Methods for Laminar and Turbulent Flows, Pineridge, UK, July, 1987.
96. T.H. Pulliam and J. Steger, "Recent Improvements in Efficiency, Accuracy and Convergence for Implicit Approximate Factorization Algorithms," AIAA Paper 85-0360, 1985.
97. T.L. Holst, "Viscous Transonic Airfoil Workshop Compendium of Results," *J. of Aircraft*, vol. 25, pp. 1073-1087, 1988.
98. T. Pulliam, "Euler and Thin Layer Navier-Stokes Codes: ARC2D, ARC3D," Computational Fluid Dynamics Workshop Proceedings, UTS1, Publication No. E02-4005-023-84, 1984.
99. W.K. Anderson, J.L. Thomas and C.L. Rumsey, "Application of Thin Layer Navier-Stokes Equations Near Maximum Lift," AIAA Paper 84-0049, 1984.
100. C. Harris, "Two-Dimensional Aerodynamic Characteristics of the NACA0012 Airfoil in the Langley 8-Foot Transonic Pressure Tunnel," NASA TM-81927, 1981.
101. C.M. Maksymink and T.H. Pulliam, "Viscous Transonic Airfoil Workshop Results Using ARC2D," AIAA Paper 87-0415, 1987.
102. D.L. Huff, J.C. Wu and L.N. Sankar, "Analysis of Viscous Transonic Flows about Airfoils," AIAA Paper 87-0418, 1987.

103. C.L. Rumsey, S.L. Taylor, J.L. Thomas and W.K. Anderson, "Application of an Upwind Navier-Stokes Code to Two-Dimensional Transonic Airfoil Flow," AIAA Paper 87-0413, 1987.
104. P. Cook, M. McDonald, M. Firmin, "Airfoil RAE2822 - Pressure Distributions and Boundary-Layer Wake Measurements," AGARD AR-138, paper A6, 1979.
105. E.J. Jumper, S.J. Shreck and R. L. Dimmick, "Lift-Curved Characteristics for an Airfoil Pitching at Constant Rate," *Journal of Aircraft*, vol. 24, pp. 680-685, 1987.
106. J.M. Walker, H.E. Helin and J.H. Strickland, "An Experimental Investigation of an Airfoil Undergoing Large Amplitude Pitching Motions," *AIAA Journal*, vol. 23, pp. 1141-1142, 1985.
107. H.E. Helin and J.M. Walker, "Interrelated Effects of Pitch Rate and Pivot Point on Airfoil Dynamic Stall," AIAA Paper 85-0130, 1985.
108. J.H. Strickland and G.M. Graham, "Force Coefficients for a NACA0015 Airfoil Undergoing Constant Pitch Rate Motions," *AIAA Journal*, vol. 25, pp. 622-624, 1987.
109. K.W. McAlister and L.W. Carr, "Water Tunnel Visualization of Dynamic Stall," *Journal of Fluid Engineering*, vol. 101, pp. 376-380, 1978.
110. R. Landon, "NACA0012 Oscillating and Transient Pitching - Compendium of Unsteady Aerodynamic Measurement," AGARD-R-702, 1982.
111. J.J. Thibert, M. Grandjacques, and L.H. Ohman, "NACA0012 Airfoils: An Experimental DataBase for Computer Program Assessment," AGARD-AR-138, pp. A1-1-A1-19, 1979.
112. W.A. Spivey and G.G. Moorehouse, "New Insight into the Design of Swept-Tip Rotor Blades," 26th Annual National Forum of the American Helicopter Society, Washington DC, June, 1970.
113. W.A. Spivey, "A Study to Investigate the Aerodynamics of Rotor Blade Tip Shapes," Bell Helicopter Company Report, No. 299-099-468, Jan. 1970.

114. G.R. Srinivasan, W.J. McCroskey, J.D. Baeder and T.A. Edwards, "Numerical Simulation of Tip Vortices of Wings in Subsonic and Transonic Flows," AIAA Paper 86-1095, 1986.
115. G.C. Uhad, T.M. Weeks and R. Lange, "Wind Tunnel Investigation of Transonic Aerodynamic Characteristics of Forward Swept Wings," *Journal of Aircraft*, vol. 20, pp. 195-202, 1983.
116. G. Redeker and G. Wichmann, "Forward Sweep - A Favorable Concept for a Laminar Flow Wing," *Journal of Aircraft*, vol. 28, pp. 97-103, 1991.
117. U. Brennenstuhl and D. Hummel, "Vortex Formation over Double-Delta Wings," iCAS-82-6.6.3, 1982.
118. P.E. Olsen and R.C. Nelson, "Vortex Interaction over Double-Delta Wings at High Angle of Attack, " AIAA Paper 89-2191-Cp, 1989.
119. S.B. Kern, "Numerical Investigation of Vortex Flow Control Through Small Geometry Modifications at the Strake/Wing Junction of a Cropped Double-Delta Wing, " AIAA Paper 92-0411, 1992.
120. A.D. Young, "The Aerodynamics of Controls," AGARD-CP-384, Paper No. 17, October, 1984.
121. K.E. HOFFLE, M.R. Dhanvada, and M.C. Frassinelli, "Basic Studies on Delta Wing Flow Modifications by Means of Apex Fences," *Vortex Flow Aerodynamics Conference Proceedings*, NASA CP-2416, Hampton ,VA October 8-10, 1985.
122. R.M. Dhanvada, C. Moskovitz and D.G. Murri, "Forebody Vortex Management for Yaw Control at High Angles of Attack," *Journal of Aircraft*, vol. 24, no. 4, pp. 248-254, 1987.
123. J.K. Huffman, D.E. Hahne, and T.D. Johnson, "Aerodynamic Effectos of Distributed Spanwise Blowing on a Fighter Configuration," *J. of Aircraft*, vol. 24, pp. 667-679, 1987.